Scuola Normale Superiore

Ph.D. THESIS

IN

BIOPHYSICAL SCIENCES

Capturing molecular behavior in dynamic subcellular nanostructures

Filippo Begarani

Advisor

Prof. Francesco Cardarelli

2019/20

To all researchers in the world, beacon of hope for the entire humanity!

Foreword

This Thesis is the result of my research activity at NEST laboratory of Scuola Normale Superiore in Pisa: I began my PhD program studies in 2014, supported by Professor Francesco Cardarelli and his group where I found a stimulating and energetic environment loaded with profound ambition and deep scientific know-how; fundamental conditions necessary to carry out this PhD program in Biophysical Science.

List of publications

Begarani, F., D'Autilia, F., Signore, G., Del Grosso, A., Cecchini, M., Gratton, E., ... & Cardarelli, F. (2019). Capturing Metabolism-Dependent Solvent Dynamics in the Lumen of a Trafficking Lysosome. *ACS nano 13, 2, 1670-1682*

Begarani, F., Cassano, D., Margheritis, E., Marotta, R., Cardarelli, F., & Voliani, V. (2018). Silica-Based Nanoparticles for Protein Encapsulation and Delivery. *Nanomaterials*, *8*(11), 886.

In preparation: Begarani, F., D'Autilia, F., Del Grosso, A., Cardarelli, F. Investigating the dynamic behavior of molecular species in subcellular nanostructures by time-tunable raster-image correlation spectroscopy.

Table of Contents

Table of Contents

Table of Contents

Table of Contents

Foreword

It is no coincidence that modern Biophysics is commonly thought to have been born with the words pronounced by Erwin Schrödinger during his lectures held in 1943 at Trinity College in Dublin and collected in the book ***"What is Life? The Physical Aspect of the Living Cell"***[1]. Wondering about the complexity of life, Schrödinger admirably defines what will be, from then on, the main concern of an experimental biophysicist, that is, in his words: ***"how can the (molecular) events in space and time which take place within the spatial boundary of a living organism be accounted for by physics and chemistry?"*** Capturing the intrinsic spatial and temporal dimension of life regulation is a challenge that biophysicists have been increasingly embracing, building on nearly a century of studies at a variety of length scales. Over the last decades, the focus of biophysics progressively shifted from the macroscale to the nanoscale. Here, main actors are the molecules. To successfully address the intrinsic spatial and temporal scales of molecular behavior, two crucial requisites are needed: (***1***) nanometer spatial resolution (to tackle the spatial scale of molecules), (***2***) micro-to-millisecond temporal resolution (to probe the time scale that is relevant for molecular processes). In this context, optical microscopy is a valuable methodological approach. First, at wave numbers of visible light, and using fluorescence as readout, both the spatial and temporal scales can be investigated directly in living matter. In addition, the recently-developed super-resolution technologies[2] circumvented the remaining limit imposed by diffraction and pushed biophysical investigations to the true nanoscale.

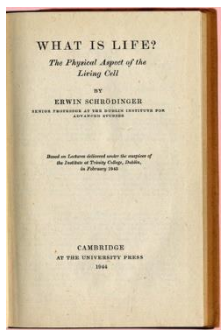
WHAT IS LIFE?

The Physical Aspect of the Living Cell

BY

ERWIN SCHRÖDINGER

CAMBRIDGE
AT THE UNIVERSITY PRESS
1944

In spite of these achievements, life regulation is destined to remain elusive in a natural condition of living matter, that of subcellular, membrane-enclosed nanosystems: transport vesicles, organelles, or entire subcellular protrusions. Here, the leading molecular actors are part of a reference nanosystem that is endlessly changing position in space and time in the complex 3D cellular environment. This peculiar condition imposes that a third requisite be concomitantly met in the same experiment, that is: (***3***) large volume sampling to localize the nanosystem. Unfortunately, however, volume sampling and temporal resolution are mutually-dependent parameters, i.e. the larger the volume to probe, the lower the temporal resolution achievable.

The overriding goal of my PhD Thesis is to grab the physics of life regulation at the level of nanoscopic, dynamic subcellular systems. By bringing state-of-the-art biophysical tools along the 3D-trajectory of the target system, unprecedented spatiotemporal resolution will be achieved to (i) enlighten the hitherto elusive realm of molecular processes occurring in the new reference system, and (ii) plan breakthrough experiments to interrogate living-matter physiopathology at the subcellular scale.

This Aim will be pursued by two main methodological and technological implementations at the subcellular scale, namely: (i) time-tunable Raster Image Correlation Spectroscopy (RICS) to analyze the average dynamic behavior (i.e. diffusion) of molecules within a population of subcellular nanosystems (i.e. organelles or compartments) and (ii) the combination of fast RICS with feedback-based 3D orbital imaging&tracking of a single intracellular nanosystem *per* time in order to maximize the temporal resolution achievable to look at molecular behavior.

In time-tunable RICS, a confocal microscope is used to capture standard images of the sample with a raster-scanning laser beam. Time-tunable RICS is achieved by acquiring consecutive stacks of images using different pixel

dwell times. Each scan speed is used as a filter to select the characteristic temporal scale of molecular behaviour that significantly contributes to the measured correlation function. This approach covers a hitherto unexplored dynamic range, as determined by available pixel dwell times, from 0.5 μs to several milliseconds.

On the contrary, by feedback-based 3D orbital imaging&tracking, the light-beam is sent in a periodic orbit around the nanostructure of interest. The recorded signal (e.g. fluorescence or scattered light) is used as feedback to localize the nanostructure position with unprecedented spatiotemporal resolution. The acquired, privileged observation point will be used to push single-molecule studies to an entirely new level, exploiting the analytical tools mentioned above (i.e. RICS analysis).

For the sake of clearness, results are organized as described in the following:

- In ***Chapter 1***, a review of the more common imaging-based techniques developed for quantitative molecular analysis at the subcellular level is reported. In this Chapter, each technique is presented highlighting advantages and drawbacks, with a particular emphasis on the peculiar spatial and temporal resolution, i.e. on the ability of each technique to grab the dynamic behavior of molecules at the subcellular level.
- In ***Chapter 2***, time-tunable RICS is introduced, with a particular focus on its application to the study of dynamic molecular processes hosted within subcellular nanosystems which are dynamic as well. The diffusion of a variety of fluorescent molecules is measured on different paradigmatic subcellular structures or organelles (e.g. lysosomes, mitochondria, secretory granules, etc.) either in their lumen or on their membrane.
- In ***Chapter 3***, RICS analysis is combined with feedback-based 3D orbital imaging&tracking. The Lysosome is selected as the main case-study here and the dynamics of different molecules either within lysosome lumen or on its membrane are measured to validate the

approach. The results obtained serve as a solid reference to introduce the subject of the next Chapter.

- In ***Chapter*** 4, RICS analysis along the orbit is used to unveil quantitatively the spatiotemporal fluctuations of the solvent contained in the lumen of lysosomes trafficking within living cells. Once again, lysosomes are chosen as a paradigmatic example of biomedical interest: different physiological and pathological conditions are tested.
- In ***Chapter 5,*** in conclusion of my work, possible implementations to improve the performances of the presented approaches are discussed, together with potential future applications in biophysics and related fields.

Chapter

1

Introduction

Cells contain distinct dynamic, membrane-enclosed sub-compartments with sizes spanning from tens of nanometers (e.g. synaptic vesicles, caveolae, clathrin-coated pits) to hundreds of nanometers (e.g. endosomes, lysosomes, mitochondria, secretory granules), to several microns (e.g. Golgi apparatus, Endoplasmic Reticulum, nucleus). In addition, each of these mentioned cellular compartments is designed to concentrate specific sets of components and functions[3]. This aspect of organization determines, in turn, a discontinuous and heterogeneous landscape of molecular composition, molecular functions and physicochemical properties within the cell.[4]. These properties, in turn, play an active major role in the regulation of the biochemical processes representative of each specific district. To study the heterogeneity of subcellular organization, the choice of the most suitable technique becomes crucial. Being able to assess both chemical, biological and physical properties within the correct spatial and temporal scales is

everything. At present, there are no techniques that makes all these aspects available at once, but few attempts to go towards that direction.

In particular, our ability to study molecular behavior at this level is severely hindered by the restless, rapid movement of the entire reference system in the 3D cellular environment. State-of-the-art optical microscopy tools for delivering subcellular information at molecular resolution fail to subtract the 3D evolution of the entire system while preserving the spatiotemporal resolution required to probe dynamic molecular events.

1.1 Molecular information at the subcellular level in a non-natural environment

The eukaryotic cell is characterized by a complex and well-organized mixture of biomolecules showing the most diverse functions and characteristics. Proteins, lipids, nuclei acids and other biomolecules get organized inside cells in an efficient and practical fashion to give birth to nuclei, cytoplasm, plasma membranes and a plethora of membrane-enclosed intracellular organelles to execute the most diverse functions.[3] The survival and function of every living organism and in particular of cell is thus strictly related to its internal organization, where multiple structures execute all the necessary tasks for cell homeostasis. It is for this reason that the term ‘organelle’ today is used to described specific intracellular environment where highly specialized functions take place[2].

These function-specific environments, whether they are found as membrane-enclosed or membrane-less organelles, comprise large protein complexes such as the signalosomes or protein-RNA complexes such as the ribosomes but also membrane-bound specific structures such as the mitochondria, the lysosomes, the exosomes, the Golgi apparatus and so forth[2,3,5]. In order to study these function-specific subcellular environments, many techniques and tools have been developed in the course of the human history, but, the

discoveries made in the last 100 years, with the advent of the transistor-based electronics, computer science, nanotechnology and Molecular Quantum Mechanics, along with their first experimental applications in the analysis of living organisms, paved the way to the development of a series of techniques that today represent the basis of ì Biophysics as a science.

1.1.1 The biochemistry of intracellular structures/compartments studied *in vitro*

Subcellular analysis was ideally born in 1682 thanks to the pioneer work of the microscopist Antoine Van Leeuwenhoek who first discovered the nucleus in cod and salmon red blood cells (Fig. 1.1). Mitochondria and Golgi apparatus were instead first described respectively in 1850's by Rudolph Albert von Kolliker and in 1890's by Camillo Golgi. Their observations were only possible thanks to the employment of the first, rudimental, optical microscopes. As a matter of fact, with the advent of transmission electron microscopy, in the 1940s and 1950s, the study of intracellular organelles began, and structures such as the endoplasmic reticulum (ER) and peroxisomes were discovered. In the same period, electron microscopy was accompanied by biochemical studies of the cell and its components. Cellular fractionation by centrifugation allowed, in this sense, for the discovery of other subcellular organelles such as the lysosomes in 1955 by Christian de Duve[2]. The importance of analysing these structures in terms of their molecular content was first addressed by O'Farrell and colleagues in 1977 via gel electrophoresis[6]. In this context, organelle proteomics helped to unveil the content of many subcellular structures[7–11]. A significant boost of this activity was imposed by the advent of mass-spectrometry-based approaches. The first demonstrations of mass spectrometry used for subcellular analysis dates back to the years 1984-85 when Richard W. Gross published his results on mitochondria and plasma membrane[12,13]. Since then, mass spectrometry

techniques such as Matrix-assisted laser desorption/ionization (MALDI) and Desorption electrospray ionization (DESI) have evolved to address subcellular contents.

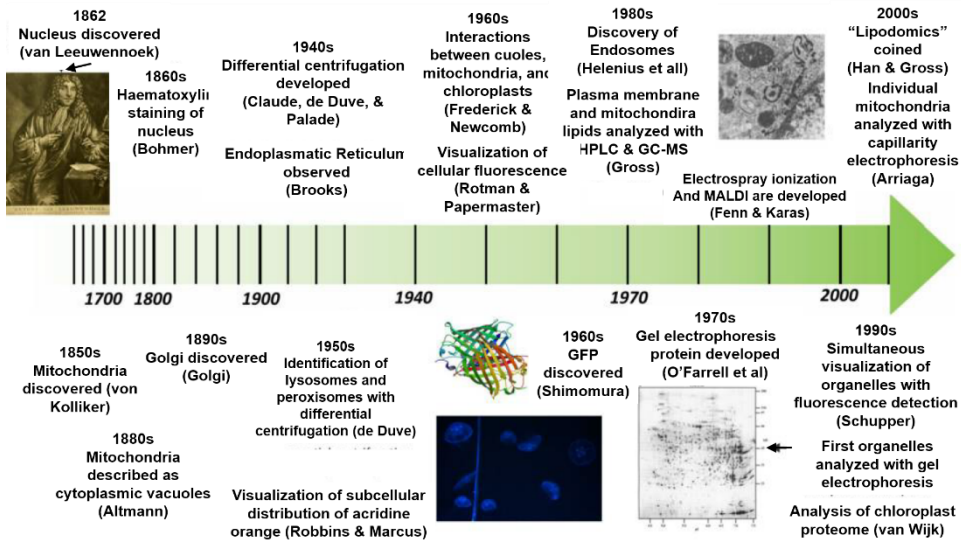

Figure 1.1 History of subcellular organelles studies. Image reprinted from ref. [2]

However, all these techniques imply either the isolation of the organelles from their original environment (*i.e.*, the cell) or the disruption of the structure itself. For instance, all the analytical tools created for organelle proteomics necessarily require the isolation of the organelles from the cells, thus altering their natural surrounding environment and consequently the complex dynamic behaviours they would assume within. Mass spectroscopy instead, works by extracting ionized atoms from the sample surface, thus destroying the sample as it is being analysed. It is for these reasons that these disruptive approaches will not be part of in this dissertation.

1.1.2 The ultrastructure of subcellular structures/compartments studied at the wavenumber of electrons

Electron microscopy (EM) has played an important role in biology and especially cellular biology. In recent years, EM reached the highest performances in terms of spatial resolution thanks to the development of cryo-EM that opened to the study of protein structure[14]. This was acknowledged in 2017 by the Nobel prize in chemistry awarded to Jacques Dubochet, Joachim Frank and Richard Henderson[15]. Fig. 1.2shows a roadmap of the key milestones reached by EM in biology since its first demonstration in 1932 by Knoll and Ruska[16]. Standard EM techniques, such as TEM (Transmission Electron Microscopy) and SEM (Scanning Electron Microscopy), have played an important role in the study of subcellular organelles. TEM allowed scientists to discover Mitochondria, the endoplasmic reticulum (ER), the Golgi apparatus and it is being widely used to study the final fate of innovative drug delivery systems such nanoparticles and other drug formulations[2,17–19]. Fig. 1.2 functions as an overall example of TEM used for imaging biological samples.

EM technologies met a dramatic improvement when Dubochet and his team discovered that water divided in thin films could be vetrified[20]. This result paved the way to cryo-EM and cryo-electron tomography (CET). In vitrified water, water molecules are in an amorphous state of ice that, in close proximity, resembles the state of liquid water. Today different methods for sample vitrification exist, but are all based on the use of cryogens such as liquid Nitrogen[14,17]. Sample preparation is then a fundamental step for the good success of the measurement. Cryo-EM has been combined with tomography to deliver 3D reconstruction of the analyzed samples. In CET samples are imaged from multiple angles and the images obtained are then recombined by specialized algorithms to deliver a 3D reconstruction of the sample; similarly to what happens in computed tomography (CT) in

medicine[14,21,22]. CET is particularly suitable for the study of cellular organelles and biomolecules, as the increasing number of reviews on this subject proves[21,23,24].

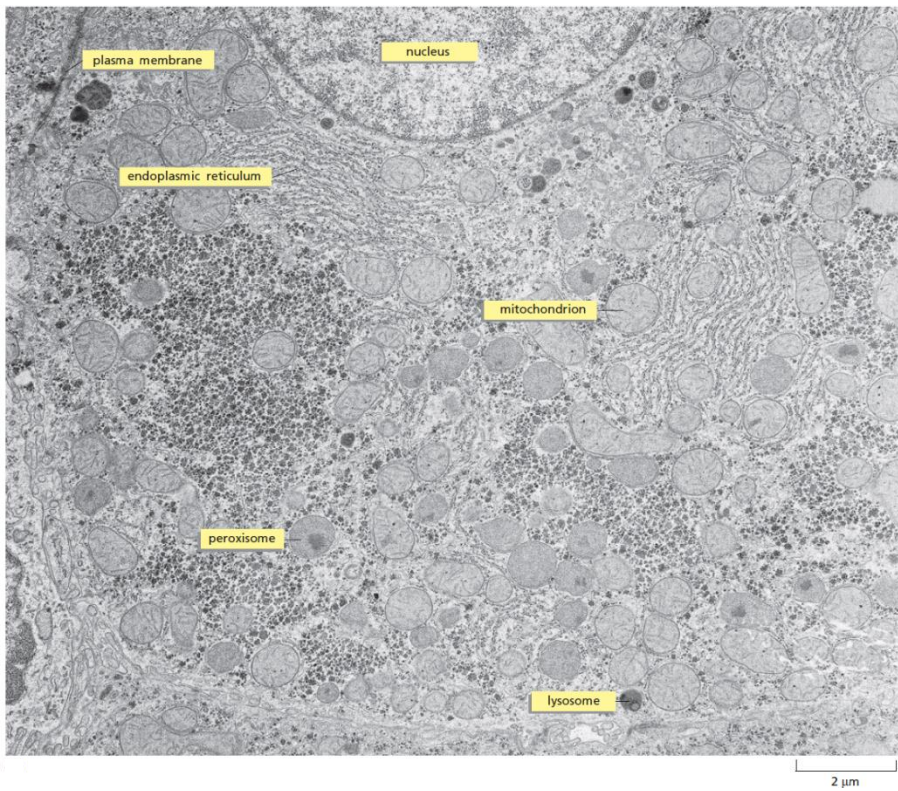

Figure 1.2 Example of TEM image of a cell. Thin section of a liver cell identifying a number of different structures.Image reprinted from ref.[3]

Nevertheless, the incredibly high spatial resolution of these techniques is achieved at the expenses of temporal resolution thus compromising the possibility to unveil dynamic behaviour of the structures of interest and of their molecular content.

1.1.3 Studying subcellular structures/compartments by means of nanoscopic probes: Atomic Force Microscopy (AFM).

Atomic Force Microscopy (AFM) represents another successful tool for the study of many morphological and chemical properties of biological samples such as DNA and proteins, viruses, bacteria, cells and also subcellular organelles[25]. In particular, AFM was employed to analyze mechanical changes at the nanoscale of rat heart mitochondria[26] (Fig. 1.3), to compare the properties of synaptic vesicles from rat brain[27] and to characterize the mechanical properties and their changes in retinal pigment epithelium melanosomes[28].

As the examples mentioned above proof, AFM is a technique suitable for the analysis of biological sample, especially when used in 'non-contact' mode that avoid sample damage. It offers high resolution and provide a true three-dimensional reconstruction of the surface of the sample. In addition, no special sample preparation is needed and AFM has proven to work nicely at ambient temperatures and in buffer solutions, thus allowing to study cells (and organelles) in their natural context. On the contrary, even if AFM shows a high axial resolution, its scanning speed is quite low compared to other techniques such as fluorescence microscopy, making it not suitable to study molecular behavior of subcellular structures. Although AFM-based techniques have potential for the study of the dynamic properties of subcellular organelles, they show important limits: organelle identification, organelle damage and low time resolution. As a matter of fact, it is really difficult to locate and identify subcellular organelles based only on their shapes and, for this reason, these structures are usually identified by optical techniques and/or isolated for making them accessible to AFM tips.

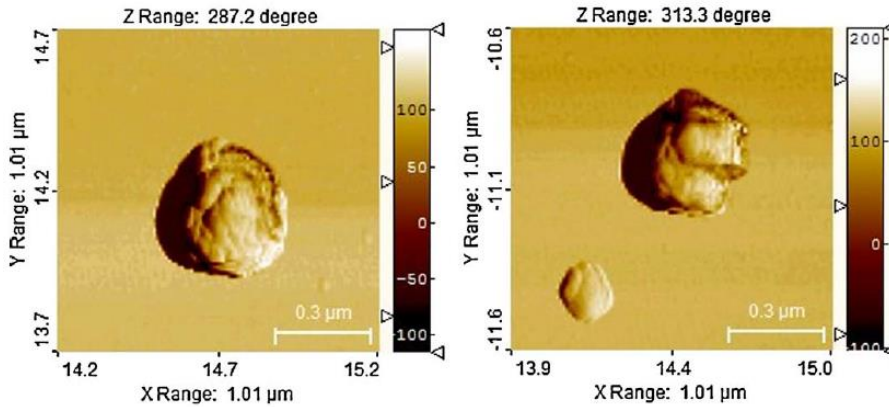

Figure 1.3 Example of AFM imaging of mitochondria isolated from hearts in rats. Image adapted from ref.[26]

1.2 "Chemical imaging" at the subcellular level: what perspectives?

In this section a brief review of the most common chemical imaging methods for cell biology application is reported. Even if these techniques possess a great potential, their potential application at the subcellular level is hampered by poor spatial resolution. Still, ongoing efforts in this regard promise to open the way for the analysis of molecular processes within living cells and also within subcellular structures.

1.2.1 Fourier Transform Infrared (FTIR) imaging

FTIR imaging provides information of the intra-molecular vibration modes of the analyzed samples. In FTIR briefly, an IR radiation is focused in a tiny spot on the sample. The light passing through or reflected back is than analyzed with a spectrometer. Major advantages of this technique lie on its ability to provide global organic information of the sample, a label-free high contrast and the use of harmless radiations that avoid damages of the irradiated area[29]. Although in principle this technique offers a series of major advantages, its

employment for biological studies is still limited. The reason for that lies on its intrinsic pour lateral resolution (i.e., 2.5 to 25 μm in the mid-infrared range 4000-500 cm^{-1}) with respect to the diffraction limit of light. This represents a big issue because it makes almost impossible the interpretation of IR spectra extracted from cells which does not correlate with the dimension of the pixel[29]. Nevertheless, Kazarian's group was able to visualize the distribution of chemical components in live human cancer cells without the need for labelling the sample and at a single cell level[30]. The introduction of more evolved optical systems such as the use of immersion lenses will certainly open new opportunities for cell imaging using FTIR[30].

1.2.2 Raman spectroscopy

Differently from FITR, the use of Raman spectroscopy for cell imaging has been gaining greater and greater consideration. In brief, Raman spectrum origins from inelastic scattering of incident photons on the sample surface. As opposed to vibration which requires changes in dipole moment, Raman scattering requires a change in polarizability. As final result, Raman spectroscopy returns a spectral information that is similar but, in many cases, complementary to IR spectra. The Raman effect is very weak because only a tiny fraction of incident photons undergoes Raman scattering. Nevertheless, Raman spectroscopy and thus Raman microscopy possesses many advantages compared to FTIR imaging. In fact, both inorganic and organic compounds have a Raman spectrum and they usually return bands that are sharp and specific from a chemical point of view. In addition, it is perfectly suitable for imaging live cells (Fig. 1.4) also due to its non-invasive properties. The combination of Raman spectroscopy with confocal microscopy allows for lateral and vertical resolution of 250 nm and 1μm respectively.

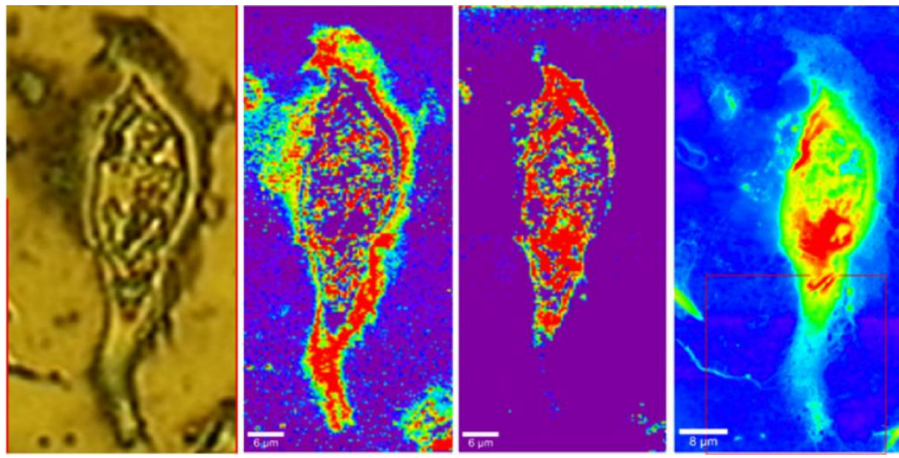

Figure 1.4 Raman confocal microscopy example. Raman images obtained with a confocal microscope at 250 x 250 nm^2 spatial resolution. From left to right: optical image of the cell; mapping of Raman shifts for lipids; phosphates and proteins. The red square in the image on the right was used for further analysis with AFM (not reported here). Image reprinted from ref.[29]

Due to its sensitivity to C-H groups, Raman microscopy is considered the best option for imaging lipids in biological systems, but, unfortunately, the typical scanning time required (i.e., tenths of minutes on average) makes Raman spectroscopy not suitable yet for the analysis of the dynamic behaviours of cells and in particular, of intracellular structure and processes. The development of faster detectors would for sure greatly increase the applicability of this technique to many more biological situations and structures[29].

1.3 Molecular information at the subcellular level from fluorescence-based optical microscopy

None of the techniques described so far allows to extract molecular information at the subcellular level simultaneously in space and time, inside

a living cell, at the proper resolution. They either entail the use of subcellular fractionation to isolate the structure/compartment of interest or they make use of sample fixation before measuring. An opportunity to tackle these issues comes in principle from fluorescence-based optical microscopy techniques. As a matter of fact, optical microscopy allows for the visualization of the molecules of interest (i.e., thanks to the use of fluorescent probes) inside living samples, by means of light sources in the UV-Vis- NIR range, that do not damage the sample and allow for prolonged imaging. Still, a major limit with optical microscopy techniques is represented by the diffraction limit of light that hinder the spatial resolution of the results (i.e., limited to around 250 nm). During the last decades, major efforts were made to overcome this limit. Super-resolution microscopy techniques were generated which allow fluorescence microscopy to push spatial resolution bypassing the diffraction limit imposed by visible light. Super-resolution microscopy represented such a breakthrough as a tool available to biologist and life science scientists that its inventors were awarded with Nobel prize for chemistry in 2014[31,32].

1.3.1 Localization-based methods: accuracy is a time-consuming task

A classical example of localization-based methods is represented by single molecule/particle tracking (SMT/SPT). These approaches rely on a common principle. Nanoscopic reporters such as quantum dots, gold nanoparticles or fluorescent probes/molecules are attached to the biomolecule of interest and imaged several times (thus forming a stack of temporal images) using standard optical microscopy techniques. Every image is analyzed using different image processing algorithms that have the final purpose of determining the final spatial coordinates of the center positions of each imaged particle.

In each frame the positions of each particle are linked to the positions they possessed in the previous and following frames of the series (Fig. 1.5), thus allowing to unveil important parameters such as the mean square displacement (MSD).

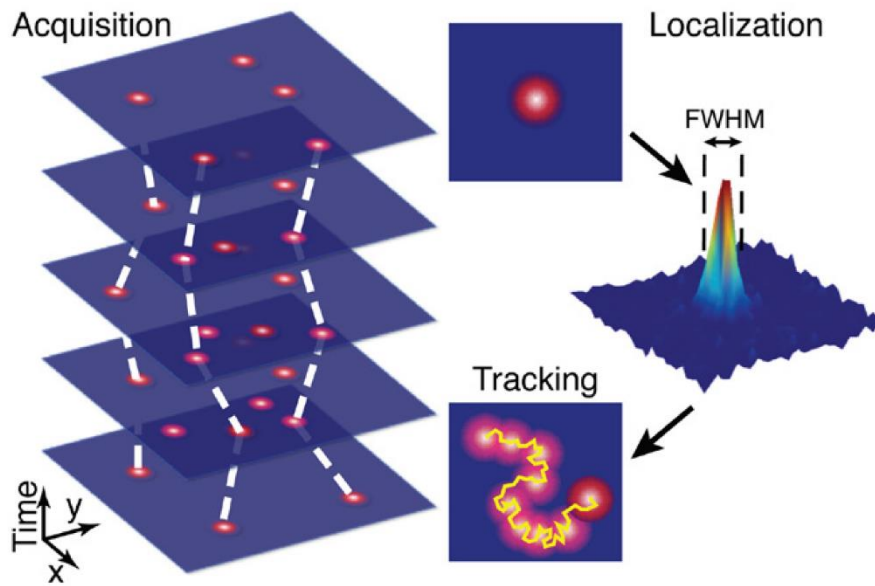

Figure 1.5 Principle of standard SPT. A series of images containing the labelled molecules of interest is acquired with a high-speed camera. The localization of the center-positions of each single molecule in each image of the series represents the core of the second step. These positions are then linked together between adjacent (in time) frames and trajectories of individual particles are generated. The displacement between two adjacent frames and the time elapsed between consecutive images give rise to the information about the dynamics of the observed objects. Image reprinted from ref.[148]

A fundamental requirement for localization-based microscopy is that the molecules/particles to be localized are sufficiently separated in space (i.e. the concentration is very low), a condition that is not always easy to obtain in biological experiments. Specific super-resolution approaches tackle this issue thanks to the use of photo-switchable/activable dyes or proteins (the general principle is explained in Fig. 1.6)[33]. These approaches were named stochastic optical localization microscopy (STORM)[34], photoactivated localization microscopy (PALM)[35] and fluorescence photoactivation localization microscopy (fPALM)[36]. Fig. 1.7 shows the difference, for instance, between the spatial resolution of conventional confocal microscopy and STORM[34] applied at the subcellular scale.

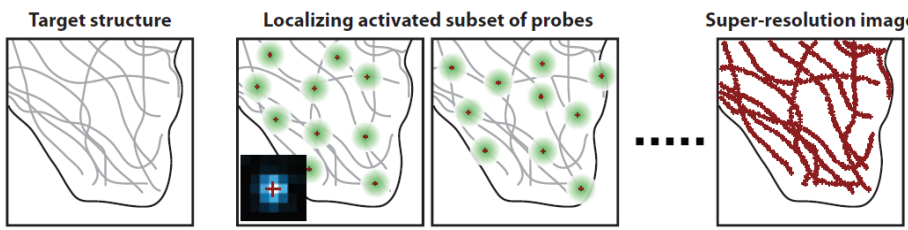

Figure 1.6 Principle of localization microscopy. Different spatially separated fluorescent probes are activated in different acquired image (thus at different time point). This avoids spatial overlapping of the active fluorophores and thus allows for their precise localization. After a long series of acquisition, a super-resolved image is reconstructed (*right*).
Image reprinted from ref. [33]

These super-resolution approaches, in order to work properly, rely on the collection of multiple images of the same sample area (in each image a different subset of fluorophores is activated). Typically, thousands of images are needed to generate the final super-resolved one. This may take up to several minutes, while many cellular processes (included those at the subcellular level which are of interest here) happen on a much shorter timescale[37,38] and requires a large amount of photons to be flashed on the sample. Also, even in its simplest configuration, the localization process *per se* is inherently limited by the time needed to acquire the number of photons

required for proper localization, and this in turn is linked to the choice of the fluorescent probe. Overall, localization-based techniques hit a limit at a resolution of about 10-20 nm.

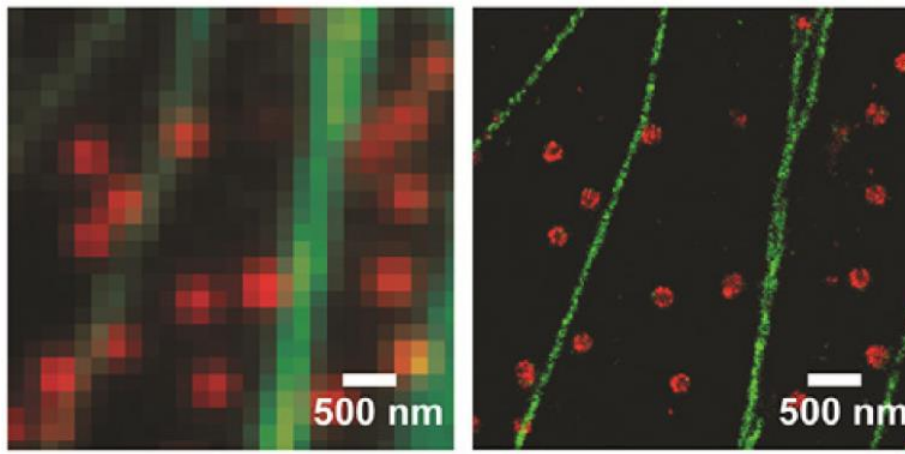

Figure 1.7. STORM imaging. Comparison of conventional confocal microscopy (left) and STORM (right) imaging of microtubules and clathrin-coated pits (CCP). Image reprinted from ref. [33]

Worthy of mention in this regard, Balzarotti *et al.* recently described another way of localizing single molecules called MINFLUX[39]. As in PALM and STORM, fluorophores are stochastically switched on and off, but the emitter is located using an excitation beam that is doughnut-shaped, as in stimulated emission depletion. Finding the point where emission is minimal reduces the number of photons needed to localize an emitter. MINFLUX attained ~1-nm precision, resolving molecules only 6 nanometers apart. MINFLUX tracking of single fluorescent proteins increased the temporal resolution and the number of localizations per trace by a factor of 100, as demonstrated with diffusing 30*S* ribosomal subunits in living *Escherichia coli*. As conceptual limits have not been reached, the authors expect this localization modality to break new ground for observing the dynamics, distribution, and structure of

macromolecules in living cells and beyond. Still, the ability of such strategy to discriminate between the dynamics of the structure of interest (the subcellular trafficking structure/organelle) and that of the biological processes occurring within the same structure has yet to be proven.

1.3.2 Structured illumination microscopy (SIM)

An alternative super-resolution approach not based on localization is Structured Illumination Microscopy (SIM). In brief, SIM exploits patterned light illumination to make high spatial frequencies available. A finely structured grating is placed on an intermediate image plane of a light widefield microscope that has the effect of projecting an illumination pattern through the optical path of the microscope on the sample surface[38,40–42]. The grating is characterized by a single spatial frequency that induce interference in the recorded image. This interference allows the spatial frequency information to be shifted down to lower frequencies; in this way the high frequency information previously too high to be collected is now available in the resulting image. SIM is particularly suitable for live-cell imaging and large areas of the sample can be imaged thanks to its implementation in wide-field microscopes but, unfortunately, can provide an improvement in resolution by only a factor of two[38]. The main drawback, along with the relatively poor spatial resolution, is represented by its relatively slow acquisition mode. The need to acquire multiple images of the same sample region requires obviously more time and this, in turn, implies the need for slow movements and low bleaching within the sample[37,38]. Given that, SIM remains suitable for live cell imaging, and experimental data demonstrated the possibility to obtain a single image reconstruction in a time range that spans from few seconds to hundreds of milliseconds[43,44]. Fig 1.8 shows the comparison between the results

originating from the imaging of labeled mitochondria using both standard confocal microscopy and 3D-SIM[45].

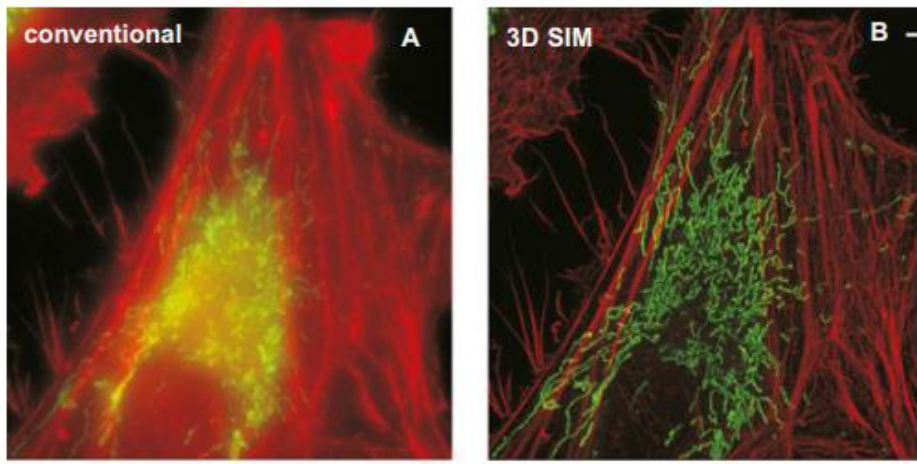

Figure 1.8 Live 3D SIM imaging of labelled mitochondria. Live 3D SIM imaging of mitochondria labelled with MitoTracker Green and the actin cytoskeleton labeled with tdTomato-LifeAct in a HeLa cell over 30 time points. (A) image taken using conventional microscopy. (B) 3D-SIM reconstruction of the same ROI shown in (A).Image reprinted from ref. [45]

1.3.3 Stimulated emission depletion microscopy (STED)

Proposed in 1994 by Hell and colleagues[46], the STED approach affords increased spatial resolution by shaping the observation spot of the laser well below the standard diffraction limit. The principle is easy to explain: molecules brought to the excited state by a first laser excitation can be brought to the ground state before spontaneous fluorescence emission occurs if a second laser, matching the energy difference between the excited and ground states, is used [33,37,46,47]. If the laser used to achieve stimulated emission presents a pattern with zero intensity at the center, this can be adopted to shrink the excitation PSF by simply forming an annulus that prevents spontaneous emission in the illuminated region. In this case, to achieve super-resolution, the region in the center of the annulus, where spontaneous

emission is allowed, must be smaller than the PSF of the laser use to have spontaneous emission[33]. To ensure that all spontaneous fluorescence emission is prevented, STED laser intensity must reach a certain threshold which may damage the sample itself; in addition, raising the power of the STED laser allows to expands the depletion zone without particularly affecting the fluorescence spontaneous emission area. The size of this region is only limited by practical physical issue, related to the practical power of the STED laser[33].

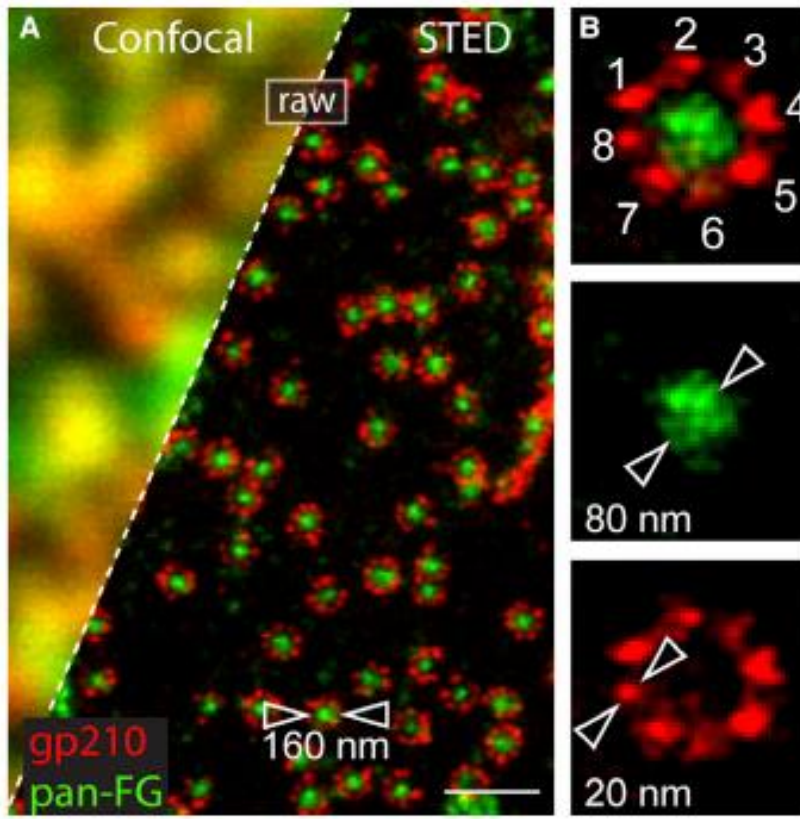

Figure 1.9 STED imaging of NPC. Comparison of conventional confocal microscopy and STED. In this particular case, (A) STED reveals immulabeled subunits in amphibian NPCs. (B) Individual NPC showing eight antibody-labeled gdp12 homodimers as 20-40 nm size units and a 80 nm-sized localization of the subunits in the central channel. Image reprinted from ref.[149]

Fig. 1.9 shows a series of Nuclear Pore Complexes (NPCs) imaged first with a standard confocal microscope (above) and later using STED (below)[48].

A major advantage achieved with STED microscopy is represented by the ability to deliver simultaneously high spatial and, potentially, temporal resolution. As a matter of fact, STED acquisition-time depends exclusively on the speed of the raster scan of the laser and the pixel dwell time used. Regard to this, important implementations were recently proposed. For instance, Schneider and co-workers successfully combined STED-based imaging with electro-optical scanning technologies to obtain an unprecedented line-scanning frequency of 250 kHz. Using SPT and taking advantage of the 70-nm static spatial resolution provided by STED, these authors investigated the dynamics of fluorescently labeled vesicles in living Drosophila or HIV-1 particles in cells with a temporal resolution of 5–10 ms[49]. More recently, Lanzano and coworkers integrated STED with Fluorescence Correlation Spectroscopy (FCS) as a tool to look at molecules, and with two additional analytical approaches, the separation of photons by lifetime tuning (SPLIT) and the fluorescence lifetime correlation spectroscopy (FLCS), to efficiently and simultaneously probe diffusion in a 3D environment at different sub-diffraction scales[50]. SPLIT-FLCS combination allowed probing, from a single FCS experiment, the diffusion from uncorrelated background, and continuously decreasing-in-size observation volumes in the cell cytoplasm, down to the spatial scale of approximately 80 nm, were reached. As a matter of fact, the authors proved the ability of STED-FCS-SPLIT-FLCS to generate the molecular diffusion laws at each single point in the cell at a relatively short spatiotemporal scale[50]. Worthy of mention here, FCS used as a tool to achieve single molecule sensitivity (with no need to dwell on or localize any molecule in particular) offers an ideal platform to increase the temporal resolution and the overall performances of available optical microscopy techniques (see also next section).

1.4 Fluorescence Correlation Spectroscopy: a powerful tool to boost the spatiotemporal resolution of optical microscopy methods

FCS represents a powerful tool to obtain information about the dynamics of molecules within living cells. In general, FCS is based on the autocorrelation of the fluorescent signal collected from fluorescent molecules contained in the sample; it provides the average diffusion time of the molecules contained in the observation volume and their average number. FCS and its various applications turned out to be particularly useful for the analysis of fluorescent molecules diffusing in the 3D intracellular environment (e.g. the cytosol) or on 2D biological membranes[51–56].

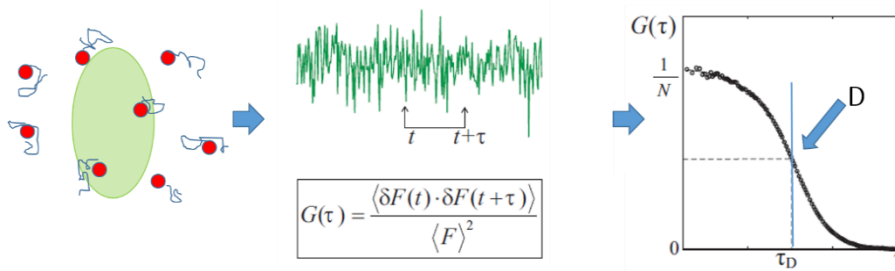

Figure 1.10 Principle of single-point FCS. The PSF of laser (*green ellipsoid*; this shape has been selected to highlight the fact that the axial dimension of the PSF in a confocal microscope is higher the lateral dimension) is focused on a diffraction-limited point in the sample volume (*left*); fluorescent molecules (*red dots*) diffuse in the volume of the samples; some of them will enter and some will exit the volume of the PSF. The fluorescent emission generated inside the PSF is collected and converted into an electric signal (*center*); autocorrelation function is then computed using the equation shown in the middle where G(τ) represents the autocorrelation, τ the time lag, t the actual time of the electric signal and F(t) the electric signal originated from the fluorescence emission. Once the autocorrelation function is obtained (*right*) it is fitted to obtain the average number of particles inside the observation volume or the PSF (inversely proportional to G(0)) and the average diffusion coefficient D of the molecules that passed through the PSF during the acquisition time. Image adapted from ref.[53]

To introduce its general principle, single-point FCS approach is taken as a paradigmatic example. In single-point FCS, the laser of a common confocal microscope is focused on single point within a solution (e.g. the cell cytosol) containing the fluorescent molecules of interest (Fig. 1.10). The fluorescence emission is collected through a light detector such as a PMT and converted into an electric signal and, in turn, its autocorrelation function is calculated. By fitting the autocorrelation function with a model curve allows for the determination of the average diffusion and the average number of the molecules contained in the PSF[53].

An important evolution of single-point FCS is the so called raster image correlation spectroscopy (RICS) technique[57–60]. RICS is a powerful tool since it exploits the movement of the PSF during a confocal microscopy acquisition. As depicted in Fig. 1.11, in RICS, a spatial autocorrelation between adjacent pixels is performed[59].

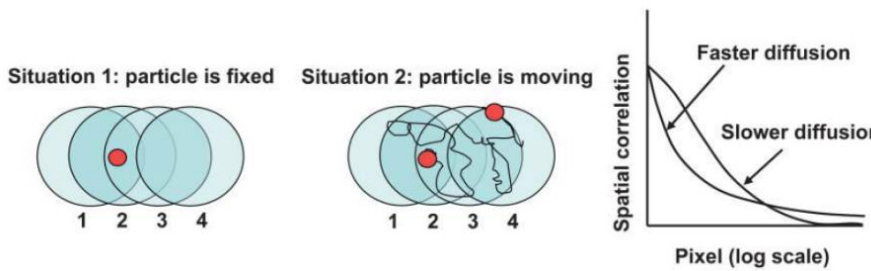

Figure 1.11 RICS principle. RICS represents a powerful tool since it exploits the autocorrelation between fluorescence signals recorded in time by adjacent pixels. In this situation a raster scan acquisition of a typical confocal microscope is assumed. (Situation 1, *left*) If a particle is fixed or slowly moving, its signal will be detected in pixels 1, 2 and 3 but not in 4 during a line acquisition. The spatial autocorrelation will then reveal a slower motion of the particle (*right*, slower diffusion). (Situation 2, *center*) if a particle is moving quickly, there is a higher probability that it will be detected also in pixel 4 and this will then be visualized on the autocorrelation function (*left*, *faster diffusion*). Obviously, the correlation of the fluorescence at different pixels of distance will be dependent on the size of PSF of the laser adopted as well. Image reprinted from ref.[59]

The fitting of the spatial autocorrelation function again returns information regarding the dynamics of the fluorescent molecules under investigation. Of note, if multiple scan speeds image correlation spectroscopy of fluorescence fluctuations are used (as presented by Groner and collaborators[61]) each scan speed can be used as a filter to select the characteristic temporal scale of molecular diffusion that significantly contributes to the measured correlation function. This approach can cover a wide dynamic range, as determined by available pixel dwell times, from below 1 µs to several milliseconds, and give selective access to average molecular displacements much smaller than the diffraction limit.

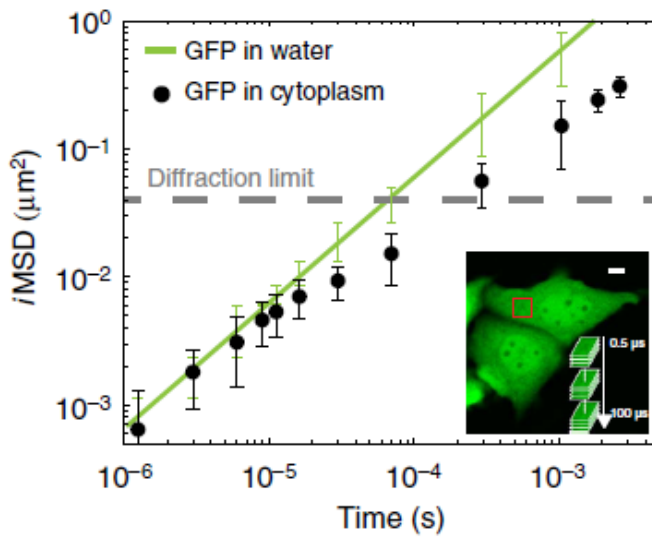

Figure 1.12 Mean Square Displacement analysis (MSD) obtained using RICS of GFP protein in the cell cytoplasm. Here the MSD of GFP protein contained in cell cytoplasm is shown in comparison to the MSD of GFP in solution. The authors found evidence, using RICS, that, for short spatial scales (less than 100 nm), free GFP was diffusing in the cytoplasm as if it was diffusing in water; thanks to this result, the authors were able to demonstrated the presence of water within the cell; a theory that, even if obvious, until that moment was in contrast with experimental data. Image adapted from ref.[60]

My colleagues at NEST used this approach to study the dynamics of a paradigmatic inert, nanoscopic molecule (i.e. GFP) in the cytoplasm of living cells as compared with dilute solutions. Thanks to this comparison, they proved short-range, unobstructed, Brownian protein translational motion within the cytoplasm at the temporal scale from 10^{-6} to $2x10^{-5}$ sec, corresponding to protein mean displacements from 25 to 100 nm[60] (Fig. 1.12). This was possible thanks to the high temporal resolution achievable with standard confocal microscope.

At the beginning of my PhD, such a platform appeared ideal to show how spatiotemporal fluctuation analysis can push the dynamic spatial resolution of a measurement well below the imaging nominal resolution, thus shedding light on unexplored dynamic phenomena such as the behavior of fluorescently labeled molecules trapped inside a vesicle.

To illustrate this, my colleagues had already performed a simulated experiment in which fluorescent molecules can move within a vesicle that is comparable in size to the static spatial resolution of the measurement (Fig.1.13). The simulated image series is used to reconstruct the iMSD profile of fluorescent molecules. Fig. 1.13 shows that by means of spatiotemporal fluorescence correlation spectroscopy, one can access the motion of fluorescent molecules trapped within moving vesicles and thus fully exploit information collected on timescales up to microseconds, which can be easily reached in a line-scanning acquisition with the aforementioned technology. In more detail, the iMSD plot displays two different diffusive regimes: a short-range diffusion that quantitatively describes the motion of molecules within the vesicle, and a 10-fold slower, long-range diffusion that reflects the movement of the entire vesicle. Both of these regimes match the imposed values. What is of importance here is that by applying spatiotemporal fluctuation analysis, we can resolve the dynamic behavior of molecules within

a submicrometric environment with a *dynamic* spatial resolution much higher than the nominal static spatial resolution set by the experimental conditions.

The idea to bring these potentialities into real experiments in living cells represents the starting motivation of my Thesis work..

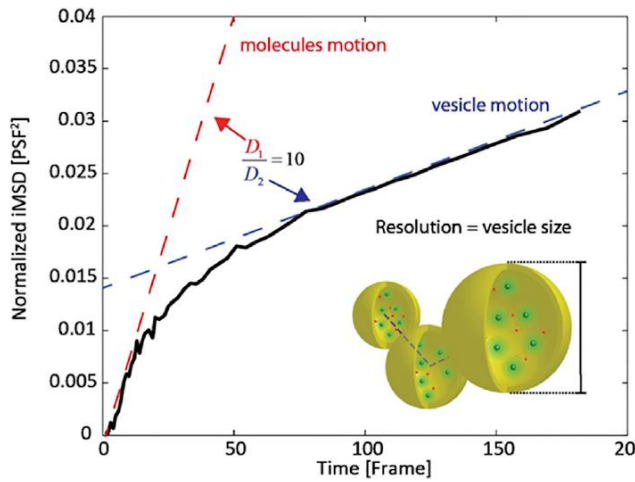

Figure 1.13 Spatiotemporal fluctuation analysis can super-resolve single molecule dynamics: a simulated experiment. A three-dimensional moving spherical object (in this case, a vesicle) with a diameter corresponding to the nominal measurement resolution (PSF) is filled with fluorescent molecules (see drawing in the inset). Both the vesicle and the molecules are free to diffuse, but the latter are 10 times faster than the vesicle and cannot cross the imposed spherical boundary. By applying spatiotemporal analysis of fluorescence fluctuations, one can measure the motion of the molecules within the vesicle (red dashed line) and the motion of the vesicle (blue dashed line) concomitantly, even if both are significantly smaller than the nominal imaging resolution. Image adapted from ref.[55]

Chapter

2

Time-tunable Raster Image Correlation Spectroscopy to capture molecular diffusion in dynamic subcellular nanostructures

2.1 Time-tunable RICS on dynamic subcellular nanosystems

As the name suggests, RICS exploits the raster scan movement of the laser beam, as in the case of a confocal microscope for instance; in RICS the signal originated by adjacent pixels in a frame is correlated (see below for more details)[58,59]. This allows users to follow the motion of fluorescent molecules that move along adjacent pixels with an average time comparable to the motion of the laser beam, which is usually in the microsecond regime. Thus, a longer pixel dwell time will result in the detection of slower probes and vice versa. Spatiotemporal Image Correlation Spectroscopy (STICS), instead,

considers the spatiotemporal correlation of pixels separated by different frames in a temporal stack of images collected. This reveals the motion of even slower fluorescent entities that change position among consecutive temporally separated frames[62]. With STICS, millisecond-sampling periods are obtained, unveiling the motion of entire intracellular compartments such as lysosomes or mitochondria. Starting from a theoretical work conducted by Di Rienzo et al. [60], we applied simple RICS analysis to study the motion of molecules inside intracellular moving compartments, representing, as far as we know, both a novelty in the field, and a potential and easy tool to be adopted in the study of nanoscopic compartments of biological interest.

2.1.1 RICS analysis

The temporal stacks of images acquired for every experimental situation were first filtered using a moving average filter that eventually subtracted to each frame the values resulted from averaging the same frame with the following ones in the temporal sequence; this allowed removing the contribution to the signal of the immobile components of the acquisition. Once the filtering procedure was completed, image stacks were analyzed using RICS technique[57–59].

The correlation curves derived from each experimental setup and each pixel dwell time were calculated on every image of the stack using Eq. 1:

$$G(\xi,\psi) = \frac{\langle I(x,y)I(x+\xi,y+\psi)\rangle_{x,y}}{\langle I(x,y)\rangle^2_{x,y}} \qquad \text{(Eq. 1)}$$

where I is the intensity of the pixel at the coordinates x (horizontal axis of the carpet) and y (vertical axis); ξ and φ are the spatial increments in the x and y direction respectively. Square brackets indicate the average operation over all

spatial coordinates (i.e., *x* and *y*). For each image stack, an average correlation (or RICS) curve was obtaining from the correlation curves of each image of the stack.

RICS curves were obtained from experimental acquisitions and these curves were fitted using the spatial correlation equation for normal raster scan acquisition[57]:

$$G(\xi,\psi) = \frac{\gamma}{N}\left(1+\frac{4D(\tau_p\xi+\tau_l\psi)}{w_0^2}\right)^{-1}\left(1+\frac{4D(\tau_p\xi+\tau_l\psi)}{w_z^2}\right)^{-\frac{1}{2}} \quad \text{(Eq. 2)}$$

where D is the diffusion coefficient, is the pixel dwell time while τ_l is the time between lines in the single frame; w_0 and w_z are respectively the planar and axial waists of the laser beam profile. Due to the possible variation in the laser alignment from day to day, the waist (w_0) of the excitation beam was calibrated before each day's measurements as previously described by Digman et al.[57]. The fitting of the experimental curve with Eq. 2 allowed us to find the diffusion coefficient (D) of the analyzed fluorophores.

The Stoke-Einstein equation (Eq. 3) was necessary to derive either the hydrodynamic radius or the solvent viscosity from diffusion measurements:

$$D = \frac{k_B T}{6\pi\eta r} \quad \text{(Eq. 3)}$$

2.1.2 STICS analysis

The temporal stacks of images acquired for every experimental situation were analyzed using STICS technique[62]. The correlation curves derived from each

experimental setup were calculated only for temporal stacks collected at 2µs pixel dwell time following Eq. 4:

$$G(\xi,\psi,\tau) = \frac{\langle I(x,y,t)I(x+\xi,y+\psi,t+\tau)\rangle_{x,y}}{\langle I(x,y,t)\rangle^2_{x,y}} \qquad \text{(Eq. 4)}$$

where I (x,y,t) is the intensity of the pixel at the coordinates x,y at time t; ξ and φ are the spatial increments in the x and y direction respectively and τ is the temporal lag between consecutive frames in the same temporal stack. In this particular case, we used temporal stacks acquired at 2µs pixel dwell time with 33 nm pixel size and 128 x 128 pixel resolution. This results in a time lag between two consecutive frames in a stack of 188 ms. Square brackets indicate the average operation over all spatial coordinates (i.e., x and y). For each image stack, a STICS curve was obtained and fitted following standard equations already described elsewhere[63]. This analysis returned the diffusion coefficients (D) of the motion of objects corresponding to a sampling period of 188 ms. It is important to stress that the employment of RICS alone would be sufficient to unveil the dynamic behaviour of both subcellular organelles and their molecular species contained within, but, nonetheless, the use of STICS will open to the possibility of analysing the movement of subcellular compartments to a lager temporal scales (compatible with the scales of other SPT techniques) thus allowing for a complete analysis of their behaviours simultaneously.

2.1.3 Time-tunable RICS validation on dynamic nanosystems in vitro

For the validation of this time-tunable FCS on nanoscopic vesicles, a set of experiments that could prove its reliability was conducted. Quantum dots (QDs) were selected as testing probes thanks to their high signal to noise ratio regarding fluorescence emission. RICS was initially performed on QDs simply dispersed in their buffer solution and average diffusion coefficients were extracted for every pixel dwell time (Fig. 2.1 and 2.2).

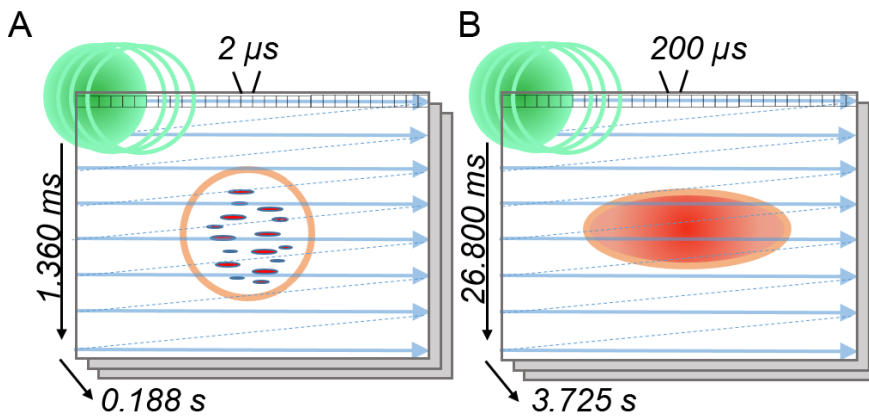

Figure 2.1 Time-tunable RICS principle. Schematic representation of the main concepts underlying the technique. (A) The use of short pixel dwell time (*e.g.*, 2 µs that translates in 1.360 ms of line time and 0.188 s of frame time) unveils the motion of fluorescent molecules inside intracellular compartments. (B) With long pixel dwell time ((*e.g.*, 200 µs that translates in 26.800 ms of line time and 3.725 s of frame time) the motion of the compartment is more and more dominant in the overall result.

To simulate intracellularly moving vesicles, QDs were loaded inside liposomes, and they were then poured in an agarose solution to be slowed down. Temporal stacks of confocal images were collected at different pixel dwell time and correlation curves were obtained and fitted (Fig. 2.2). Diffusion coefficients were then extracted as for the previous experiment.

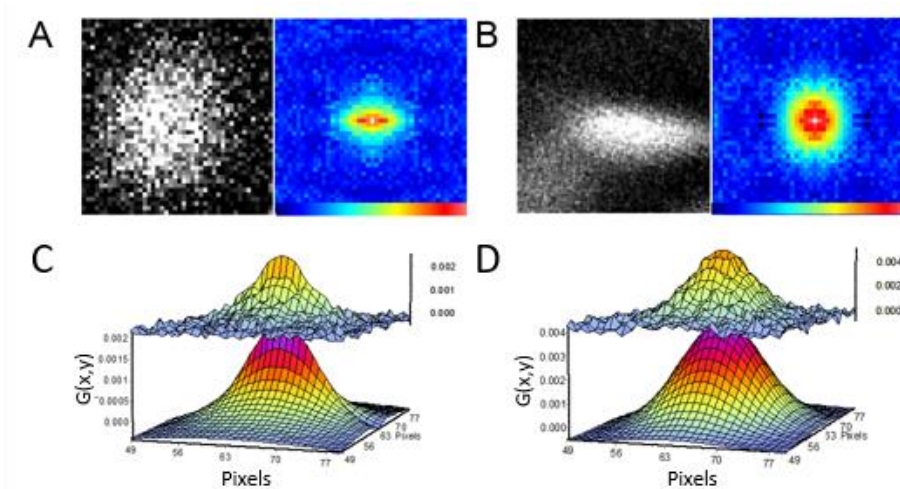

Figure 2.2. Pixel dwell time comparison. (A) Illustrative frame collected at 2 µs showing a liposomes containing QDs (left) and its corresponding RICS curve (right with color scale bar: red represents the highest value and dark blue the lowest). (B) Illustrative frame collected at 200 µs showing the same liposome containing QDs reported in A (left) and its corresponding RICS curve (right with color scale bar: red represents the highest value and dark blue the lowest). Notice how RICS curve corresponding to 200 µs is broaden if compared with the 2 µs curve. This is explained by the detection of faster movements in the acquisition reported in A. (C) Real (above) and fit (below) RICS curves of the acquisition reported in A. (D) Real (above) and fit (below) RICS curves of the acquisition reported in B. Notice how RICS curve in D is broader than the curve reported in C. Again, this is due to the selection of slower motional behaviors of the acquisition in D compared to the faster ones collected in C.

As Fig. 2.3 shows, with a fast scan speed we were able to select and analyze the motion of fast molecules inside moving organelles, while, as the scan speed slows down, the motion of the compartment itself becomes more and more relevant in the outcome of the correlation (Fig. 2.1A and B). For this reason and in order to analyze all possible motions inside intracellular compartments, temporal stacks of confocal images were acquired at different pixel dwell times, namely at 2, 4, 8, 20, 40, 100 and 200 µs.

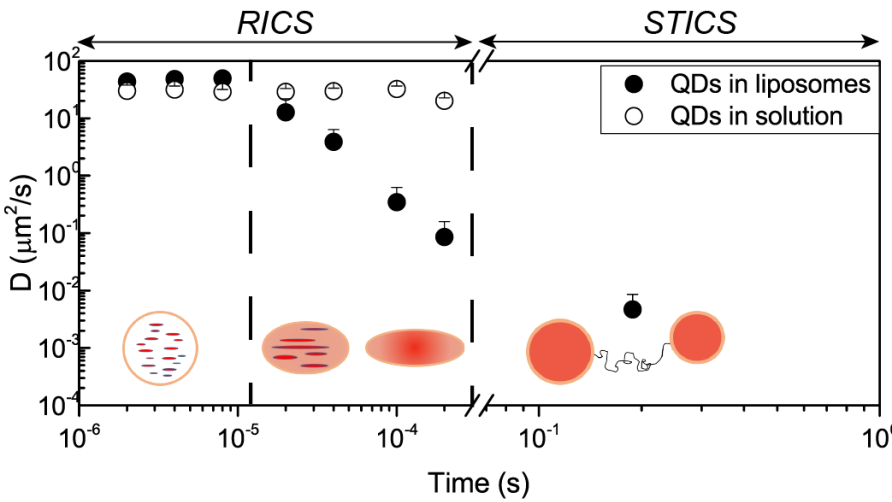

Figure 2.3 Diffusion coefficients of QDs within liposomes at different pixel dwell times. This graph shows the Diffusion coefficients found for both QD-loaded liposomes (black dots) and QDs in buffer solution (white dots) at different sampling time. Note the distinction between RICS and STICS time domains. Below the data, we reported a schematic representation of the situation studied at different time samplings. On the left, thus for short pixel dwell times (few microseconds) we find a situation in which RICS analysis reveals movement of the molecules inside the liposome. As we move towards longer sampling times (hundreds of microseconds), the situation is a sort of mixture between the molecular movements and the displacements of the entire structure; until, for STICS time domains (hundreds of milliseconds), only the displacement of the entire compartment sticks out in the correlation analysis.

These stacks were then analyzed using RICS and STICS and diffusion coefficients at different sampling time were extracted by fitting the obtained correlation curves with the equations provided above in section 2.1.1 and 2.1.2.

As Fig. 2.3 reports, diffusion coefficients of QDs inside liposomes (black dots) follow the values of the coefficients of free QDs (blue dots) for short pixel dwell time (2, 4 and 8 µs). As pixel dwell time increases, the motion of the overall liposome prevails in the correlation analysis and diffusion coefficients start decreasing until they reach the value of the coefficient of the sole liposome found with STICS analysis (188 ms). It is worth to mention that diffusion coefficients of free QDs are reported only for RICS analysis, since it is impossible with STICS to recover their full diffusivity due to the down-sampling limit of the technique.

To further prove the reliability of this technique we compared the diffusion coefficients obtained at 4 µs of pixel dwell time with the coefficients found on the same samples using feedback-based 3D Orbital Tracking (OT) technique combined with RICS (this is a really complex technique that will be the object of the following Chapters; for this reason and for a detailed description the reader is redirected to Chapters 3 and 4; within this particular experimental work, the technique was simply adopted as a control experiment). As described in Chapter 3, OT is a feedback-based tracking technique that moves an excitation light beam along an orbit surrounding the fluorescently labeled structure of interest (in our case a QD-loaded liposome). Analyzing the collected fluorescence signal of OT with RICS allowed us to recover the diffusion coefficients of the fluorescent probes (QDs in this case) and the motion of the overall tracked structure (the QD-loaded liposome in this second case). The values obtained with OT were comparable to the coefficients obtained using RICS and STICS (see Fig. 2.4).

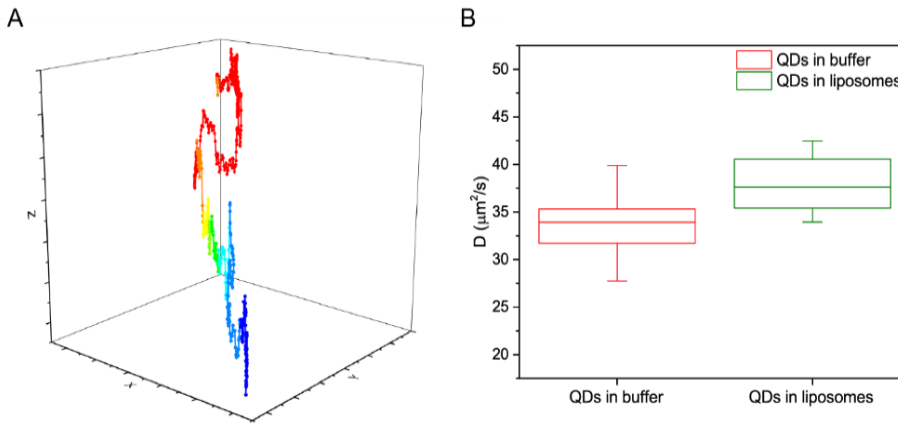

Figure 2.4. Control experiments with Orbital Tracking on QD-loaded liposomes. (**A**) Example of a QD-loaded liposome trajectory in agarose gel obtained using 3D orbital tracking. The average Diffusion coefficient of liposomes slowed down in Agarose gel is 0.085 ± 0.047μm^2/s (expressed as mean ± standard deviation). Ticks on axes represents pixels, thus 50 nm of space distance. (**B**) Plot of the diffusion coefficients of both QDs dispersed in Borate buffer (red) and QD-loaded liposomes in Agarose gel (green) measured obtained with Orbital Tracking using 4 μs of pixel dwell time. Upper and lower edges of the boxes represent the 25 and 75 percentiles of the distributions found; the middle line shows the mean value. Whiskers show standard deviations.

2.1.4 Time-tunable RICS validation in biological samples

The lysosome is selected as a paradigmatic case study. HeLa cells were cultured in physiological conditions and treated with Red Lysotracker (Fig. 2.5); this fluorescent dye was selected as it proved to be prone to the analysis of molecule diffusion in combination with FCS[64]. Stacks of images at 33 nm of pixel size were collected under a confocal microscope at different sampling times. Again, acquisitions were done at 2, 4, 8, 20, 40, 100 and 200 μs of pixel dwell time and data were analyzed using RICS and STICS (Fig. 2.5 and 6).

The analysis returned diffusion coefficient values decreasing in time as for the case of QD-loaded liposomes (Fig. 2.3).

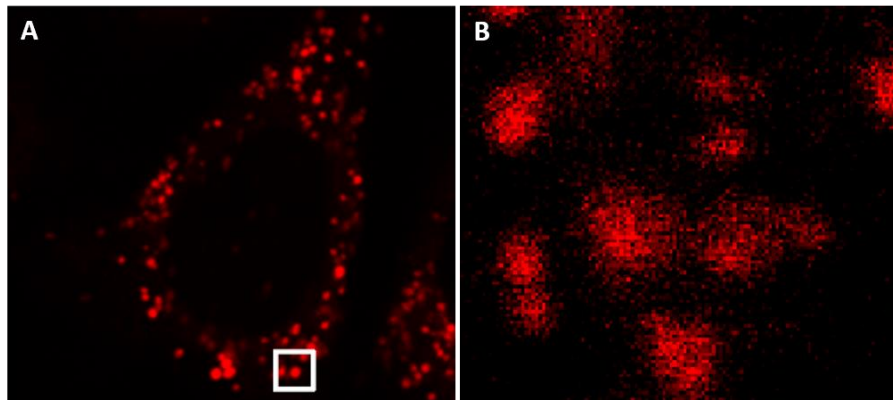

Figure 2.5 Red Lysotracker in lysosomes of HeLa cells. (A) Confocal image of a HeLa cell labelled with Red Lysotracker (scale bar 10 µm). (B) Magnification of figure A, white square. This is the magnification used for time-tunable RICS experiments (*i.e.*, 33 nm per pixel).

Using the Stoke-Einstein equation (Eq. 3 section 2.1.1), and assuming a hydrodynamic radius of 0.8 nm for Red Lysotracker inside lysosomes, we

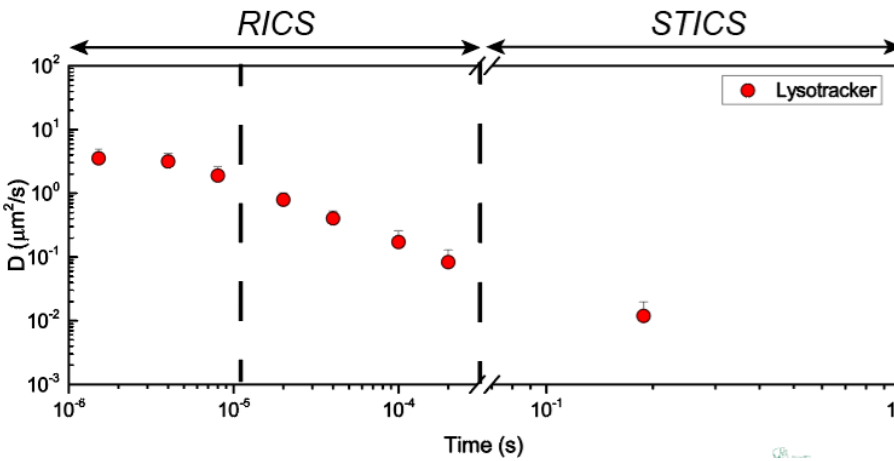

Figure 2.6 Diffusivity of Red Lysotracker in lysosome of HeLa cells. This graph shows the Diffusion coefficients of Lysotraccker inside lysosomes of HeLa cells different sampling time. Notice the distinction between RICS and STICS time domains.

extrapolated an average lysosome viscosity of 73 cP that is line whit what previously showed in literature by Wang et al[65].

Measurements on free Alexa488 in solution were also acquired as a control experiment (Fig. 2.7), resulting in much higher diffusion coefficients as expected when compared to Lysotracker inside lysosomes.

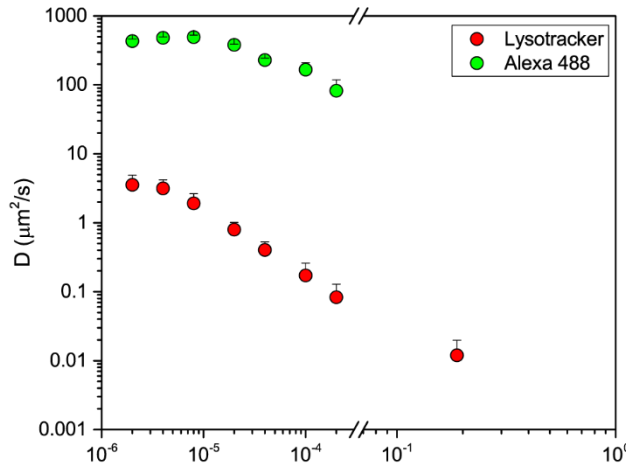

Figure 2.7 Comparison between diffusion coefficients of free Alexa 488 dissolved in water and of Red Lysotracker in lysosomes of HeLa cells. This graph shows the Diffusion coefficients found for both free Alexa 488 dissolved in water (green dots) and Red Lysotracker (red dots) contained in the lysosomes of HeLa cells at different sampling time. Notice how free Alexa returns diffusion coefficients that are two order of magnitude higher than Lysotracker; both Alexa and Lysotracker are small molecule with comparable hydrodynamic radius, but Alexa is diffusing in a much less viscous environment (*i.e.*, pure water). We highlight the fact that after 20 μs of pixel dwell time the diffusion coefficients of Alexa start decreasing due to a down-sampling condition; due to high diffusivity of Alexa it becomes impossible to follow its rapid movements using long sampling period; it is a physical limit.

Unfortunately, there is no obvious way to determine the hydrodynamic radius of Red Lysotracker inside lysosomes, due to the acidic condition and the crowded environment that characterize lysosomes.

It is worth to highlight that more than a viscosity value, time-tunable RICS affords a measurement of the 'apparent' diffusion coefficient. I deliberately used the word 'apparent' because the diffusion coefficient strictly depends on the sampling time at which the acquisition is performed. Thus, comparing diffusion coefficients extrapolated with the same pixel dwell-time is mandatory. Still, based on the fact that the diffusivity (and thus the viscosity) obtained by RICS is in good agreement with the results reported before by Wang et al.[65] (obtained by a completely different strategy: lifetime applied to an activatable rotor probe), we are prompted to speculate that our estimates are close to the real viscosity of the organelle. In addition, feedback-based 3D OT, as shown in the next Chapter can afford a similar estimate of the average diffusion coefficient of the organelle itself. In addition, the average value found using STICS and Lysotracker (*i.e.*, 0.012±0.007 $\mu m^2/s$, mean ± SD)is also close to the results obtained by Digiacomo et al.[66] on HeLa cells treated with Lysotracker using iMSD, a technique close to the STICS proposed herein.

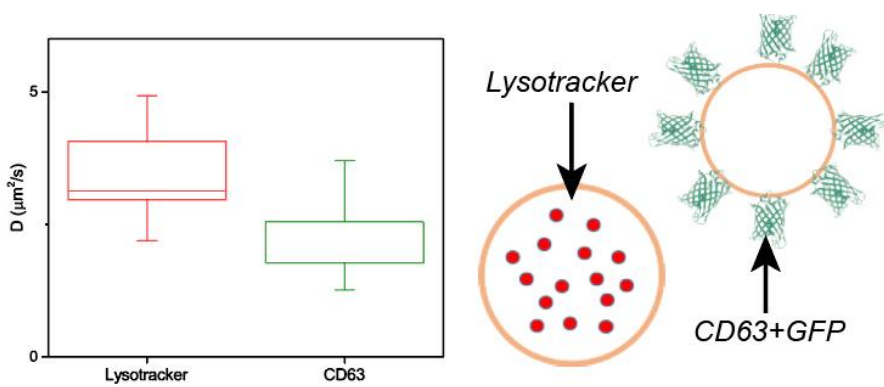

Figure 2.8 Diffusivity of Red Lysotracker and GFP-labeled CD63. Plot of the diffusion coefficients of Red Lysotracker (red) and GFP-labeled CD63 (green) measured on lysosomes of HeLa cells obtained at 2 μs of pixel dwell time. Upper and lower edges of the boxes represent the 25 and 75 percentile of the distributions found, the middle line shows the mean value. Whiskers show standard deviations (left side). Schematic representation of the two distinct situations (right side).

To provide additional support to the reliability of this application, we again conducted the analysis on lysosomes, but, this time, using a different

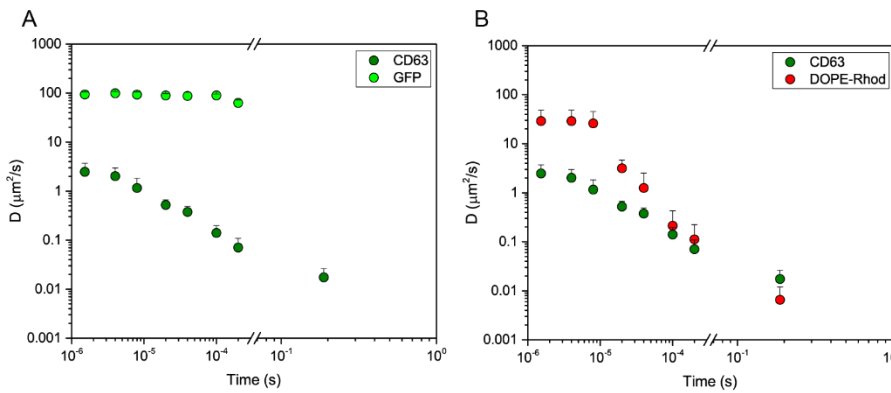

Figure 2.9 Control experiments for GFP-labelled CD63 protein. To further prove the reliability of the measured values of CD63 protein in HeLa cells, we conducted control experiments where we measured diffusivity of both free GFP in water and Rhodamine-labeled DOPE lipid in liposomes. In this latter case, liposomes were formed as a mixture of lipids: Rhodamine-labeled DOPE and DPPC (see Appendix B). (A) This graph shows the Diffusion coefficients found for both free GFP dissolved in water (light green dots) and GFP-labeled CD63 on lysosomes of HeLa cells (dark green dots) at different sampling time. Notice how free GFP, as for Alexa 488 above, returns diffusion coefficients that are almost two order of magnitude higher than Lysotracker; both free GFP and CD63 are small proteins with comparable hydrodynamic radius, but free GFP is diffusing in a much less viscous environment (*i.e.*, pure water). (B) Here the graph shows the diffusivity of both CD63 in HeLa cells (green dots) and Rhodamine-labeled liposomes (red dots). We found different diffusivities especially for short pixel dwell times where the molecular diffusion gives a higher contribution to the correlation curves. The analysis returned that Rhodamine-DOPE diffuses on liposome surface much faster than CD63 does on lysosome surface as expected. In addition, as for the case of free GFP and GFP-alebelled CD63 protein reported in A, the rate of molecular diffusion of Rhodamine-DOPE showed a much slower behavior compared to free Rhodamine in solution as previously demonstrated[150]. The proposed method is also able to discriminate different diffusivity even on the surface of nanoscopic structures and not only inside them.

fluorescent probe: GFP-labeled CD63. CD63 is a protein that is expressed on the external surface of lysosomes (Fig. 2.8).

HeLa cells were transfected with GFP-CD63 plasmids (see appendix B) and temporal stacks at 2, 4, 8, 20, 40, 100 and 200 µs pixel dwell time were acquired. Fig. 2.8 (left part) shows the comparison between the diffusion coefficients of Lysotracker inside lysosomes and CD63 on the external surface of lysosomes obtained at 2 µs pixel dwell time. Lysotracker molecules inside lysosome move faster than protein on its external surface (Fig. 2.8, right part). Given this last result, we can finally state that time-tunable RICS and STICS offer a simple and efficient tool to study the behavior of different molecules both in the lumen and on the surface of an analyzed nanoscopic compartment.

To support these later results, measurements of the diffusivity of free GFP in solution and of DOPE-Rhodamine lipid on liposome membrane were also acquired (Fig. 2.9), showing an expected difference in the diffusivity values extrapolated.

2.2 Concluding remarks

The use of RICS analysis to study the dynamic behavior of subcellular organelles revealed itself as a useful and promising instrument for this kind of applications. Its versatility and reliability have been demonstrated in the experiments reported above. Here, the lysosome has been chosen as a paradigmatic example and the results found with this approach were in good agreement with what found with other techniques such as OT and RICS (described in details in the next Chapters). In addition, with time-tunable RICS we were able to unveil the different viscosities between the lysosomal lumen of Twitcher and WT cell models. Worthy of note is the fact that time-

tunable RICS and STICS is not limited to specific organelles or structures. Current preliminary experiments performed by my group showed interesting results, in term of feasibility, on mitochondria and insulin granules. The simplicity of its application is limited only by the choice of the labelling approach and by the discovery of biologically relevant information.

It is fundamental to stress that time-tunable FCS does not require specific, tailored-made and expensive instruments. Any biological lab equipped with a standard confocal microscope can adopt this approach. Even image processing skills are not mandatory since everyone could download the free version of the simFSC software (www.lfd.uci.edu, University of California Irvine).

This technique may pave the way to new important discoveries associated with the understanding of subcellular dynamics. The application of time-tunable RICS with super-resolution technologies, such as STED, could further enhance its spatial resolution allowing the observation of distinguished dynamic marks inside the same structure. Cross-correlation tools combined with time-tunable acquisitions could in principle allowed for the analysis of the dynamics of different proteins and their interactions. Even the study of protein conformational changes may become accessible with this approach. The further development and improvement of imaging systems such as the introduction of faster photon detectors or the establishment of new labelling approaches will also bring benefits to this well-known technique that has not been exploited to its maximum potential yet.

Chapter

3

Bringing RICS on the trajectory of single subcellular nanostructures by feedback-based 3D orbital tracking

In the last Chapter, time-tunable RICS was used to study the dynamic behaviour of molecular species inside a moving subcellular compartment, the lysosome. We demonstrated that time-tunable RICS can be a powerful tool that empowers biophysicists with the ability to study the dynamics of molecular species contained within moving subcellular compartments. It is an easy-to-implement technique since it requires only a confocal microscope and a basic mathematical tool to perform the correlation and fitting operations. As described in previous Chapter, time-tunable RICS offers (1) good spatial resolution and (2) high temporal resolution; in addition, it allows to remove from the analysis the movement of the subcellular compartment, thus leaving only the dynamic information of the molecular species contained within its

boundaries. Still, the proposed approach suffers from being limited to the analysis of an optical section of the sample, in which (*i*) the contribution from several organelles may be averaged and (*ii*) each organelle is followed for a limited amount of time (as compared to its intracellular characteristic lifespan). In other words, the approach suffers from poor volume sampling on single organelles.

The experimental work presented in this Chapter tackles this bottleneck by focusing an excitation light-beam in a periodic orbit around the sub-cellular organelle of interest (Fig. 3.1). The recorded fluorescence signal is used as feedback to track the position of the structure of interest.

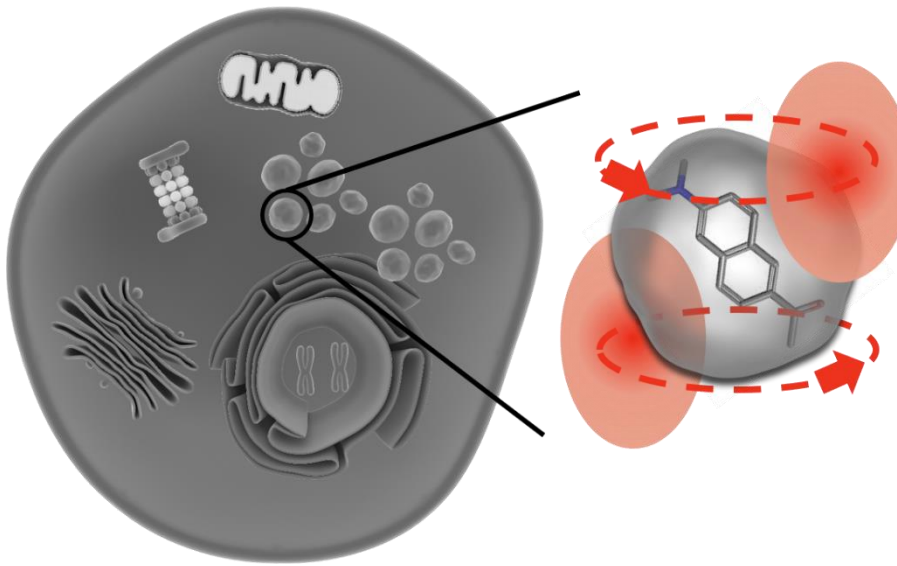

Figure 3.1 Principle of feedback-based Orbital Tracking (OT). OT allows to move, following a periodic pattern, the laser beam around an object of interest. During its movement, the laser excites the fluorescent species contained within the object of interest and the OT system measures their fluorescent and use the fluorescent signal as a feedback to correct the periodic trajectory of the laser in order to keep at object at its center. Note that the object is surrounded by two orbits (upper and lower): this is needed to calculate the axial position of the object of interest.

As already proven, OT allows for the subtraction of the natural movements of the subcellular reference system while preserves the required temporal resolution to study biological processes, i.e. microseconds along the orbits, milliseconds between the orbits[67–70].

The lysosome is selected here as a paradigmatic sub-cellular target due to its important role in metabolism, signalling, and cell-growth regulation[71–74].

3.1 From many organelles to a single organelle: the feedback-based 3D Orbital Tracking principle and setup

Feedback-based 3D OT measurements were carried out adopting the ISS Orbital Tracking System, analogous to that previously described[75], and embedded in an Olympus FluoView 1000-ASW-2.0 confocal laser microscope. The scanning of the excitation light was obtained in the x–y plane and in the z axis through two galvano-motor driven mirrors (Cambridge Technology) and a piezo-objective positioner (Phisik Instrument) respectively, both driven by a computer card (three-axis card, ISS). During tracking, the ISS system sends two π/2-phase-shifted sine wave voltage signals to the scanning mirrors of the microscope in order to generate a laser circular orbit; the offset values of the sine wave signals determine instead the scanning center. In tracking mode, the position of the center of the orbit is updated at each tracking cycle (every 4 orbits in our case) in accordance to an algorithm based on Fast Fourier transform (FFT) of the collected reference signal[76]. From the FFT of the fluorescence signal, one can get the continuous (or "DC") component (i.e., the zeroth term of the Fourier series) and its "AC" component as the first harmonic term of the Fourier series. Having the "DC' and "AC" components allows to determine the distance of a tracked object from the center of the orbit using the modulation of the signal (defined as modulation = AC/DC) and the angular coordinate by the phase of the AC

term. The tracking system changes the sine wave signals of each orbit (i.e., one orbit above the object of interest and another below it) in such a way to keep the modulation at its minimum, thus keeping the particle at the center of the orbit. To assess the vertical position of the 3D-tracked object, the ISS system evaluate the relative position of the object with respect to the upper and lower orbit simply by calculating the modulation of the average intensity of the 2 orbits, with the formula: MOD= $2*(I_{top}-I_{bottom})/ (I_{top}+I_{bottom})$, where I_{top} and I_{bottom} represents the average fluorescence intensity collected during the upper and lower orbits respectively. In our experiments, the fluorescence signal was collected on 256 pixels around a 150 nm-radius orbit with a period of 1024 ms (thus using a pixel dwell time of 4 μs derived from 1024 ms/ 256 px = 4 μs), while the vertical axial distance between the orbits was maintained at 800 nm; the orbit positions were updated every 4-orbit period (defined as a "cycle", approximately 4 ms). In doing so, the tracking system keeps trace of the movement of the center of the orbits and thus of the movements of the tracked object such as the lysosome in this particular case.

3.1.1 Circular-RICS analysis on the orbit: microseconds along the orbit, milliseconds between orbits

During OT measurements, the fluorescence intensity signal was collected and stored in intensity carpets where each column represents a pixel along the orbit and each row reports each orbit collected, as previously described[68]. Adjacent columns represent adjacent pixels along the orbit, while adjacent rows correspond to consecutive orbits during the acquisition. Spatial correlation was calculated on intensity carpets using the following equation:

$$G(\xi,\psi) = \frac{\langle I(x,y)I(x+\xi,y+\psi)\rangle_{x,y}}{\langle I(x,y)\rangle^2_{x,y}} \quad \text{(Eq. 1)}$$

where I is the intensity of the pixel at the coordinates x (horizontal axis of the carpet) and y (vertical axis), and ξ and φ are the spatial increments in the x and y direction, respectively. Square brackets indicate the average operation over all spatial coordinates (i.e., x and y). Spatial correlation curves were obtained from experimental carpets, and, later, these curves were fitted using the spatial correlation equation for circular scanning[57]:

$$G(\xi,\psi) = \frac{\gamma}{N}\left(1\frac{4D(\tau_p\xi+\tau_l\psi)}{w_0^2}\right)^{-1}\left(\frac{4D(\tau_p\xi+\tau_l\psi)}{w_z^2}\right)^{-\frac{1}{2}} exp\left(-\frac{\frac{1}{2}\left[\left(\frac{2\xi\delta r}{w_0}\right)^2\right]}{1+\frac{4D(\tau_p\xi+\tau_l\psi)}{w_0^2}}\right) \text{(Eq. 5)}$$

where D is the diffusion coefficient, w_0 and w_z are respectively the planar and axial waists of the laser beam profile. Also, τ_p is the pixel dwell time and τ_l is the time between lines in the intensity carpet (that, in this case, corresponds to the orbit time). The fitting of the experimental curve with Eq. 5 allowed us to find the apparent diffusion coefficient (D) of the molecules studied (in this particular case, ACDAN or QDs). The Stoke-Einstein equation (Eq. 3) was used to derive either the hydrodynamic radius or the solvent viscosity from diffusion measurement

3.2 ACDAN stability as a fluorescent marker of the lysosomal lumen

To study lysosome by feedback-based 3D orbital tracking, a particular fluorescent probe was employed: 6-acetyl-2-dimethylaminonaphthalene (ACDAN). Synthesized by Gregorio Weber in 1979[77] and designed as a relaxation probe for various biological environments; ACDAN possesses peculiar properties, many of which particularly suitable for the study of lysosomes. As a matter of fact, (*i*) ACDAN enters cells and its partitions mostly into hydrophilic environments[78,79], while simultaneously becoming

brighter within the most viscous/crowded ones (as demonstrated for other DAN probes[80]) as in the case of the lysosome lumen; in addition,(*ii*) ACDAN has non-ionizable groups making it insensitive to pH changes (especially in the range from 4 to 10[79]), analogously to the other DAN probes[81]; (*iii*) it also possesses an enhanced sensitivity to solvent polarity relaxation, showing pronounced red-shifts in the emission spectrum for increasing solvent polarity values[77–79] (fundamental properties for the experimental study described in Chapter 4). All these properties make ACDAN suitable for spontaneous and robust labelling of lysosomes in live cells.

ACDAN subcellular localization in living HeLa cells was probed by standard confocal microscopy (Fig. 3.2). Upon its administration to the cell medium at 5 µM, ACDAN spontaneously redistributed in few minutes into cells. In keeping with previous observations in yeast cells[79], ACDAN signal was characterized by a heterogeneous, punctuate-like intracellular distribution (Fig. 3.2).

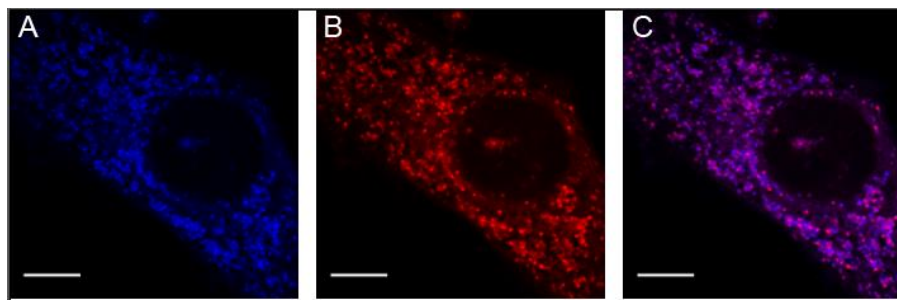

Figure 3.2 Staining of the lysosomal lumen in living cells with ACDAN. Confocal microscopy images of HeLa cells labelled with ACDAN (A) and LysoTracker (B) and the corresponding overlay of the two signals (C). Scale bars: 10 µm.

The localization within specific sub-cellular compartments was assessed by co-localization experiments with known fluorescent markers of sub-cellular structures. As evident from the images in Fig.3.2, a major contribution to ACDAN localization came from lysosomes (labelled with Red Lysotracker). This was also quantitatively expressed by the two calculated Manders' Overlap Coefficients (MOCs: hereafter M1 and M2) for the two signals (Fig. 3.3). In particular, M2 (Lysotracker *vs* ACDAN) was slightly higher than M1 (ACDAN *vs* Lysotracker): demonstrating the non-exclusive localization of ACDAN within lysosomes.

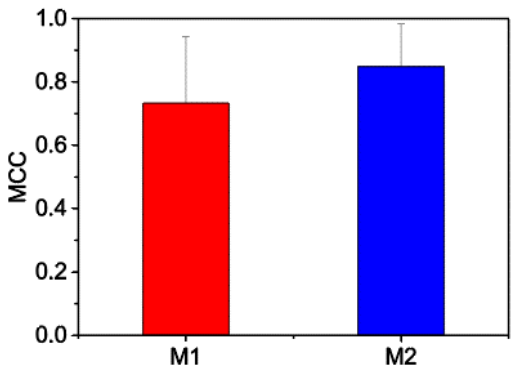

Figure 3.3 Colocalization of ACDAN and Red Lysotracker. Here the quantitative analysis of the co-localization between ACDAN and LysoTracker signals obtained by using the Fiji® plugin for co-localization analysis and Manders' coefficients (M1 and M2) is reported. Values represent the Mean ± SD for N=10 cells.

As a matter of fact, Fig. 3.4 shows that ACDAN not only labels lysosomes but also, although to a lesser extent, mitochondria and other structures within the cytoplasm and nucleoplasm.

The different intensity of ACDAN signal within these compartments (i.e. lysosomes>mitochondria>cytoplasm>nucleus, Fig. 3.4) agrees with previous reports on analogous probes[82], and may depend on the viscosity of the sensed environment. In particular, it seems that higher viscosities correlate with higher intensity and vice versa.

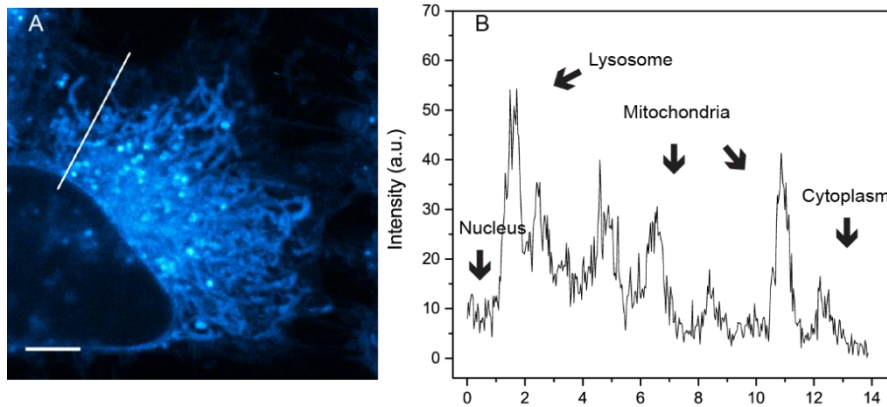

Figure 3.4 ACDAN distribution in HeLa cells. (A) Confocal microscopy images of HeLa cells labelled with ACDAN, Scale bar: 5 µm. (B) Normalized intensity profile along the white line depicted in (A) showing the different accumulation of ACDAN with respect to different compartments (i.e., lysosomes>mitochondria>cytoplasm>nucleus). This is just a representative example. In reality, many images were acquired and all showed the same behaviour reported here.

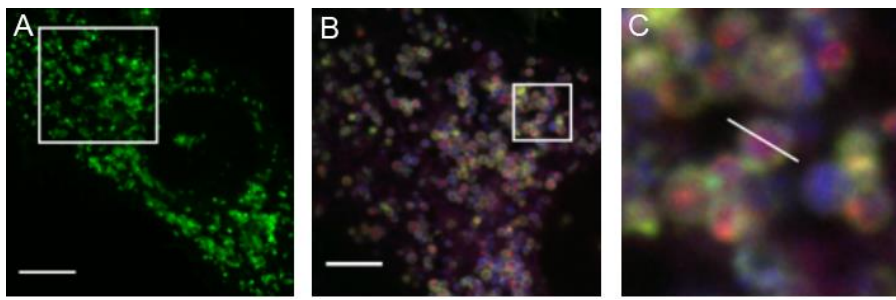

Figure 3.5 Concentration of ACDAN within the lumen of lysosomes. (A) The same HeLa cells shown in Fig. 3.2 are also expressing the lysosomal protein CD63-EGFP; (B) Zoom of the area enclosed in the white square in (A) showing many distinguished labelled lysosomes and the overlay of all the three signals (ACDAN, Red Lysotracker and GFP-labeled CD63) recorded. Scale bar: 5 µm; (C) The area identified with the white square in (B) is reported here to show the magnification of single lysosomes.

In order to prove that ACDAN is insensitive to membrane-associated solvent dynamics[83], its labelling potential was compared with specific markers of the lumen (i.e. Lysotracker) and membrane (i.e. EGFP-labelled CD63) (Fig. 3.5 A-C) of the lysosome. The intensity profile of ACDAN superimposes to that of Lysotracker showing a maximum peak in the lumen of the organelle (Fig. 3.6, blue and red lines). This is in contrast with the intensity profile of CD63-EGFP that reports two maxima at the edges of the lysosome (i.e., on membranes) and a minimum close to lumen (Fig. 3.6, green line).

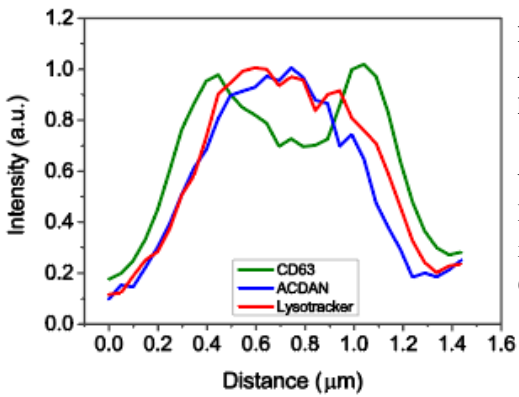

Figure 3.6 Intensity profiles of ACDAN, Red Lysotracker and GFP-laebeled CD63 protein in lysosomes. Normalized intensity profiles along the white line in Fig. 3.5C for a single lysosome; blue line reports ACDAN intensity profile, green line represents CD63-EGFP and red line LysoTracker.

3.3 Feedback-based 3D Orbital tracking and RICS on single lysosomes

In this particular configuration the fluorescence from ACDAN was used to generate a feedback signal for OT system. Fig. 3.7 reports the conceptual experimental setup.

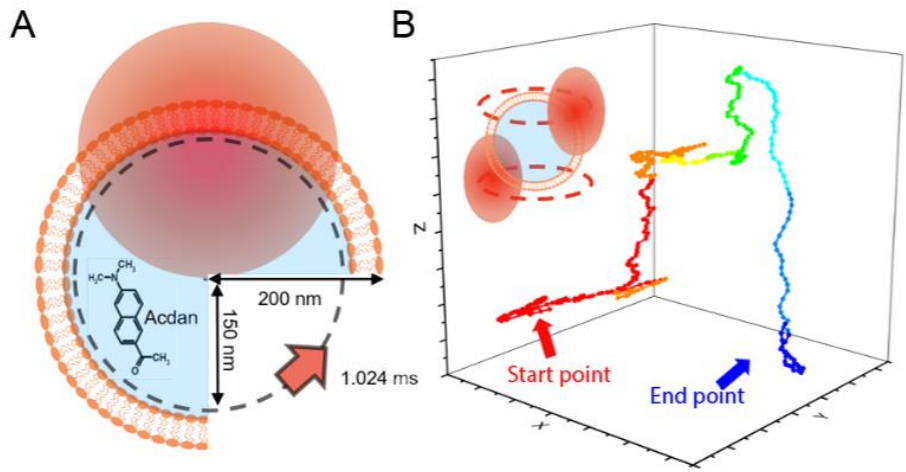

Figure 3.7 Feedback-based 3D Orbital tracking setup on single Lysosomes. (A) Scheme of a typical feedback-based 3D orbital tracking configuration. In red the laser Point Spread Function (PSF), in orange lysosomal membrane and in light blue the lysosome lumen; 200 nm is the average radius of lysosomes; 150 nm is the radius of the laser orbit adopted and 1.024 ms represents the time selected for the laser to complete an entire orbit. The drawing is not in scale. (B) Example of a real single-lysosome trajectory originated from a feedback-based 3D orbital tracking measurement. Ticks on axes represents pixels of 50 nm of size. It is evident that lysosomes on average moved a few micrometers in each direction during the measurements. On the top-left we reported a schematic representation of a typical feedback-based 3D orbital tracking configuration: a lysosome is shown at the center along with the scanning PSF (red) creating two orbits separated along the axial direction.

In addition, Red Lysotracker was used as reference to unequivocally select lysosomes for the tracking experiment. Tracking measurements last 30-60 seconds each and were conducted at 1-millisecond temporal resolution per orbit (i.e. microsecond sampling along each orbit). For each tracked lysosome a 3D trajectory (Fig. 3.7B) was extracted and the analysis of the trajectories returned the Mean Square Displacement (MSD, Fig. 3.8) and the average diffusion coefficient (D, $\mu m^2/s$) of each tracked organelle. The results obtained, in terms of both the shape of the MSD curve and the retrieved D (0.009 ± 0.010 $\mu m^2/s$, Mean ± SD) were in good agreement with what previously obtained with the *i*MSD approach[64].

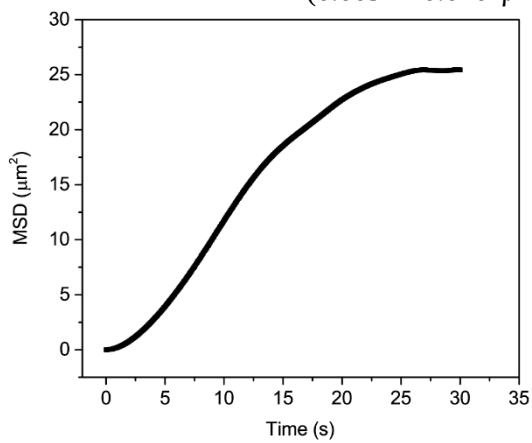

Figure 3.8 MSD of ACDAN-labelled lysosomes. Plot of the average Mean Square Displacement originated from recovered 3D trajectories of lysosomes.

It is worth mentioning that lysosomes typically move several microns in the x-y-z directions during a measurement (Fig. 3.8); this proves the suitability of 3D OT as compared to a 2D configuration of the same OT setup.

The collected fluorescence signal originated from ACDAN along each orbit was used for the feedback-based tracking and, as a consequence, to reposition the orbit around the organelles and it was also stored in an 'intensity carpet' for further fluctuation analysis (Fig. 3.9A and B). In detail, classical Raster Image Correlation Spectroscopy (RICS) analysis[57,59] was performed on

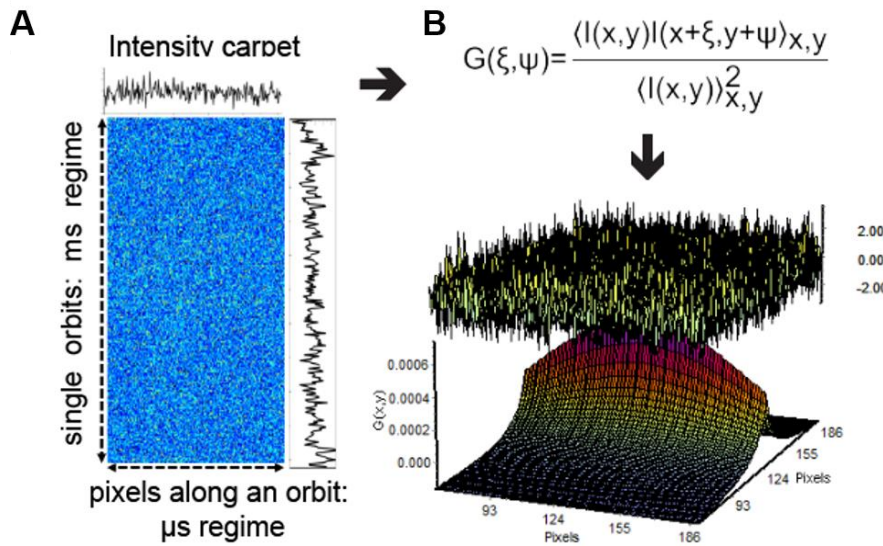

Figure 3.9 RICS analysis on OT fluorescent carpets. (A) Example of real ACDAN intensity carpet originated from the real tracking experiment reported in (Fig. 3.7B). (B) Circular-RICS general equation (Eq. 5), top. Circular-RICS autocorrelation curve fit of experimental data acquired in (A): plot of fit residues above and RICS fitting curve below.

ACDAN carpets (Fig. 3.9B) (hereafter referred to as circular-RICS). The obtained circular-RICS curves were then fitted using the typical circular-RICS autocorrelation curve model and this allowed us to obtain a quantitative estimate of ACDAN intra-lysosomal concentration and apparent diffusivity (hereafter indicated as 'D', $\mu m^2/s$). The point extrapolated at zero-time lag of the autocorrelation curve (or G_0) yielded an estimated concentration of ACDAN within the lysosome that was found to be around 6 µM (see Fig. 3.10 for the G_0 analysis).

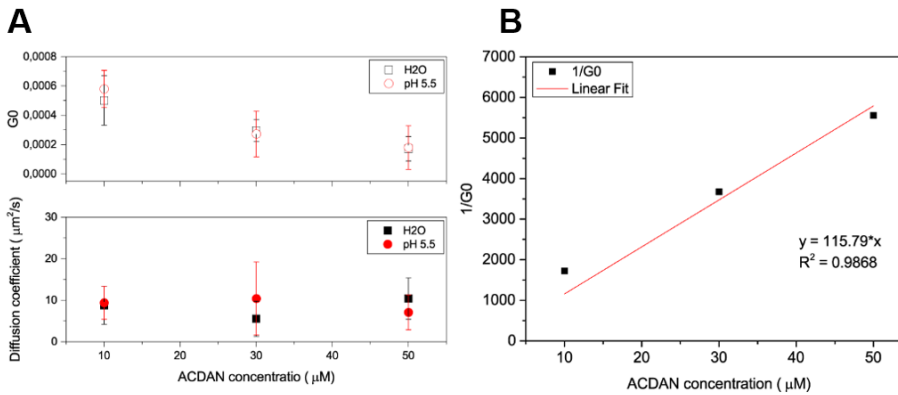

Figure 3.10 Viscosity calibration. (A) G0 analysis. G0 value decreasing as ACDAN concentration increases in aqueous solution of 66% sucrose in neutral (black) and acidic, pH 5.5, (red) conditions (top panel) instead diffusion coefficients remain constant (lower panel). (B) Calibration of G0 in 66% sucrose pH 5.5.

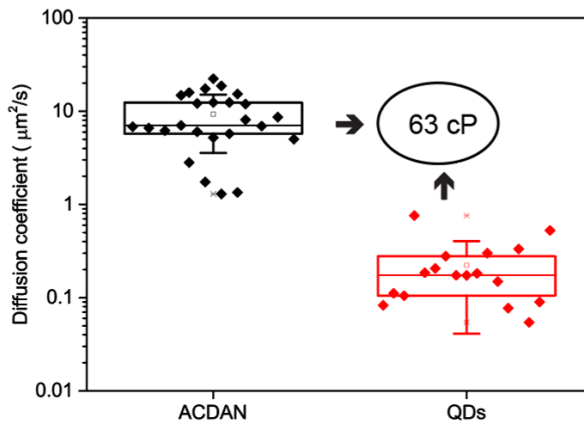

Figure 3.11 Diffusion coefficients of ACDAN and QDs inside lysosomes. Plot of the diffusion coefficients of ACDAN (black) and QDs (red) measured inside lysosomes of HeLa cells. Each point corresponds to a single measurement on a single lysosome. Upper and lower edges of the boxes represent the 25 and 75 percentiles of the distributions found, the middle line shows the median value, while the square inside the boxes are the mean values. Whiskers show standard deviations. 63 cP is the average viscosity value found using both QDs and ACDAN.

Concerning the apparent diffusivity, these measurements returned an average D of 9.3 ± 5.7 $\mu m^2/s$ (Mean ± SD, Fig. 3.11 black points). It is worth mentioning that ACDAN diffusivity may be in principle used to obtain an estimate of lysosomal internal viscosity, thus further validating the proposed experimental strategy.

In this regard, an estimate of ACDAN hydrodynamic radius was needed. This was obtained by performing circular-RICS measurements *in cuvette*, using ACDAN aqueous solutions at different concentrations of Sucrose (*i.e.*, 50, 55, 60 and 65% w/w), to obtain different viscosities. As reported in Fig. 3.12, D values decreased with increasing Sucrose concentration, as expected. Successively we inserted the resulting values inside the Stokes-Einstein relation:

$$D = \frac{k_B T}{6\pi\eta r} \quad \text{(Eq. 3)}$$

Here, the diffusion coefficient (D) is directly proportional to the temperature (T) at which the experiment is conducted through the Boltzmann constant (k_B), and is inversely proportional to both hydrodynamic radius (r) and solvent viscosity (η). A value of 0.43 nm was found for the hydrodynamic radius of ACDAN molecule. Later, relatively to the experiments performed on lysosomes of live cells, the value of the hydrodynamic radius was inserted, along with the D values obtained from the each OT experience in Eq. 3.The inversion of Eq.3 led to the an apparent viscosity of the tracked lysosome lumen of about 63 cP (ranging from a minimum of 40 cP to a maximum of 148 cP, Fig. 3.12), a value that nicely matches previous FLIM-based estimates obtained using molecular rotors[65].

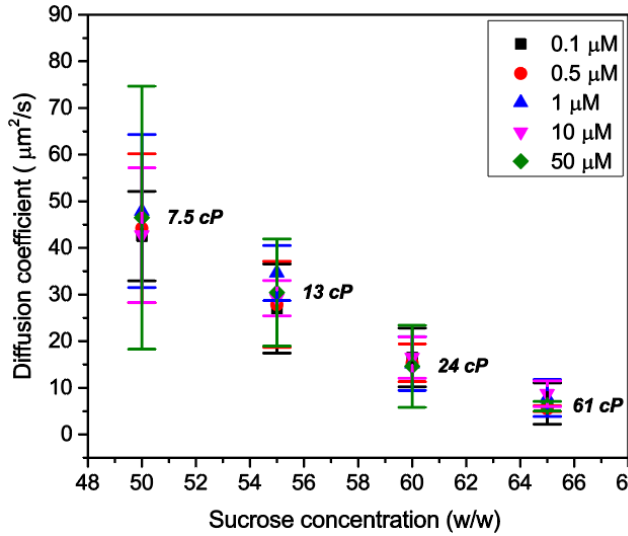

Figure 3.12. Diffusion coefficients of ACDAN measured at different viscosities. Average D values and SD (μm2/s) measured at different viscosities (i.e., different aqueous concentrations of Sucrose). Different colors represent different ACDAN concentrations (see legend on the top right).

To further validate this results, similar experiments were conducted with quantum dots (QDs). To this end, QDs were administered to culture medium and, later, a fraction of them spontaneously entered cells and ended up within lysosomes[84] (not shown).

The strong fluorescence emission of QDs was exploited to track lysosome position while performing fluctuation analysis to study the intralysosomal diffusivity of QDs (D= 0.22 ± 0.18 $\mu m^2/s$, Mean ± SD, Fig. 3.11 red points). In Combination with QD hydrodynamic radius (obtained from *in-cuvette* measurements, data not shown), QDs revealed exactly the same intralysosomal viscosity obtained using ACDAN as a probe[84].

In addition, analogous experiments were performed within the nucleus; in this experiment, the ISS system was left to scan the 3D orbits of the previously

described tracking setup in a fixed and random point inside cell nuclei (i.e., feedback-based 3D orbital tracking was not active during this experiment, while upper and lower orbits were left to scan the sample in a fixed point): as expected, these measurements revealed a less viscous and more heterogeneous environment characterized by a slightly larger distribution of D values (Fig. 3.13), in accordance with available literature[85].

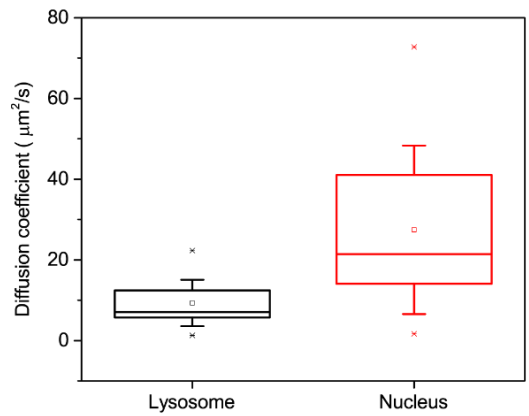

Figure 3.13 Viscosity of nuclei. Diffusion coefficients of ACDAN measured inside lysosomes (black) and nuclei (red) of HeLa cells. Upper and lower edges of the boxes represent the 25 and 75 percentile of the distributions found, the middle line shows the median value, while the square inside the boxes are the mean values. Whiskers show standard deviations. Image reprinted from ref.[84]

3.4 Concluding remarks

As demonstrated above, the combination of feedback-based 3D orbital tracking and circular RICS analysis revealed itself as a powerful tool to grab the dynamics of molecules within subcellular compartments which are trafficking within cells. As a matter of fact, this technique allows to achieve simultaneously (1) high spatial resolution, (2) high temporal resolution and (3) large volume sampling to follow the object of interest in 3D.

As we will demonstrate in the following Chapter, further combination of this approach with suitable fluorescent probes will allow to unveil peculiar physicochemical properties of these subcellular environments and their variation in time.

Chapter

4

Capturing metabolism-dependent solvent polarity fluctuations in the lumen of a trafficking lysosome in physiology and disease

Present knowledge suggests that the intraluminal solvent of lysosomes bears little resemblance of the surrounding cytoplasmic environment. First, the lysosome lumen represents a crowded aqueous environment, between 50- to 500-times more viscous than the cytoplasm[65,86]. Second, its lumen is highly polydisperse; its constituents can indeed reach different sizes that span several orders of magnitude, from sub-nanometer (ions, metabolites) to nanometers (proteins) to tens/hundreds of nanometers (enzymatic complexes, membrane fragments, nano sub-compartments)[87]. Third, metabolic activities

continuously drive the lysosome lumen far from thermodynamic equilibrium[88]. Thanks to these dynamic variations, the cell can reversibly shut down metabolism and respond to environmental cues[89].

In the last decades, a huge number of solvatochromic and fluorogenic dyes were developed to probe a variety of physicochemical parameters within the cell mainly by optical microscopy[90]. However, their employment as probes to detect solvent physicochemical properties within sub-cellular compartments at the timescale relevant to molecular processes (i.e. micro-to-millisecond regime) is, at present, an unattained task.

To probe the physicochemical properties of the lysosome lumen we adopted feedback-based 3D orbital tracking of single lysosomes labelled by ACDAN molecule. As stated in Chapter 3, ACDAN is particularly suited for the study of lysosomes.

In brief, Standard Generalized Polarization (GP) calculations[91] (explained in detail in the next sections) were herein used to quantify the ACDAN emission shift at any time point. Then, RICS[57] analysis was performed to extract characteristic dissipation time of ACDAN GP fluctuations in the lysosome lumen, analogously to what already done by others on membranes or within the cell cytoplasm using DAN probes[78,79,92–94]. For the first time intra-lysosomal solvent polarity fluctuations with characteristic dissipation times in the micro-to-millisecond range were unveiled. Control experiments demonstrate that polarity fluctuations are dependent on (acidic) lysosomal pH and metabolic energy in the form of ATP. In addition, we observed polarity fluctuations in live cells, but not in fixed ones. These results suggest that intra-lysosomal solvent polarity fluctuations depend on the ongoing metabolism. Besides shedding light onto the lysosome lumen, the strategy proposed here paves the way to a new spectroscopy approach for the investigation of the natural, yet elusive, biochemistry of living matter at the subcellular level.

4.1 The Twitcher model and preliminary time-tunable RICS analysis

Lysosomal Storage Disorders (LSDs) represent a set of rare diseases that, due to alteration in a gene sequence, result in lysosomal malfunctioning. To provide an example of a possible application towards a more biomedical orientation, we analyzed the diffusion coefficients of Lysotracker inside lysosomes of fibroblast cells harvested from Twitcher mice, used as model for Krabbe disease (Fig. 4.1). As a preliminary test, Lysosomes of Twitcher cells were studied using time-tunable RICS with the same parameter setting described in Chapter 2.

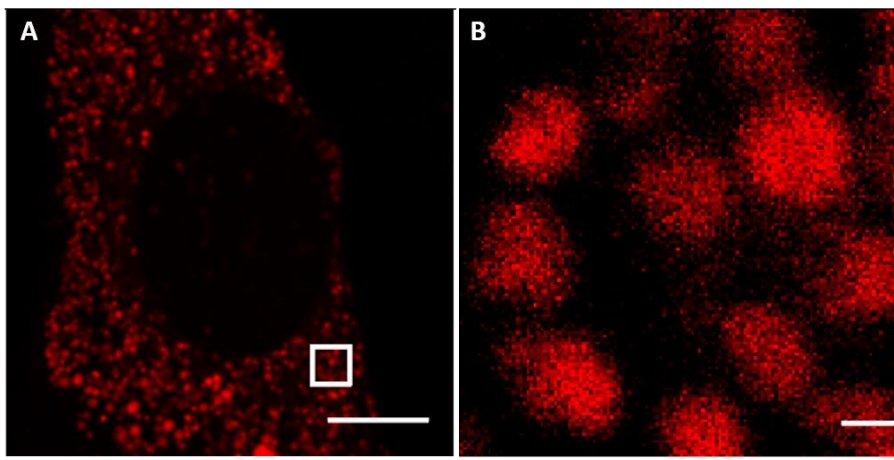

Figure 4.1 Red Lysotracker in lysosomes of Twitcher fibroblast treated with Psycosine. (A) Confocal image of a Twitcher Fibroblast cells labelled with Red Lysotracker (scale bar 10 μm). (B) Magnification of figure A, white square. This is the magnification used for time-tunable RICS experiments (*i.e.*, 33 nm per pixel).

In parallel, Wild Type (WT) fibroblasts were used as a control. As reported in Fig. 4.2, Lysotracker showed lower diffusion coefficients inside lysosomes of Twitcher cells (blue dots) when compared to the WT case. This automatically translates in a higher viscosity of lysosomes of Twitcher cells (Eq. 3,section 2.1.1).

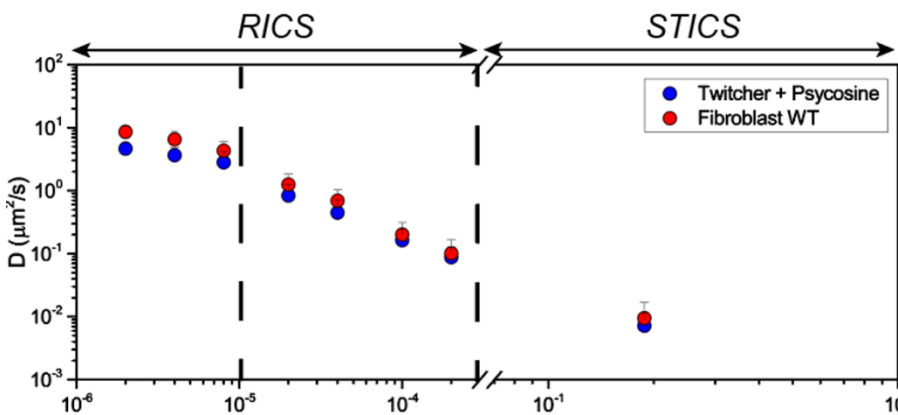

Figure 4.2 Diffusivity of Red Lysotracker in lysosomes of Twitcher fibroblast treated with Psycosine. This graph shows the Diffusion coefficients found for both Twitcher Fibroblasts treated with Psycosine (blue dots) and Wild Type Fibroblasts (red dots) at different sampling time. Note the distinction between RICS and STICS time domains. Notice how Twitcher cells show, in general, lower diffusion coefficients, thus resulting in a more viscous environment compared to WT case.

Fig. 4.3 shows the statistics of diffusion coefficients found at 2 μs per pixel dwell time. Lysosomes of WT cells showed an average diffusion coefficient two times higher than the average value of Twitcher cells, thus a viscosity of the Twitcher case two times higher, in agreement with the results presented by Devany et al.[86] where a factor four of difference was found using a completely different technique.

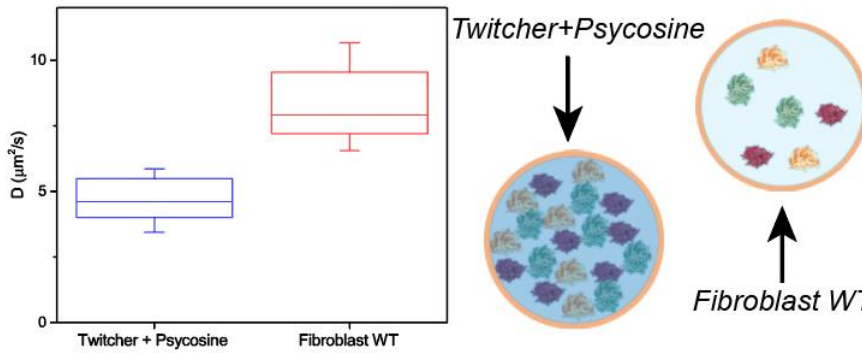

Figure 4.3 Diffusion coefficients of Red Lysotracker inside the lumen of Twitcher cells treated with Psycosine compared to WT cells. Plot of the diffusion coefficients of Twitcher Fibroblast treated with Psycosine (blue) and Wild Type Fibroblast (red) measured on lysosomes of HeLa cells obtained at 2 μs of pixel dwell time. Upper and lower edges of the boxes represent the 25 and 75 percentiles of the distributions found, the middle line shows the mean value. Whiskers show standard deviations (left side). Schematic representation of the two distinct situations (right side). The mean value of the diffusion coefficient of WT cells almost doubles the value of the Twitcher case.

4.2 Circular-RICS on ACDAN GP carpets

Once the viscosity of lysosomes contained in WT and Twitcher fibroblasts was retrieved using time-tuneable RICS on a population of labelled lysosomes, our analysis focused on exploiting the combination of feedback-based 3D orbital tracking to jump onto the reference system of a single organelle.

The exquisite sensitivity of ACDAN to environmental polarity was exploited here to extract the dynamic behaviour of the solvent in the lumen of the single trafficking lysosome (Fig. 4.4).

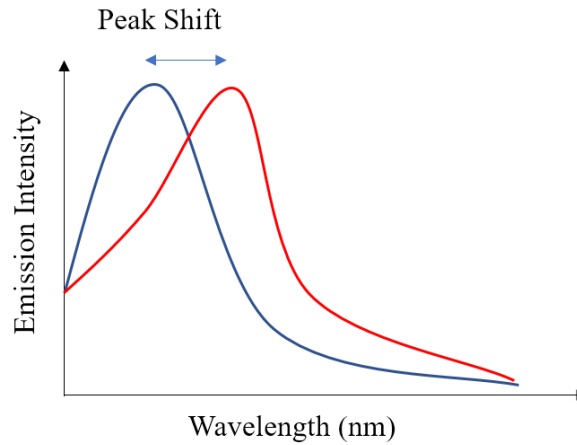

Figure 4.4. Emission Peak shift of ACDAN. Schematic representation of the shift of the ACDAN emission spectrum due to a different environmental polarity.

To this end, the ACDAN fluorescence signal was split into two channels (CH1: 400-470 nm and CH2: 475-545 nm) that were then combined into a GP image following Eq. 6:

$$GP = \frac{CH2-CH1}{CH2+CH1} \quad \text{(Eq.6)}$$

A typical GP map obtained by standard confocal imaging of an entire cell is reported in Fig. 4.5. The same analysis can be performed on single lysosomes, as reported in the scheme of Fig. 4.6. These latter measurements yielded, in our case, an average GP value in lysosomes of approximately 0.04. To calibrate this result, we evaluated *in-cuvette* the fluorescence emission of ACDAN in different protic and aprotic solvents. GP was extracted from the acquired emission spectrum (for further details see Appendix B) and plotted

against the solvent dielectric constant (not shown). ACDAN fluorescence emission showed a clear dependence on environment polarity.

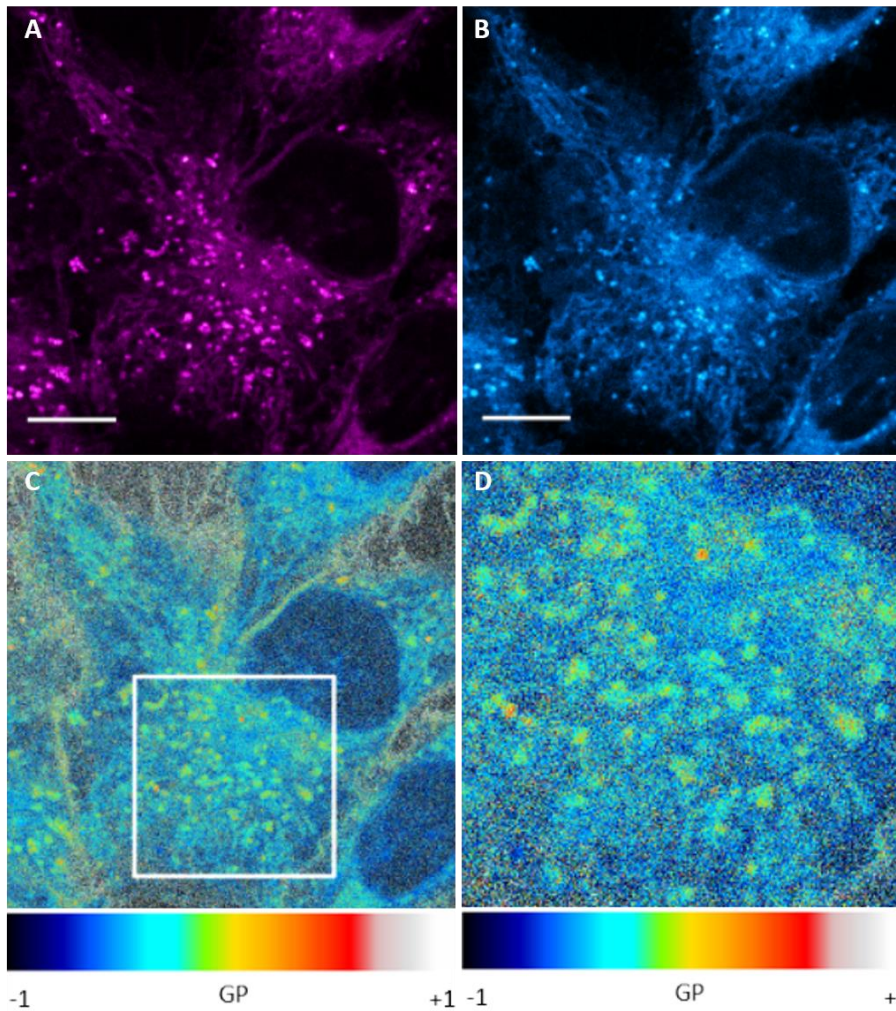

Figure 4.5 GP maps on live HeLa cells. (A−C) Confocal microscopy images of HeLa cells labelled with ACDAN. (A) CH1 representing wavelength values ranging from: 400 to 470 nm. (B) CH2 collection range: 475−545 nm. (C) GP image obtained by applying Eq.6 to images in (A) and (B). LUT of GP values is reported on the bottom. (D) Zoom of the area enclosed within the white square in (C). LUT of GP values is reported on the bottom.

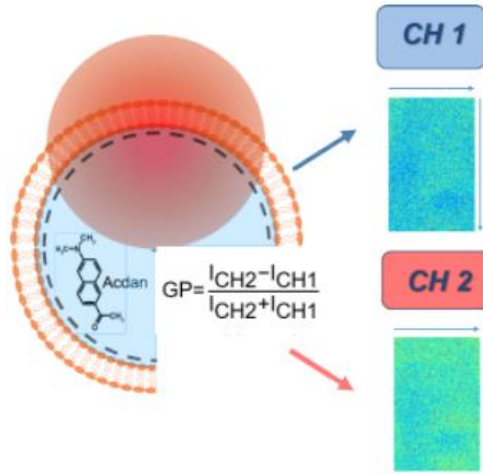

Figure 4.6 Schematic representation of GP analysis on a single Lysosome. Scheme of the feedback-based 3D orbital tracking setup for GP acquisitions (with GP equation). CH1 and CH2 denote the two different acquisition ranges (400−470 nm for CH1 and 475−545 nm for CH2) and thus the two different fluorescence carpets acquired.

Interestingly, the GP of ACDAN in lysosomes (0.04) was not far from the GP of ACDAN measured both in DMSO (aprotic, GP=0.09) and 3-Methyl 1-Butanol (protic, GP=0.35): two solvents with dielectric constants (46.7 and 15.2, respectively) far from that typical of lipids (which is known to be around 2), further corroborating the idea that ACDAN is not embedded in the lipid bilayer. At this point, feedback-based 3D orbital tracking was used to probe the GP evolution in time in single lysosomes. During these sets of experiments, ACDAN fluorescence signal collection was split in 2 channels: CH1 and CH2 as shown in Fig. 4.5 and 4.6. Of note, the ACDAN fluorescence of CH1 was used as a source of signal for the feedback of 3D orbital tracking and GP analysis, while Red Lysotracker was used to univocally identify lysosomes before performing the tracking measurement. In detail, GP was calculated pixel-by-pixel along the orbit by using the Eq. 6.

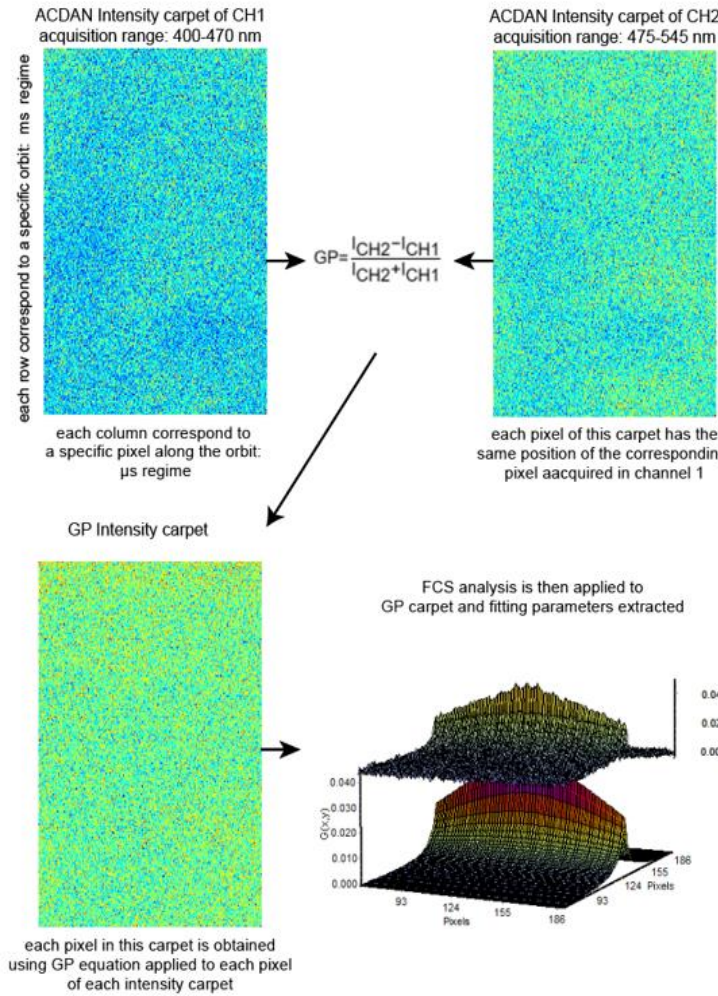

Figure 4.7 GP analysis workflow. The two carpets of ACDAN corresponding to Channel 1 (CH1, range: 400-470 nm, top left) and Channel 2 (CH2, range: 475- 545 nm, top right) are combined using Eq. 6 to obtain the GP carpet (bottom left). This carpet is then analyzed using circular-RICS (bottom right).

Then, the GP values for each pixel along the orbit were organized in a 'GP carpet' that was finally processed by fluctuation spectroscopy (Fig. 4.7).

Notably, circular-RICS analysis highlights the occurrence of GP fluctuations in the lumen of trafficking lysosomes. By Eq. 7 we were able to extract the characteristic dissipation time given of GP fluctuations:

$$\tau = \frac{w_0^2}{4D} \quad \text{(Eq. 7)}$$

Here w_0 is the radial waist of the laser beam profile (in this case 0.3 μm). Fig 4.8A shows the characteristic dissipation time and the amplitude (G_0) of such fluctuations for lysosomes measured in HeLa cells under physiological conditions. Fig 4.8A shows the characteristic dissipation time and the amplitude (G_0) of such fluctuations for lysosomes measured in HeLa cells under physiological conditions. GP fluctuation analysis returned a broad distribution of characteristic dissipation times ranging from micro milliseconds to tenths of seconds (blue dots in Fig. 4.8A), with two main population discernible as ‘slow’ and ‘fast’ (Fig. 4.8A). Concerning the characteristic amplitude of the polarity fluctuations, the obtained G0 values are distributed around an average value of about 10^{-3}. Please note that this amplitude is of the same order of magnitude of that previously measured in the cytoplasm of yeast cells by ACDAN GP analysis, even if on a different timescale (i.e. seconds)[78,79]. However, an overall increase in the GP fluctuation amplitude was detected in the ‘slow’ population when compared to the ‘fast’ (see horizontal blue lines in Fig. 4.8A).

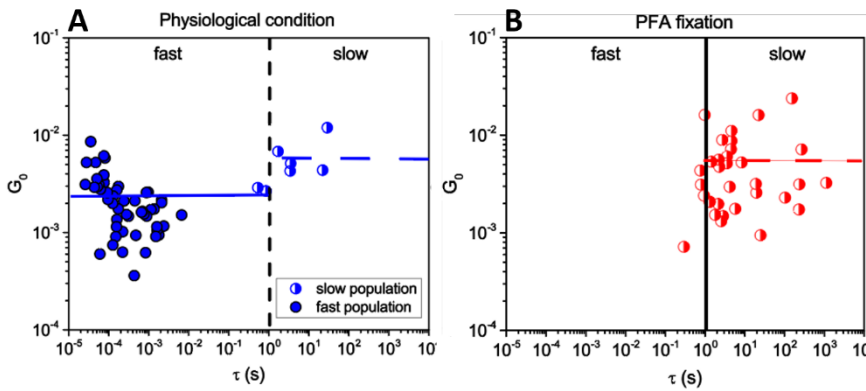

Figure 4.8 G_0 vs τ for cells cultured in physiological conditions and for fixed cells.
(A-B) G0 vs τ plot showing the results of the circular-RICS analysis performed on ACDAN GP carpets originated by feedback-based 3D orbital tracking measurements of lysosomes of HeLa cells cultured under physiological conditions (blue dots in A) and on HeLa cells fixed with PFA (red dots in B), respectively. The continuous vertical black line in (B) shows the limit threshold identified by means of the statistical analysis of data from fixed cells (placed at τ = mean − SD). Such threshold identifies two regions of the G0 vs τ plot which are mostly populated by slow fluctuations ("slow" region) and fast fluctuations ("fast" region), respectively. It is used as a reference in all plots.

Several control experiments were performed to assess the nature of the polarity fluctuations observed in the lysosome lumen. A first control experiment was conducted *in cuvette*, using an aqueous solution of 66% (w/w) Sucrose. ACDAN was dissolved in this Sucrose solution at a concentration of 6-µM ACDAN. While ACDAN diffusivity was correctly extracted from the intensity carpets, as expected, in absence of any cellular component, no detectable GP fluctuations was present (data included as 'ND' in Table 4.1).

A second control measurement was performed on paraformaldehyde-fixed cells, intended as a condition that preserves lysosome structural identity (Fig. 4.8B) while physically blocking its molecular components (e.g. enzymes of the lumen) and, as a consequence, all ongoing dynamic processes. Of note, under this limit condition, polarity fluctuations in 'fast' regime were completely absent. Instead, circular-RICS analysis highlighted a remarkable shift of the experimental points towards very 'slow' GP fluctuations (red dots in Fig. 4.8B). These experiments clearly showed that polarity fluctuations in the micro-to-millisecond range were only present within living cells. The region of the G_0-*vs*-τ plot relative to the experiment on fixed cells (Fig. 4.8B) was also used to derive a reference threshold, identified at a τ-value corresponding to the Mean - SD (continuous black line in the plot, at τ=1.05 s), above which the method probes phenomena that are of no interest for the present analysis. The region of the G_0-*vs*-τ plot on the left of this threshold is hereafter referred to as the 'fast' region; the region on the right, by contrast, is referred to as the 'slow' region. Please note, in fact, that experimental data points from cells in physiological conditions almost entirely fall within the fast region of the G_0-*vs*-τ plot, in a time scale (10^{-6} -10^{-3}s) relevant for enzyme action and for complementary, simultaneous, reorganization of the protein solvent proximity. This suggests that intralysosomal GP fluctuates in space and time as a result of the complex molecular processes occurring in live cells and their spatiotemporal regulation.

Study on HeLa cells								
	Viscosity study		GP analysis					
	Viscosity (cP)		τ (s) min-max		% Population		Average GP	
	Mean	Range	Slow	Fast	Slow	Fast	Mean	SD
Physiologic. condition	63	40-148	0.5 - 28	$3\cdot10^{-5}$ - $7\cdot10^{-3}$	11	89	0.04	0.02
Sodium Azide	58	35-161	$1\text{-}22\cdot10^{3}$	$5\cdot10^{-5}$ - $2\cdot 10^{-3}$	85	15	0.05	0.03
Chloroquine	57	34-148	$1\text{-}20\cdot10^{3}$	$4\cdot10^{-5}$ - $5\cdot10^{-3}$	82	18	0.04	0.02
Osmotic Shock	48	29-130	$0.3\text{-}2\cdot10^{3}$	$4\cdot10^{-5}$ - $3\cdot10^{-3}$	56	44	0.05	0.03
Physiologic. Cond. Nuclei	19	11-83	0.5-227	$1\cdot10^{-5}$ - $10\cdot10^{-3}$	30	70	0.04	0.01
PFA Fixation	ND	ND	$5\text{-}24\ 10^{3}$	ND	100	0	0.13	0.04
66%(w/w) Sucrose	60	40-90	ND	ND	ND	ND	0.71	0.01

Table 4.1 Results on Hela cells. The upper part of the table shows the results from RICS analysis on OT carpets of ACDAN fluorescence emission. Viscosity estimates are derived by Eq. 4, using the diffusion coefficients reported in Fig. 3.11. The middle part shows the results from RICS analysis on GP carpets of ACDAN emission signal. For both the 'fast' and 'slow' populations, the range of characteristic GP fluctuation times (τ), and the fractional population contributions are reported. Finally, in the lower part, the average GP values retrieved from 3D feedback-based ACDAN imaging of single lysosomes are reported for all tested conditions. ND stands for Not Determined. Table reprinted from ref.[84]

4.3 ACDAN GP fluctuations and metabolic activity

In the following, a series of control experiments are reported to address the potential link between ACDNA GP fluctuations and the metabolic activities ongoing within the single organelle. In a first experiment, cells were treated with Sodium Azide, a well-known blocker of ATP production (Fig. 4.9, 4.10 and Table 4.1). ACDAN and Lysotracker proved to be stable markers of the lysosome even under these conditions. In particular, upon energy depletion (*i.e.*, ATP depletion), 'fast' GP fluctuations almost completely disappear: ~85% of the retrieved values fell within the 'slow' region of the G_0-*vs*-τ plot, the one characteristic of fixed cells. It must be observed that ATP depletion is a generic treatment that inhibits all active processes within the cell; alternatively, chloroquine is a molecule that specifically affects lysosomal metabolism: it possesses indeed the ability to inhibit many lysosomal enzymes (mostly hydrolases) by raising the intraluminal pH[95]. Notably, results obtained in presence of 50-μM chloroquine nicely correlate with those reported upon ATP removal (Fig. 4.9, 4.10 and Table 4.1): the fraction of fast GP fluctuations (fast region) drops to ~18%.

A third experiment was then performed under osmotic shock conditions. Here, pure water was added to the cell medium inducing, as a consequence, an increase in the amount of water contained within the lysosome lumen. As a direct consequence, an increase of the average size of lysosomes was evident: as a matter of fact, we had to adjust and increase the orbit radius from 150 to 200 nm. In addition, a ~20% increase of the average GP value as compared to the physiological condition (Table 4.1) was also observed. Still, this was not regarded as an experimental condition able to directly affect lysosomal activity and metabolism (at least not to the same extent of previous control experiments). In this regard, the fraction of fast GP fluctuations almost doubled (44% Fig. 4.9, 4.10 and Table 4.1) the fraction of fast measurements

registered with ATP removal and lysosome basification, thus probably supporting the continued presence of a residual lysosomal activity.

Overall, these experiments strongly suggest a link between the measured solvent polarity fluctuations and active, pH-dependent, intralysosomal processes. It is worth noting that the average absolute value of ACDAN GP was quite similar among all the conditions tested a part from a slight increased with cells undergoing osmotic shock.

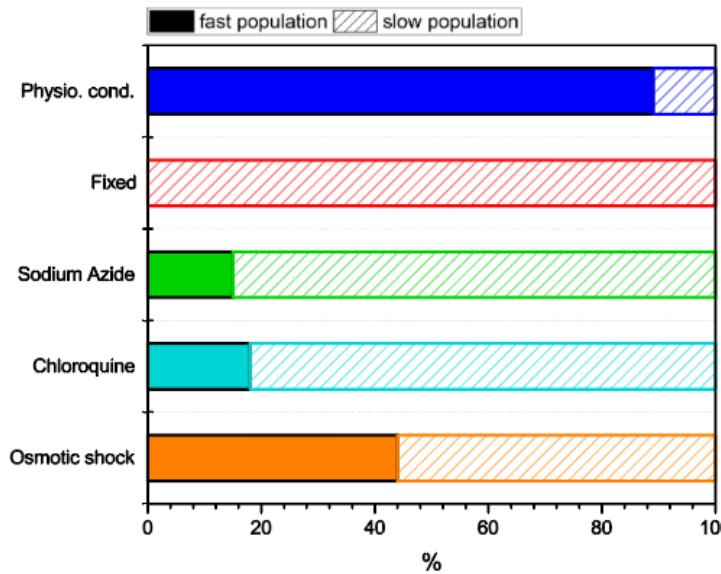

Figure 4.9 Percentage of 'fast' and 'slow' populations derived from Circular-RICS analysis of ACDAN GP carpets on lysosomes of HeLa cells cultured under different physiological conditions. Plot summarizing the fractions of experimental points that fell within the "fast" region (filled histogram) and "slow" region (dashed histogram) of the G0 vs τ plot for all the experimental conditions.

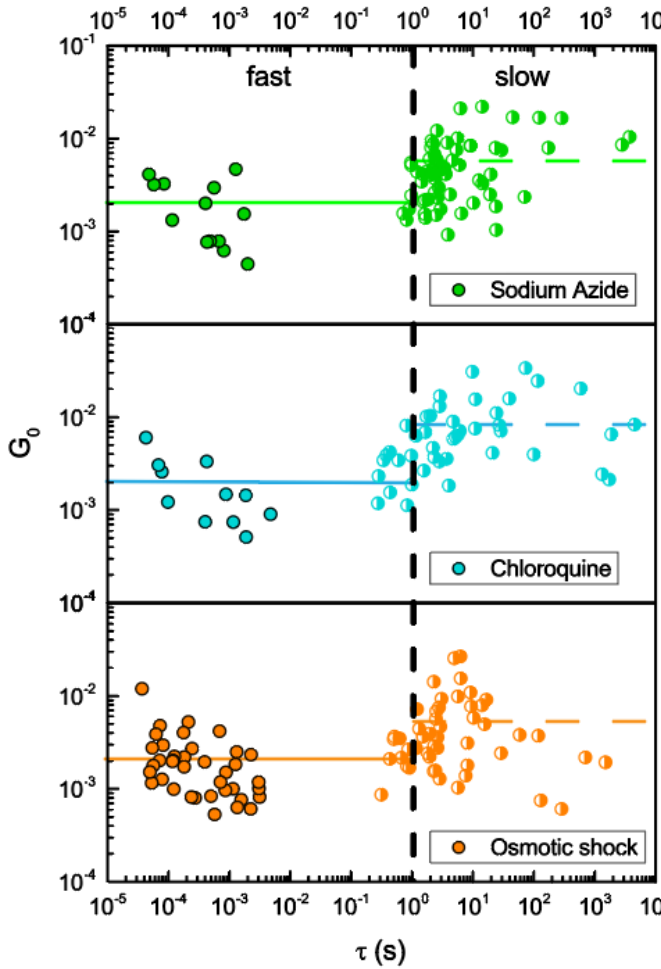

Figure 4.10 Circular-RICS analysis of ACDAN GP carpets derived from lysosomes of HeLa cells cultured under different physiological conditions. G0 vs τ plot of the GP fluctuation results obtained in HeLa cells treated with sodium azide (green dots), chloroquine (cyan dots), and osmotic shock (orange dots). The dashed black line indicates the limit threshold (mean − SD) already presented in Fig. 4.7.

4.4 ACDAN GP fluctuations in a cellular model of LSD

Having obtain these robust results, our focus was once again directed to the murine cell model of Krabbe disease (KD, or globoid cell leukodystrophy; OMIM#245200); as known, KD represents a rare metabolic disorder characterized by the loss of function of the lysosomal hydrolase galactosylceramidase (GALC; E.C. 3.2.1.46). This deficiency leads, in turn, to the accumulation of undigested biomaterial inside the organelles and the cell[96,97]. As described in detail in the Appendix B, primary fibroblasts were extracted from the ears of wild-type (WT) and Twitcher (TWI) mice, the latter being a recognized naturally occurring animal model for the study of KD[98,99]. In particular, WT fibroblasts were cultured under normal conditions, while TWI fibroblasts were exposed to 100 μM psychosine (PSY) for 24 h previously to image acquisition in order to exacerbate and better reproduce the KD phenotype. This treatment allows to mimic, in the fibroblast model, the toxicity typically elicited by the abnormal accumulation of PSY in the glial cells of the nervous system (considered to be the primarily responsible for the pathogenesis)[100]. In both cell preparations, ACDAN (and Lysotracker) proved to be an excellent lysosomal marker, as also showed in Fig. 4.11A-H. Again, the fluorescence emission originated from ACDAN molecules within the lysosomes was used as a feedback signal to perform feedback-based 3D orbital tracking and, later, FCS analysis.

Fitting of the circular-RICS autocorrelation curves yields an ACDAN intralysosomal apparent D of 9.4 ± 4.2 μm2/s in WT cells and 6.9 ± 2.9 μm2/s in TWI cells treated with PSY. These values combined with Eq. 3 and the apparent hydrodynamic radius of ACDAN allowed for an estimate of the apparent viscosity of the lysosome lumen: 54 cP in WT cells (ranging from a minimum of 37 cP to a maximum of 98 cP, Fig. 4.12A and Table 4.2) and 73 cP in TWI cells treated with PSY (ranging from a minimum of 51 cP to a maximum of 123 cP, Fig. 4.12A and Table 4.2). This increased value of

viscosity observed in lysosomes of TWI cells as compared to WT ones (~35%) supports the idea that the lysosome lumen may be more crowded (and thus more viscous) due to the accumulation of undigested lipids occurring in TWI cells and this well agrees with recent results obtained using nanoherology, on lysosome viscosity in a different LSD [86].

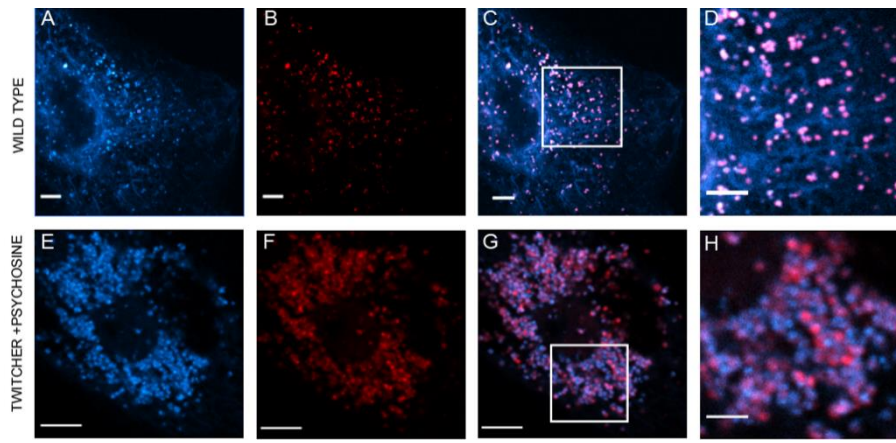

Figure 4.11 ACDAN as a fluorescent probe to sense the metabolism of lysosomes in a cellular model of LSD. Confocal microscopy images of WT primary fibroblasts labelled with ACDAN (A) and LysoTracker (B) and the corresponding overlay of the two signals (C). Scale bar 5 μm. (D) Zoom of a cytoplasmic region corresponding to the white square in (C) showing labeled lysosomes. Scale bar: 2 μm. (E−H) Confocal microscopy images of psychosine-treated primary fibroblasts from Twitcher mice, labelled with ACDAN (E) and LysoTracker (F), with the corresponding overlay of the two signals (G) (scale bar: 5 μm) and zoom from a cytoplasmic region corresponding to the white square in (G) showing labelled lysosomes also in this case (H). Scale bar: 2 μm).

Notably, treating WT fibroblasts with sodium azide, chloroquine, and osmotic shock returned the same results obtained in HeLa cells (see Fig. 4.13 and 4.14). Following this experimental validation of the LSD cell model, feedback-based 3D orbital tracking was again used to probe the GP evolution in time, in single lysosomes. As expected, also in this case, circular-RICS

analysis on GP carpets originated by ACDAN fluorescence emission produced a similar broad distribution of characteristic GP dissipation times (from micro to milliseconds) in the lumen of trafficking lysosomes in WT fibroblasts as the one obtained for HeLa cells (Fig. 4.8). Although the distribution of dissipation time showed the same range of values, results obtained on lysosomes of WT fibroblasts marked slight imbalance in favor of the "slow" fluctuations (*i.e.*, the 57% of the total), contrary to what observed in HeLa cells (compare statistics reported in Tables 4.1 and 4.2). Interestingly, in TWI fibroblasts, the fractional contribution of the "slow" GP population increased as compared to WT cells, reaching 70% of the total data collected. The results collected so far may find an interpretation again with lysosome metabolism; in TWI cells indeed the metabolism of lysosomes is impaired as compared to the WT case. This causes the lysosome lumen of TWI fibroblast to be more crowded (as testified also by the average GP value retrieved from orbital tracking measurements, see Table 4.2).

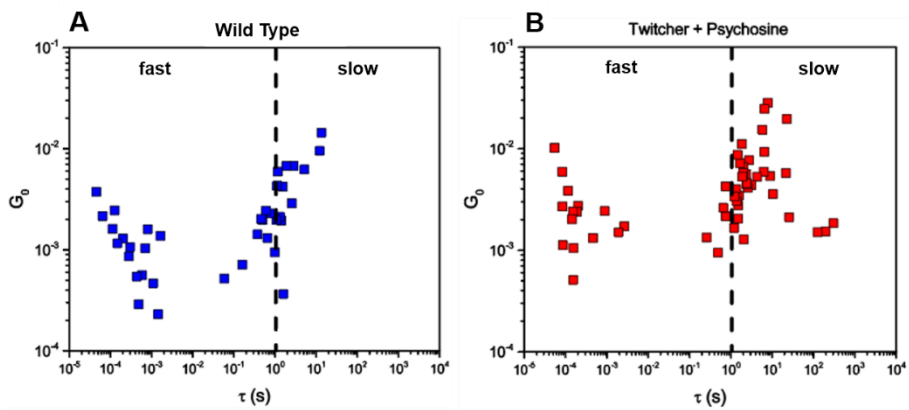

Figure 4.12 Circular-RICS analysis of ACDAN GP carpets derived from lysosomes of Twitcher and WT fibroblasts. G0 vs τ plot showing the results of the GP analysis performed on WT fibroblasts (blue squares) and psychosine-treated Twitcher fibroblasts (red squares), respectively.

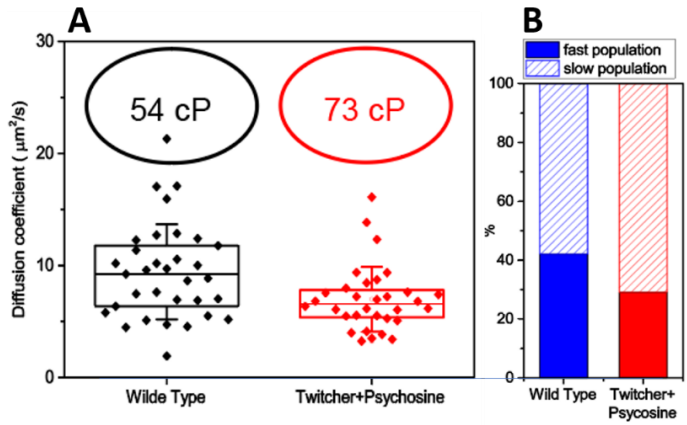

Figure 4.13 FCS analysis of ACDAN fluorescence from WT and Twitcher fibroblast. (A) Plot of the diffusion coefficients of ACDAN measured within lysosome lumen of both WT (black dots) and Twitcher (red dots) cells. Each point corresponds to a single measurement on a single lysosome. Upper and lower edges of the boxes represent the 25 and 75 percentiles of the distributions, respectively; the middle line indicates the median value; whiskers are standard deviations. As reported in the graph, 54 cP (values ranging from 37 cP to 98 cP) is the average viscosity in lysosomes of WT fibroblasts, and 73 cP (values ranging from 51 cP to 123 cP) is instead the average viscosity in psychosine-treated Twitcher fibroblasts. (B) Plot summarizing the fractions of experimental points falling within the "fast" region (filled) and "slow" region (dashed) of the G0 vs τ plot for the two tested conditions.

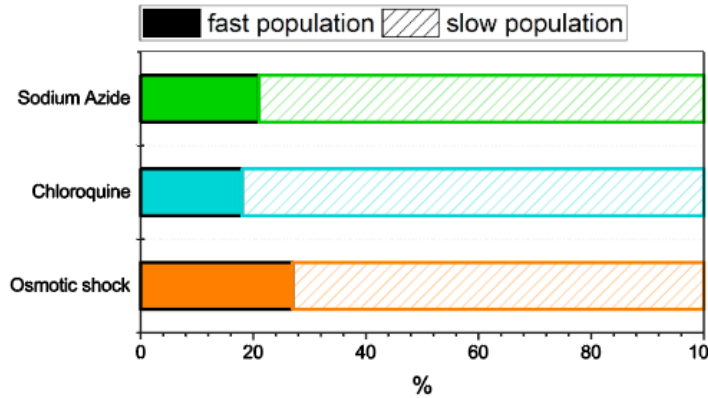

Figure 4.14 Percentage of 'fast' and 'slow' populations derived from Circular-RICS analysis of ACDAN GP carpets on lysosomes of HeLa cells cultured under different physiological conditions. Graph showing the fraction of experimental points classified as 'fast' fluctuations (filled portion of the histogram) and 'slow' (dashed portion) for all the conditions analyzed. Refer to Table 4.2 for a complete summary of the results obtained using WT and TWI (+PSY) fibroblasts.

Study on Fibroblasts cells								
	Viscosity study		GP analysis					
	Viscosity (cP)		τ (s) min-max		% Population		Average GP	
	Mean	Range	Slow	Fast	Slow	Fast	Mean	SD
Wild type Phys. Cond.	54	37-98	0.1 – 14	$4 \cdot 10^{-5}$ - $2 \cdot 10^{-3}$	43	57	0.05	0.02
Twitcher + Psychosine	73	51-123	0.3-304	$5 \cdot 10^{-5}$ - $3 \cdot 10^{-3}$	30	70	0.04	0.02

Table 4.2 Summary of results on WT and Twitcher fibroblasts. Similarly to Table 1, the upper part of the table shows the results from RICS analysis of ACDAN diffusion both in wild-type and Twitcher fibroblasts. Viscosity estimates are obtained with Eq. 3using the diffusion coefficients reported in Fig. 3.11A. The middle part shows the results from RICS analysis of ACDAN GP. For both the "fast" and "slow" populations, the range of characteristic GP fluctuation times (τ) and the fractional population contributions are reported. In the lower part, the average GP values retrieved from 3D feedback-based ACDAN imaging of single lysosomes are reported. Table reprinted from ref.[84]

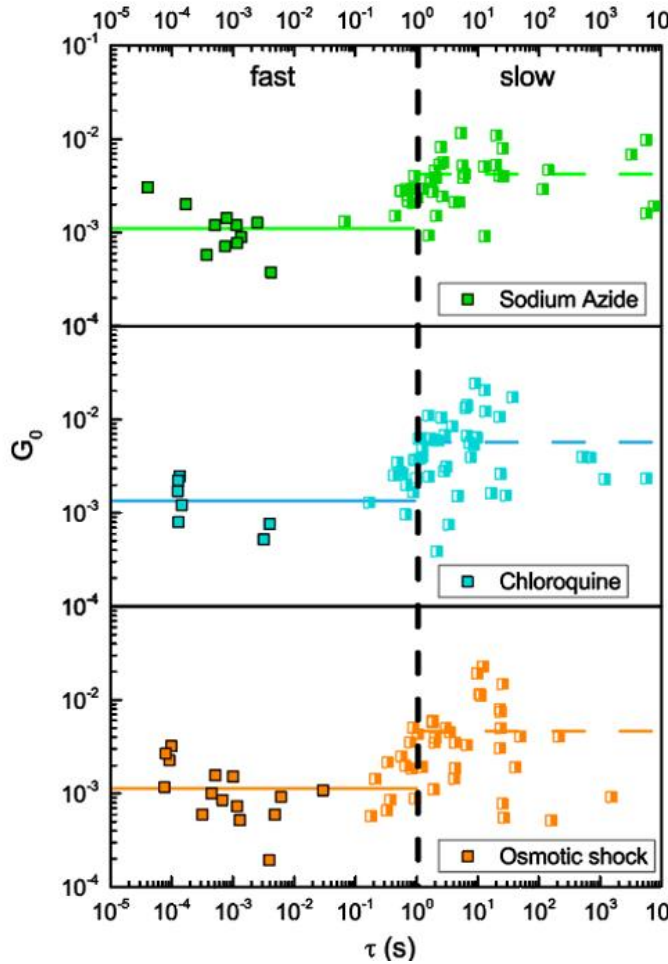

Figure 4.15 Circular-RICS analysis of ACDAN GP in fibroblasts. G0-vs-τ plots showing the results of the FCS analysis performed on ACDAN GP carpet obtained with OT on WT fibroblasts treated with Sodium Azide (green squares), Chloroquine (cyan squares) and osmotic shock (orange squares). In all plots, the dashed black line shows the limit threshold (Mean - SD) identified by the experiment on fixed HeLa cells, as explained in Fig. 4.8.

Besides, a consideration on the values of G_0 obtained for this LSD model is due. As a matter of fact, the characteristic amplitude of the GP fluctuations, were distributed similarly to those previously measured in HeLa (see Fig. 4.14), however, it is found that TWI cells have a substantially higher amplitude of the GP fluctuation as compared to WT cells (see dashed lines in Fig. 4.11).

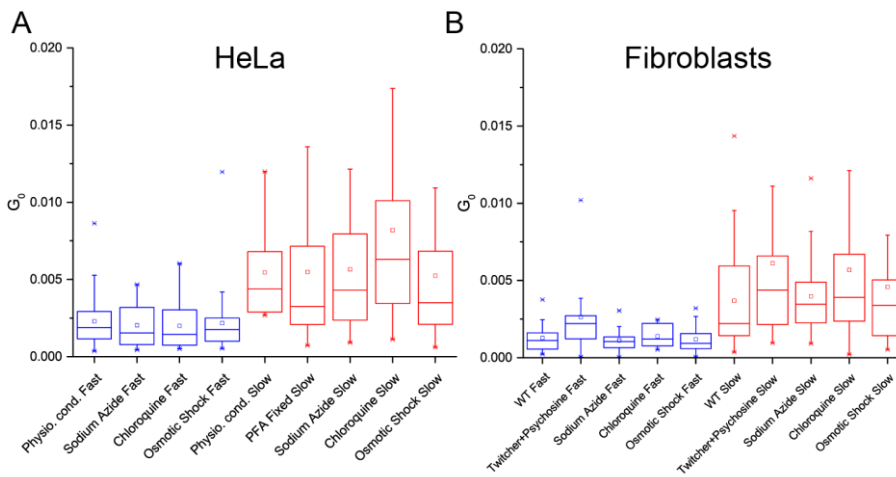

Figure 4.16 G0 analysis for all the experimental conditions tested. Plot of the G0 values of ACDAN measured inside lysosomes of HeLa cells (A) and Fibroblasts (B). G0 values of fast populations are reported in blue while those of slow populations are shown in red, for all the experimental conditions tested. Upper and lower edges of the boxes represent the 25 and 75 percentiles of the distributions, respectively; the middle line indicates the median value; the square inside the box shows the mean value; whiskers are standard deviations. Image reprinted from ref.[84]

4.5 ACDAN-GP data interpretation

The molecular mechanisms that drive GP fluctuations of ACDAN in lysosomes are important and deserve a brief discussion. As previously demonstrated by Parasassi and coworkers[80], the GP is sensitive to dipolar relaxation phenomena occurring in the surroundings of DAN probes. In this sense, the authors used Laurdan (*i.e.*, a DAN probe) and gel-to-liquid phase transitions in membranes under controlled conditions of water penetration, to successfully combine DAN dipolar relaxation to the presence of water molecules with restricted mobility (restricted with respect to bulk-phase water) in the bilayer region where the probe was located[80]. A similar approach was adopted by Thoke and co-workers to explain ACDAN GP fluctuations in the cytoplasm of *Saccharomyces cerevisiae* during glycolysis, although on a different time scale. In particular, GP fluctuations were interpreted as fluctuations in the dynamics of intracellular water and the mechanism validated by replacing H_2O with D_2O in the cells[78,79]. Such interpretation may in principle be transferred to the data shown here on the lysosome lumen. Supposing a rather constant chemical/molecular identity of the organelle during the measurement (few seconds), the dynamics of solvent dipolar relaxation extracted by circular-RICS analysis suggests a connection with the dynamics of the intraluminal molecular components, in particular of water, being a ubiquitous and major constituent of subcellular organelles and of living beings in general. In this regard, the GP fluctuation amplitude depends on the characteristic size of the fluctuating domain (Fig. 4.15), analogously to what already proposed by others when measuring Laurdan GP fluctuations due to lipid domains diffusing on the cell membrane[94].

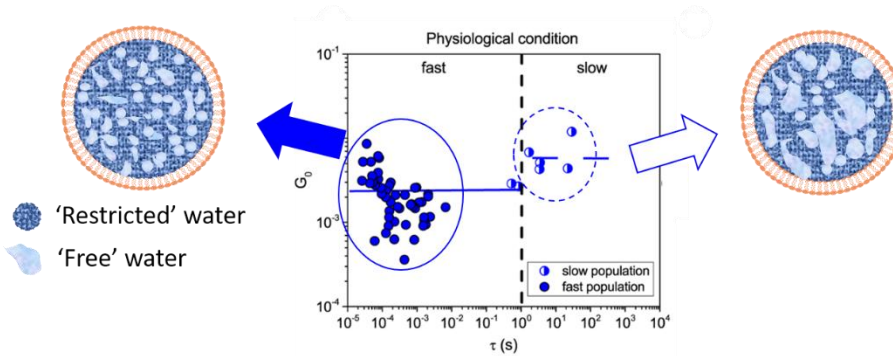

Figure 4.17 Interpretation of the solvent polar relaxation dynamics found in the experiments. As described in the text, faster solvent polar fluctuations can be linked to small water domains distributed heterogeneously within the lysosome lumen (left), while slower fluctuations can be reconducted to bigger water domain contained in inactive (or energy depleted) lysosomes.

In addition, if one considers also the time dependence, small domains are expected to produce fast fluctuations with low amplitude (e.g., the "fast" GP fluctuation population), and large domains slow fluctuations with large amplitude (e.g., the "slow" GP fluctuation population). The measured GP fluctuations therefore probe the local swings of the physicochemical properties of the milieu driven by the metabolic activity; this is expected to occur in the whole cell although with different characteristic spatial and temporal scales. To this end, we conducted a preliminary analysis within the nucleus of HeLa cells labelled with ACDAN. Fig. 4.16 highlights fluctuations of solvent dipolar relaxation in this compartment; nevertheless, characteristic timing and amplitude showed slightly different values when compared to the lysosome. In general, the available literature supports the idea that a variety of mesoscale organizational levels do exist within the cell that include as obvious canonical membrane-bound organelles that contribute to the spatiotemporal regulation of molecular processes as well. For instance, the

cytoplasm is now regarded as an heterogeneous environment, where solutes (such as proteins) are likely bound to scaffold structures (e.g., membranes, cytoskeleton) rather than freely diffusing and colliding, thus allowing for the formation of complementary nanoscopic "pools" of solvent (i.e., water) with bulk-like properties[60].

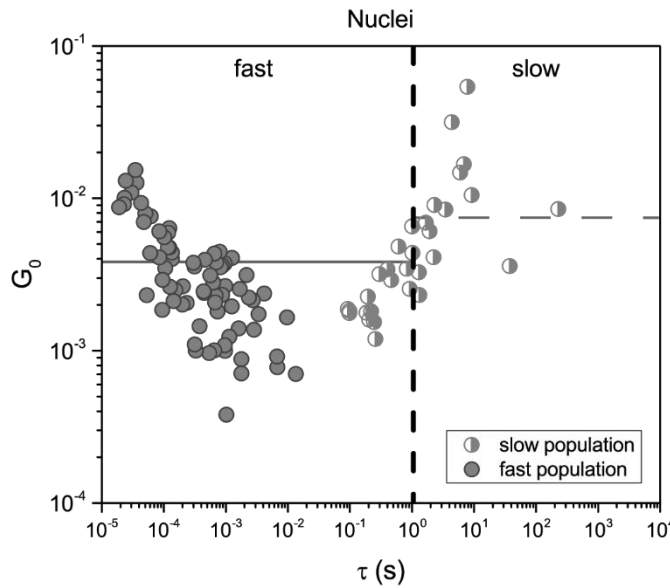

Figure 4.18 GP fluctuations of ACDAN fluorescence emission in the nuclei of HeLa cells. G0-vs-τ plot showing the results of the circular-RICS analysis performed on GP carpets of ACDAN emission collected in the nuclei of HeLa cells under physiological conditions. Black dashed line corresponds to the Mean – SD from fixed cells, as explained in Fig. 4.7. Image reprinted from ref.[84]

As a matter of fact, a similar organization has been theoretically postulated for the prokaryotic cytoplasm[101]. In this different scenario, characterized by the absence of internal membranes and scaffold structures, the hydrophobic effect would act as master regulator, dividing the cytoplasm into dynamically

crowded macromolecular regions and topologically complementary pools of solvent (i.e., water) with bulk-like properties[101]. To support this idea, Parry and co-workers, based on SPT measurements conducted on foreign particles of different sizes, debated that the bacterial cytoplasm displays properties typical of glass-forming liquids and that cellular metabolism contributes to fluidize the cytoplasm, allowing larger components to freely diffuse within the local environment and explore larger cellular regions[102].

Finally, an increasing set of data regarding subcellular organelles characterized by the lack of an enclosing membrane, but yet possessing coherent structures conferring peculiar molecular identities has been collected. Typical examples of such organelles include assemblies in the nucleus such as the nucleolus, Cajal bodies, nuclear speckles, and also cytoplasmic structures such as stress granules, P-bodies, and germ granules. Experiments performed in cuvette using selected purified components suggest that such membrane-less assemblies are formed through phase separation; this can be achieved either through nuclear polymerization of one (or more) component acting as a seed for solid/crystalline assemblies formation[103,104] or through liquid–liquid phase transition[105–107] that forms liquid droplets that eventually "age" into gels or glass. The common outcome of such processes is the creation of compartments either enriched in pools of active biomolecules, or depleted[108], thus playing an important role in the regulation of intracellular processes. Obviously, further investigations are needed with the purpose of unveiling possible mechanistic links between the physical properties of the intracellular environment and metabolism. To this end, Thoke and co-workers[78,79], building on a previous theoretical background[109], suggested that ATP may play a determining role; it acts indeed on metabolic processes by exerting an "inductive effect" upon binding to intracellular proteins. This, in turn, affects the modulation of their conformational state, their ion-binding properties, and the physicochemical properties of their

environment (e.g., the dynamic state of water in the protein proximity). The action of ATP can span over large spatial (*i.e.*, from organelles to the entire cell) and temporal (*i.e.*, from the microsecond to the second/min time scale of ATP production by glycolysis) scales as well as across the phylogenetic tree (from prokaryotes to eukaryotes), thus including all the observations collected so far.

4.5 Concluding remarks

In summary, in this Chapter we presented the combination of OT with circular-RICS analysis applied to the analysis of GP fluctuations of ACDAN. This approached allowed us to simultaneously achieve unmet 3D spatial and temporal resolution, thus unveiling, on the paradigmatic example of lysosomes, metabolism dependent solvent-polarity fluctuations within the lumen of a moving nanoscopic and subcellular organelle. In particular, OT yields high temporal resolution (micro-to-milliseconds) on a rapidly moving subcellular and nanoscopic reference system, while circular-RICS analysis of the GP carpets of ACDAN fluorescence allows the quantitative probing of the molecular processes occurring within individual structures during trafficking. Using the lysosome as a paradigmatic case study it was possible to observe that (i) the temporal intralysosomal GP fluctuations of ACDAN possess characteristic average dissipation times distributed in the micro-to-millisecond range; (ii) GP fluctuations, especially fast ones, are a characteristic of live cells; (iii) they are dependent on both the presence of metabolic energy, in the form of ATP, and the maintenance of acidic luminal pH; finally (iv) GP fluctuations are altered in amplitude and time dependence in a cellular model of lysosome-specific metabolic disorder.

Orbital tracking in combination with FCS is a powerful tool, suitable for the analysis of subcellular organelles in live cells. In comparison with time-

tunable FCS, the combination of OT and RICS allows for the study of subcellular organelles along all the spatial dimensions, paving the way for its establishment as a tremendous advantageous tool for the simultaneous 3D tracking of both the subcellular organelle and its content. Adopting this last approach, we were also able to unveil for the first time the polarity fluctuations of the solvent contained in the lumen of lysosomes and in different physiological conditions, thus proving the immense potential of this technique.

Chapter

5

Future perspectives

The idea of bringing the most advanced imaging tools at our disposal into the reference system of moving, nanoscopic structures of interest within living cells represents a truly paradigmatic shift in the way we investigate biological processes in general. In fact, rather than merely ‘observe’ living matter in action from a static viewpoint, here we ‘participate’ in the process. The toolbox proposed represents a flexible, nanotechnology-based, multi-functional approach capable of addressing virtually any high-impact biological question that involves single molecules operating on dynamic nanostructures.

In conclusion, this Thesis presents two different and innovative approaches that, through the paradigmatic example of the lysosome, proved their suitability for a number of different studies on the dynamics of subcellular organelles and their content in living cells. Worthy of note is the chance to

combine these approaches to existing techniques that potentially improve the resolution and type of information acquired. OT and RICS could, for instance, be performed on a STED microscope to further improve the spatial resolution of the outcome. Combination of OT and FLIM analysis could instead return information on the chemical composition and lifetime of the fluorophores involved. In particular, STED microscopy is the only super-resolution techniques that can be implemented in an orbital tracking setup. As a matter of fact STED needs a raster scanning microscope that can handle two laser beams in parallel: the first to create the so-called depletion region and the second to obtain spontaneous fluorescence effect within the super-resolved area of interest. Althoug the choice of STED-compatible fluorescent probes limits its application especially if used in combination with Orbital tracking, due to a possible high bleaching effect, there have been efforts in this sense to overcome its limitation. Remarkable is the research work published by Bianchini et al.[110]: they were able to implement a two-photon excitation-stimulated emission depletion optical microscope. A similar configuration offers the unique possibility to perform STED imaging with a single laser source , improving resolution but, most importantly, exploiting the intrinsic advantages of nonlinear excitation. All these improvements may potentially lead to fundamental discoveries especially if combined with Orbital Tracking and FCS tools such as RICS. In principle, this combination of powerful techniques could offer the ideal tool required for the study of the dynamics of biomolecules of interest contained within the subcellular compartments of interest paving the way for outbreaking discoveries.

Based on these considerations we might speculate that the huge amount of information still hidden behind several dynamic subcellular structures within live cells can be now addressed quantitatively. Among the most relevant examples are cytoplasmic organelles, chromatin structures, entire sub-cellular compartments (e.g. dendritic spines), naturally occurring pathogens (e.g. viruses or bacteria) and even man-engineered nano-vectors (e.g. for

nanomedicine applications). For each of these targets, the toolbox proposed can become the key to discriminate single-molecule behaviour from the natural movement of the reference system, thus making sophisticated physiopathology studies feasible in the natural condition of living matter at the nanoscale.

A few examples from neighbor research fields:

- *Cellular Biology - Physiology, Pathophysiology*: A huge amount of information is still hidden behind several dynamic nanostructures within live cells. Key examples encompass membrane-enclosed cytoplasmic organelles (e.g. mitochondria, lysosomes), membrane-less subcellular structures, etc.

- *Neuroscience*: the proposed approaches have the potential to bring the millisecond time resolution in the reference system of entire (micrometric or sub-micrometric) cellular protrusions, such as dendritic spines, or around axons to study neural transmission with single-molecule sensitivity.

- *Immunity and Infection*: The light envelope can represent a privileged observation point to reconstruct the complete transport history of naturally occurring pathogens (e.g. viruses or bacteria) during the process of host infection with unprecedented spatiotemporal resolution.

- *Nanomedicine*: It can be envisioned that the light envelope may be formed around the nanoengineered vectors that are routinely used in diagnostic and/or therapeutic applications both *in vitro* and *in vivo*. This in turn will provide the unique possibility to uncover the molecular details of vector interaction, trafficking and fate within living matter. Results of such investigations should open a new frontier for nanomedicine, as they will guide a rational engineering of optimized and better-tailored vectors. Of particular interest is the

fact that several polymeric and metallic nanoparticles commonly used for theranostic applications can be easily exploited for 3D orbital tracking applications, as they typically show robust light scattering properties. As a paradigmatic example, in Appendix C, a nanostructure carrying an active protein (in this case AcGFP) is delivered to the lysosomes in HeLa cells and the denaturation of the protein is monitored using standard confocal microscopy. Using feedback-based 3D orbital tracking and RICS with a more photobleaching-resistant fluorescent protein it would make possible the discovery of the exact moments in which the delivery system starts failing and this could help its improvement.

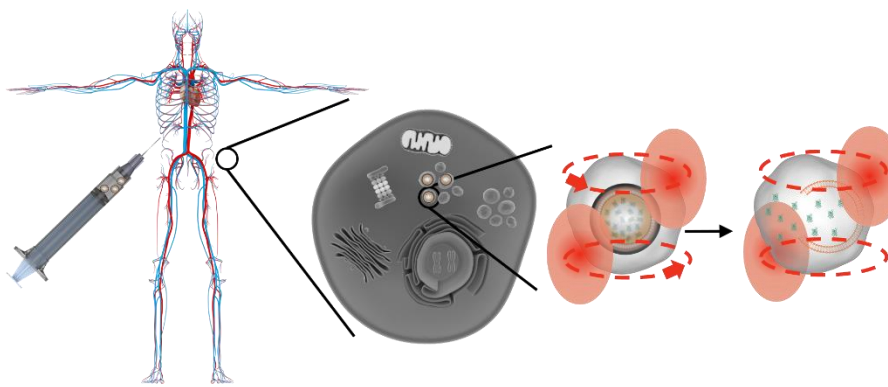

Figure 5.1 Futuristic theranostic applications based on Orbital tracking and FCS. The development of the technique presented in this Thesis may bring in the future to the design and implementation of special instrumentations where physicians and researchers may be able to track a drug system with an unprecedented spatial and temporal resolutions that unveils the most hidden dynamic properties of the molecules involved.

- *Physical and Analytical Chemical Sciences*: the idea of using feedback-based tracking locked onto a moving reference system is highly promising for the study of the physical chemistry and thermodynamics of biological systems. Notably the possibility to reach the unconventional resolution of approximately 1μs along the orbit opens unprecedented possibilities to study subtle molecular

details, such as protein conformational changes, receptor-ligand binding, etc.

Appendices

Appendix

A

Experimental setup for feedback-based orbital tracking and RICS

In this appendix, the detailed experimental setups adopted to perform all the experiments reported in this Thesis are reported.

A.1 Confocal microscopy imaging

For each experimental condition, images were acquired using an Olympus FluoView 1000-ASW-2.0 confocal microscope. To perform RICS analysis, for each case, temporal stacks of images were acquired at different pixel acquisition times (*i.e.*, pixel dwell time): 2, 4, 8, 20, 40, 100 and 200 μs. As the pixel dwell time increased, the number of frames collected for that pixel time decreased in order to obtain the same acquisition time duration for every condition and avoid bleaching. The scheme adopted was the following: 2 μs (200 frames acquired), 4 μs (150 frames), 8 μs (100 frames), 20 μs (80

frames), 40 µs (40 frames), 100 µs (20 frames) and 200 µs (10 frames). For RICS studies, a pixel size of 33 nm with 128 x 128 resolution was adopted. For each experimental scenario and each pixel dwell time, acquisitions from 20 different points of view were taken.

Lysotracker, Quantum Dots (QD) 545 and Rhodamine-DOPE excitation was achieved using the 515 nm line of the Argon laser, while CD63-GFP , AcGFP proteins and Alexa 488 were excited with the 488 nm line. Fluorophore emission was collected by a 60X planApo water immersion objective (numerical aperture=1.2). In detail, Lysotracker and Rhodamine-DOPE emission was collected in the 550-650 nm range, while CD63-GFP, AcGFP and Alexa488 emission was acquired in the 500-600 nm range; 530-550 nm was the collection range of the signal originated from QDs 545.

A.2 Live-cell confocal microscopy imaging and co-localization

Live-cell imaging for co-localization assays were carried out on a Zeiss LSM 880 raster scan confocal microscope equipped with three detectors (two GaAsP and one Airyscan) using a 63× NA 1.40 oil immersion objective. ACDAN was excited with laser light at 405 nm, while its emission was collected in the 410−480 nm range. CD63-EGFP was excited at 488 nm and collected in the 490−550 nm range. Lysotracker was excited at 561 nm and collected in the 570−650 nm range. For the three-channel experiment described in Fig. 4.5, the signals from ACDAN, EGFP, and Lysostracker where acquired in “sequential mode” operating on lines, that is, the system records the three signals sequentially switching-on only one laser per channel (with the other two switched off), and it repeats the operation for each image line. This imaging mode reduces cross-talk between channels to a minimum, while maintaining high temporal resolution (the three channels are acquired in approximately 0.5 s). Co-localization of the signals was assessed by calculating the Manders’ coefficients. Coefficient values range from 0 to 1, with ‘1’ indicating the maximum colocalization of the two signals[111].

A.3 Orbital tracking setup and experiments

In this section a brief description of the experimental setup of OT system is provided. It is similar to what described in Chapters 3 and 4 where a detailed description of the working principle is reported.

In this particular set of experiments, lysosomes containing QDs 545 were individually tracked using the ISS Orbital Tracking System, analogous to that previously described in Ref[75] and embedded in an Olympus FluoView 1000-ASW-2.0 confocal laser microscope. QDs 545 fluorescent emission was collected on 256 pixels around a 150 nm-radius orbit with a period of 1024 ms (meaning a pixel dwell time of 4 μs derived from: 1024 ms/256 px = 4 μs) and the orbit position was updated every 4-orbit period (defined as a 'cycle', approximately 4 ms).

As described in more details in Chapters 3 and 4, ISS Orbital Tracking System is able to record every single correction of the tracking orbit (and thus every single movement of the object) and reconstruct its trajectory from which many other important parameters can be recovered, such as, the Mean Square Displacement (MSD) or the average apparent diffusion coefficient D.

In addition, depending on the type of analysis performed, the following collection setups were used. For experiments on the diffusivity of ACDAN, the simultaneous excitation of ACDAN and Lysotracker was achieved by two-photon Ti:sapphire laser (Chameleon Vision, Coherent) tuned at 780 nm. Fluorophore emission was collected by using a 60× planApo water immersion objective (NA=1.2). ACDAN emission was measured in the 430−530 nm range (CH1), while Lysotracker signal was collected in the 570 650 nm range (CH2). For experiments on the GP of ACDAN, Ti:sapphire laser (Chameleon Vision, Coherent) tuned at 780 nm was used to excite both ACDAN and Lysotracker. In this case, three channels were activated, the first two to split

ACDAN signal for GP reconstruction (400−470 nm, CH1, and 475−545 nm, CH2, respectively), the last to collect Lysotracker emission (570−650 nm, CH3). Please note that this latter setup was used also for GP imaging at the whole cell level (i.e., to get GP spatial maps, see Fig. 4.4) with the microscope system operating in standard raster-scan mode. For experiments on the diffusivity of QDs "545" within lysosomes, the simultaneous excitation of QDs and Lysotracker was obtained by using a 515 nm argon laser line. Fluorophore emission was collected by using a 60× planApo water immersion objective (NA = 1.2). QDs emission was collected in the 530−550 nm range (CH1), while Lysotracker signal was collected in the 570−650 nm range (CH2). Worthy of mentioning, in all the experiments described in this work, Lysotracker signal was used to identify the target organelle for the tracking experiment. Both in the cases of two-photon excitation at 780 nm and one-photon excitation at 515 nm, Lysotracker signal vanished after few milliseconds of laser irradiation (i.e., few orbits) due to extensive photobleaching. By contrast, ACDAN signal proved to be stable under the same experimental conditions. By the way, the very first orbits from ACDAN intensity carpet(s) were not considered for fluctuation analysis (see below).

A.4 Software used for FCS analysis

All the FCS analyses reported in this Thesis, including RICS and STICS, were conducted using simFCS software (www.lfd.uci.edu, University of California Irvine) that contained all the required functionalities and fitting tools described elsewhere[63].

A.5 FCS analysis of ACDAN GP

Data acquired with the Orbital Tracking System were analyzed in two different ways: (i) circular-RICS analysis on intensity carpets and (ii) circular-RICS analysis on GP carpets. To perform circular-RICS analysis on the GP

carpet, the independent traces originated from the split collection of the emission of ACDAN fluorescence (CH1 and CH2) were processed using GP equation (Eq. 6). If applied pixel-by-pixel, Eq. 6 generates a GP "carpet". GP carpets are then analyzed using the same circular-RICS tool mentioned above. Thus, D and G0 values were obtained by fitting the correlation curves. The D value, in this specific case, was linked to the characteristic average duration (τ) of the GP fluctuations contained in the carpet by using the relation represented in Eq. 3.

A.6 Acquisition of ACDAN Fluorescence Spectrum and Evaluation of GP

ACDAN was dissolved in different solvents at a concentration of 2.5 μM. Each solvent is characterized by a different dielectric constant as shown in Table A.1. The fluorescence emission spectrum of each solution was collected using a Varian Cary Eclipse Fluorescence Spectrophotometer in the 400−545 nm range.

To evaluate the characteristic GP value of each solution, ACDAN spectrum was split into two regions, similarly to what performed at the microscope. The first (CH1) was computed by integrating the spectrum intensities in the

Solvent	Diox	CHCl3	AcOET	THF	CH2Cl2	3-Methyl1-Butanol	IPrOH	Acetone	MeOH	DMF	ACN	DMSO	H2O
Dielectric constant	0.28	4.8	6	7.52	9.1	15.2	18.3	20.7	32.6	36.7	37.5	46.7	80.1

Table A.1 Solvent used for ACDAN GP study. The Table shows the name of the solvents employed (above) and the corresponding relative dielectric constant (below). Table reprinted from ref.156[84]

400−470 nm range, while the second (CH2) by integrating the emission in the 475−545 nm range. GP values were then obtained by using Eq. 6.

A.7 Calibration of the hydrodynamic radius of QDs

For calibration of hydrodynamic radius of QDs, we suspended 5 μL of QD stock solution in 50 μL of 50 mM borate buffer. The suspension was then poured in a 22 mm glass bottom dish for cell culture and analyzed under the Orbital tracking system. The fluorescence signal was collected and analyzed as described above for ACDAN. Through Eq. 3, the average hydrodynamic radius was evaluated and averaged with the value obtained from vesicles with QDs. The result was then used to compute the viscosity of lysosomes when analyzed with QDs.

A.8 Statistical Analysis

Diffusion coefficients (and viscosities, derived byEq. 1) are normally distributed in each experiment. Thus, their values are reported throughout the text as mean ± SD and compared among different experiments using the Student's t test. By contrast, GP fluctuation values are not normally distributed. Their values are reported in the text using the minimum-maximum range. In this case, distributions from different experiments were compared using the Mann−Whitney test. Each analysis was conducted using OriginPro 9. Differences were considered significant for $P < 0.05$.

Appendix

B

Sample preparation

In this appendix, the detailed descriptions of the techniques used to prepare experimental samples to perform all the experiments reported this Thesis are reported.

B.1 Cell culture and treatments

Experiments on cells were conducted using different cell lines and treatments. HeLa cells (CCL-2 ATCC) were seeded on 22-mm glass bottom dishes (Willco Wells) and let adhere on top of them at 37 °C and 5% CO_2 in a cell culture incubator overnight. Dulbecco's Modified Eagle Medium (DMEM) without phenol red (Gibco), supplemented with 10% Fetal Bovine Serum (FBS, Gibco), 100 U/mL of penicillin, and 100 μg/mL of streptomycin was used as growth medium.

For time-lapse acquisitions and diffusion coefficient analysis, HeLa cells were labelled using two different solutions: Lysotracker and CD63-protein transfection. LysoTracker Red DND-99 (Invitrogen) was added to the desired

final concentration of 60 nM in the growth medium 20 minutes before the beginning of data acquisitions.

CD63-pEGFP C2 plasmid (gift from Paul Luzio, Addgene plasmid # 62964) was transfected into cells by electroporation using Neon Transfection System 10 μL Kit (Invitrogen). In particular, cells were trypsinized, pelleted, and resuspended in Resuspension Buffer R. DNA (0.1 μg/μL) was added to 5×10^5 cells in 10 μL buffer, followed by electroporation using Neon Transfection System (Invitrogen) operating at a voltage of 1005 V and width of 35 ms. After these steps, cells were seeded and cultured in DMEM containing 10% FBS and supplements without antibiotics and analyzed 24 h later.

Lysotracker and QDs were administered to HeLa cells following 3 washing steps with PBS. For each 22-mm glass bottom dish 5μl of QD stock solution (Qdot 545 ITK Amino (PEG), Thermofischer) were suspended in $1\,ml$ of growth medium without serum, and then, were poured on the glass-bottom dish containing cells following a sonication step of 5 minutes. After 3 hours of incubation, cells were washed 3 times with PBS containing Mg^{2+} and Ca^{2+} (in order to avoid cell detachment) and then incubated again with FBS-containing medium. After 24 hours, cells were again washed three times with PBS containing Mg^{2+} and Ca^{2+} and then incubated with medium containing FBS and Red Lysotracker at a concentration of 60 nM, as described above. 20 minutes later, cells were ready for microscope analysis.

Regarding preparation of fibroblasts for experiments on Twitcher model, cells were prepared as described in section 4.1.

B.2 Liposomes containing QDs 545: partially immobilized in Agarose gel

DPPC, 1,2-dipalmitoyl-sn-glycero-3-phosphocholine lipid (10 mg/mL in chloroform) and DOPE-Rhodamine lipid were purchased from Avanti Polar Lipids (Alabaster, AL, USA). Low-gelling-temperature agarose, BioReagent was purchased from Sigma Aldrich (St. Louis, MO, USA). Liposomes of

DPPC were prepared using the standard method[112]. Liposomes containing QDs were obtained through the evaporation of 100 µL of chloroform solution containing 1 mg of DPPC in a centrifugal evaporator under vacuum for 2 h a thin film of lipid was obtained. The film was then hydrated by adding 245 µL PBS at pH 7.45 and 5 µL of the stock solution of QDs at 50°C. The final DPPC concentration was 5 mM. Liposomes were frozen in liquid nitrogen and then thawed in a water bath at 50°C. This freeze-thaw cycle was repeated five times[113]. DOPE-Rhodamine liposomes were instead obtained by evaporating of 100 µL of chloroform solution containing DPPC and DOPE-Rhodamine in a ratio of 1:50 respectively. Evaporation lasted for 2 h under vacuum and the resulting thin film of lipids and successively Rhodamine-labelled liposeoms were then hydrated as described above. Both types of liposomes were then partially immobilized using Agarose gel as described in Ref[114]. Agarose was dissolved in PBS at a concentration of 1% w/v. Liposomes were added to the gel while the agarose was in the fluid state. After mixing, the solution was placed on a glass bottom petri dish and was left at room temperature for jellification. Following jellification, liposomes containing QDs and liposomes labelled with Rhodamine on their surfaces were analyzed using confocal microscopy. Fluorescence signal was collected and analyzed as described above (see B.2).

B.3 Preparation of fluorophore solutions

Different fluorophore solutions were prepared and analyzed using RICS analysis as controls for the various experiments conducted. A 500 nM of recombinant AcGFP (*Aequorea coerulescens* GFP) solution was prepared by dissolving the proper amount of protein in a 20 mM DEA buffer. AcGFP plasmid was purchased from Clonetech (Mountain View, CA, USA) and the protein was expressed in (DE3) E. coli cells following standard procedures for cloning techniques.

Appendix

C

Protein encapsulation and delivery through silica-based nanoparticles

This appendix reports the design and realization of a silica-based nanosystem devised for the delivery of active proteins. The work shown here was published after peer--review on the Journal of Nanomaterials (ref. [115]). I decided to report a work on such a different topic because it may represent a good example of possible applications of the techniques described in Chapter 2 and 3. Once properly adapted for orbital tracking or persistent confocal microscopy, drug delivery nanosystems could easily be studied with either the combination of OT and RICS, or the time-tunable FCS approach. This, in turn, will reveal the dynamics behaviour of such systems at an unprecedented spatiotemporal scale. In addition, the results obtained here could represent an optimal starting point for the development of a strategy for the delivery of

active proteins, an application that is gaining more and more attention nowadays.

C.1 A brief introduction to protein delivery

Therapeutic strategies based on protein are attracting more and more interest nowadays and are being actively researched for the treatment of a variety of diseases[116–118]. The high function specificity of proteins makes their administration the most suitable choice for the treatment of particular diseases characterized, for instance, by the loss of specific enzymatic functions: in this regard, lysosomal storage disorders (LSDs) may represent the best example[119]. As a matter of fact, protein-based therapeutics offers a unique list of advantages[118,120]. Proteins are typically characterized by specific sets of roles that cannot be easily mimicked by other chemical species. The high functional specificity typical of proteins and, in particular of enzymes, offers, in principle, the unique opportunity to design treatments that lower the interference with other off-target biological processes, reducing, as a secondary result, adverse and aspecific effects. In light of these benefits, one may expected reduced times for clinical approval of protein-based therapeutic compounds as compared to small-molecule drugs[118]. Despite the presence of these great advantages, successful protein delivery remains a challenging task. A major issue is represented by the existence of obstacles that place themselves against the delivery systems on their way to their final target. The loss of protein chemical and physical stability is usually a common requirement; for systemic treatments, proteins are often administered parenterally to avoid the acidic gastro-intestinal tract. In addition, due to the relatively high molecular mass and surface polarity, protein targeted and efficient delivery is inevitably hindered by the presence of biological barriers (e.g. the Blood Brain Barrier, the endothelium of blood vessels or the cellular plasma membrane [121,122]). To overcome these biological and physical limits, a number of solutions have been proposed and realized even if with limited

success[120]. Chemical modification of proteins, for instance, although favoring protein circulation half-life, proved to be extremely complex, often ending up in unwanted protein conformational changes (that in turn impair the desired functions[123]). Another interesting strategy is represented by genetic engineering: its application in protein delivery brought to the creation of Fc-based fusion proteins (made up by linking an immunoglobulin Fc domain to the therapeutic protein) that greatly enhanced protein half-life and their therapeutic efficacy. Still, these strategies are often accompanied by an adverse immune response[124]. However, in this context, a promising role is played by nanoparticle-based systems, thanks to a variety of intrinsic advantageous properties they offer. As a matter of fact, nanoparticles are, in general, small enough (< 200 nm) to avoid accumulation in spleen and lungs, but large enough (> 10 nm) to escape renal clearance[125]. Through surface engineering, they can easily be functionalized with multiple and different materials/molecules specific for different purposes: nanoparticles can indeed acquire biomimetic surfaces[126,127] (stealth systems) and host pH-responsive moieties[128] or targeting tools, such as antibodies, peptides or small molecules[129]. To efficiently load protein cargoes, however, nanoparticle-based strategies must fulfill some additional requirements. Nanoparticles are typically created using solvents and reagents that can easily affect protein structure and function[130]. Thus far, multiple and different architectures and materials were tested to tackle these limitations. PLGA-based nanoparticles probably represent the best example in terms of both gentle preparation and loading efficiency [120,131,132]. Still, it was shown that PLGA hydrolysis (a fundamental step in PLGA- based nanoparticle biodegradation) produces an acidic internal environment that can potentially perturb protein active conformations[133]. Among inorganic nanoparticles instead, mesoporous silica-based nanoparticles recently emerged as a promising platform in *theranostic* applications in general[134–140]. Silica-based nanomaterials present an inert, non-

immunogenic, easy-to-modify and biodegradable surface[120,141–143]. Regarding their application in protein delivery, several solutions were proposed to combine the benefits of the material with the specific needs of a protein-based delivery strategy. Among others, Bégu and co-workers[144] recently created a system consisting of lipid-based vesicles. Following their loading with both hydrophilic and lipophilic small molecular drugs, these vesicles were then covered with a thin silica shell that contributed to increase the particle stability and allow for surface functionalization. Starting from this strategy, I adapted the protocol to the need of encapsulating a protein. In details, the realization of a liposome containing an active protein (in this case *Aequorea coerulescens* Green Fluorescent Protein, AcGFP) coated with a thin shell of silica that offers a prolonged resistance to acidic, harsh environments is herein proposed. Another important advantage obtained with this silica coat is represented by the presence of a biodegradable and protecting shell that allows the particle (and thus the payload) to reach its target and deliver an active protein or enzyme; in addition, the liposome, thanks to its gentle preparation process, will allow the load of the desired protein in its lumen while providing protection during the synThesis of the coat of silica. In the following, I describe the steps designed for the production and loading of the nanoparticles along with the results obtained from confocal imaging analysis of their trafficking and final fate when administered to living HeLa cells.

C.2 SynThesis and characterization of the nanoparticles

The synThesis of the proposed nanoparticles can be divided into two major steps: liposome preparation and silica thin shell formation. First liposomes are formed and loaded with AcGFP dissolved in a Diethanolamine (DEA) buffer solution (for more details please refer to the section ‘Material and methods’ of the paper published on the journal Nanomaterials[115] that originated from

the work subject of this Appendix). In details, a thin film of DPPC (1,2-dipalmitoyl-sn-glycero-3-phosphocholine) lipid is formed following a previously described procedure[145]. The lipid film is then hydrated in DEA buffer (20 mM) solution containing AcGFP (2 μM) through vigorous vortexing and sonication at 40 °C. Once formed and loaded, liposomes are extruded using a 100nm pore-size membrane and then centrifuged to remove the supernatant containing the unloaded AcGFP. Newly formed AcGFP-loaded liposomes are then suspended in fresh DEA buffer solution, and added, for silica shell coating, to an aged tetraethyl orthosilicate (TEOS) solution prepared as in the following: TEOS is added to deionized water and the mix left under stirring for 24 h at RT. In the aged solution, TEOS is hydrolyzed to orthosilicic acid and, when its concentration exceeds the saturation limit, its polymerization occurs[146]. The process yields, in sequence, low- to high-molecular polymers and, due to their condensation, silica particles of 1–2 nm in diameter. To create the thin silica-shell, AcGFP-loaded liposomes are added to the aged solution before silica nuclei increase in size following a LaMer growth pattern, resulting in their absorption on the surface of liposomes by ionic interactions. Then, the remaining orthosilicic acid continues to form a complete shell until its saturation limit is reached or the reaction interrupted. Silica-protected AcGFP-loaded liposomes are finally isolated from the original solution using centrifugation. Notably, the entire process is performed in physiological pH water solutions (notice different buffers other than DEA can be employed, please refer to ref.[115]), in order to preserve the activity of the loaded proteins. Fig. C.1A briefly summarizes these concepts. TEM and SEM characterizations reported in Fig. C.1B and C show the obtained nanoparticles with an external thin layer (~2-3 nm) of silica and average diameters of 137±40 nm (reported as mean ± standard deviation)). CryoEM allowed, instead, to recognize the lipid bilayer just

underneath the silica coat (Fig. C.1D) thus further supporting the final architecture of the nanosystem.

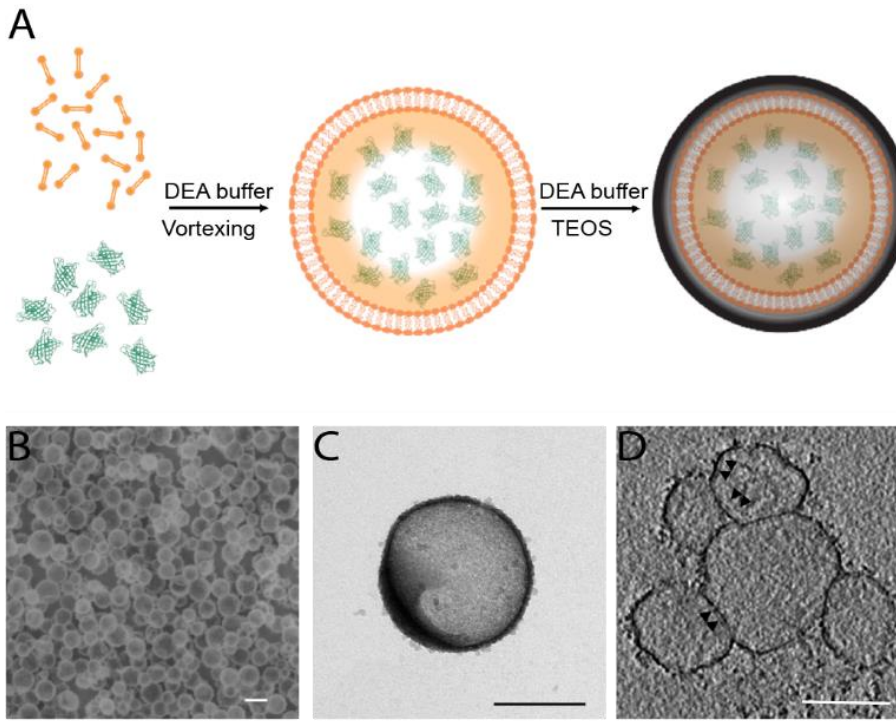

Figure C.1 Synthesis and characterization of AcGFP-loaded silica nanoparticles. (A) Schematic representation of nanoparticle synThesis. (B) SEM characterization of the obtained nanoparticles, scale bar 200 nm. (C) TEM image of a single AcGFP-loaded nanoparticle, scale bar 200 nm. (D) Averaged tomographic slice of several AcGFP-loaded nanoparticles. Black arrows point to the lipid layer present underneath the silica layer (darker contour) that delimit the nanoparticles scale bar 100 nm.

Dynamic Light Scattering (DLS) characterization revealed an average hydrodynamic diameter (HD) size of about 390 nm with a low polydispersity

index (PI=0.2) and a zeta-potential of -17.2 mV. Worthy of note is the fact that HD values are typically bigger with respect to the diameter estimate extracted from TEM or SEM due to the fact that HD comprises both the actual diameter of the nanoparticles and the solvation layer. Notable, it must de said that, as stated before, the surface of silica-coated liposomes can be easily modified with the addition of (3-amminopropyl)triethoxysilane (APTES) to change the surface electrostatic charge of nanoparticles and add anchor points for the attachment of targeting molecules. With this nanoparticle architecture, APTES functionalization is achieved adding 5 µl of APTES in a 1.5 ml of water containing AcGFP-loaded liposomes, the solution is then left under gentle stirring for 15 minutes at 37 °C; this result was confirmed by a positive zeta-potential value measured (15.1 mV).

Encapsulation efficiency was assessed using a calibration curve based on the fluorescence intensity recorded at different protein concentrations (exploiting AcGFP intrinsic fluorescence). In particular, results obtained with nanoparticle samples (see section C.5 section below) were compared with the calibration curve; this method revealed an encapsulation efficiency of about 10%. In this regard, it must be said that, although not high, the experimental conditions used during the whole encapsulation process are compatible with the recovery of non-encapsulated proteins (and their possible re-use, thus avoiding material waste).

C.3 Cellular uptake and final fate of nanoparticles

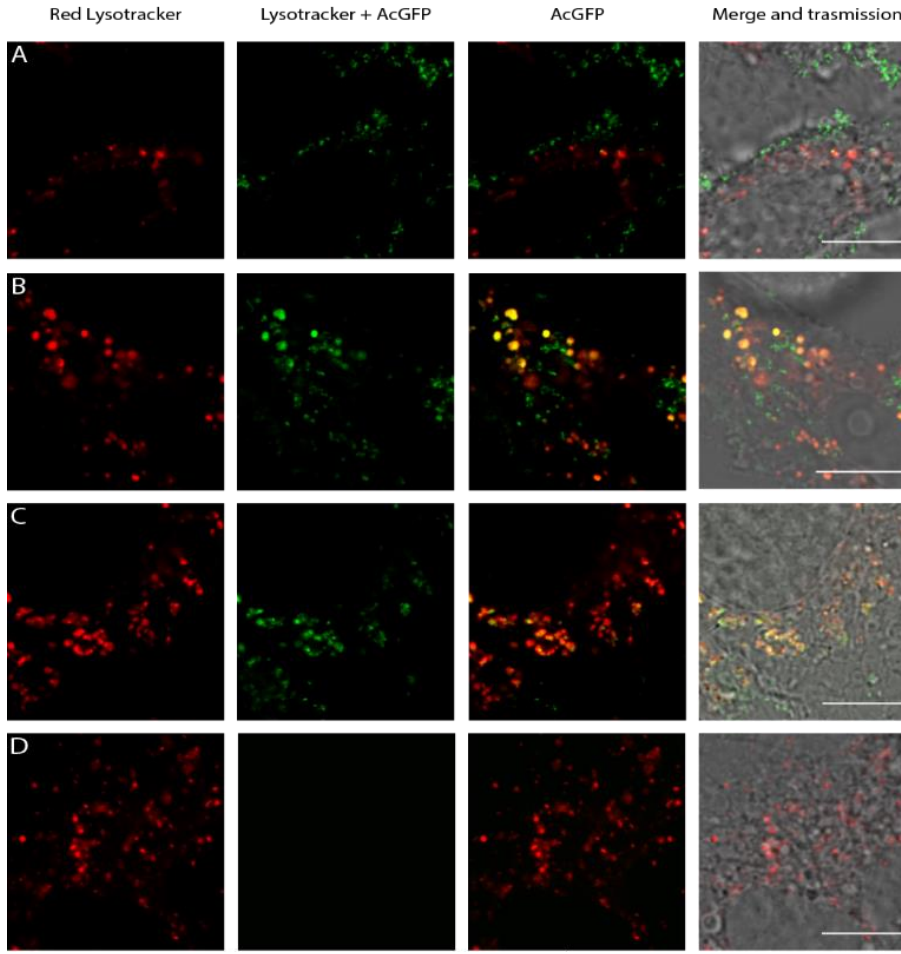

Figure C.2 Nanoparticle internalization within lysosomes of HeLa cells. (A-D) Confocal images for colocalization analysis. Columns on the left show Red Lysotracker channel, while middle columns report AcGFP-loaded nanoparticle channel and columns on the right originate from the merging of Lysotracker and protein channels. Rows represents the situation at different time points: 3 hours (A), 12 hours (B), 24 hours (C) and 72 hours (D) after particle administration. Notice how particles are all colocalizing with lysosomes at 24 hours and at 72 hours no sign from AcGFP was detected. Scale bar 10 µm.

As anticipated above, cell studies were conducted in HeLa cells (Fig. C.2). Fist, AcGFP-loaded nanoparticles suspended in the cell-culture medium without serum were incubated with HeLa cells for 3 hours. After incubation, cells were washed with PBS for three times and complete cell-culture medium containing the proper amount of Lysotracker was added following the standard protocol (see ref.[115]).

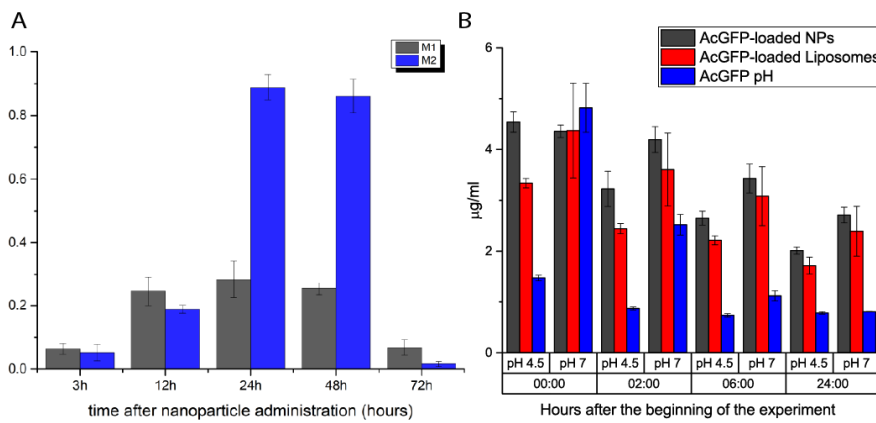

Figure C.3 Cell colocalization and fluorescent stability in acidic conditions. (A) Manders' colocalization coefficients; referring to M1 as the colocalization of AcGFP channel with Lysotracker channel and vice versa for M2. Colocalization rallies to a maximum at 12 and 24 hours after particle administration and steeply decreases at 72 hours. (B) Amount of active protein in both citric acid (pH4.5) and PBS (pH 7) solutions at different time points (namely, time 0, and 2, 6 and 24 hours since the beginning of the experiment. Black bars: AcGFP-loaded nanoparticles. Red bars: AcGFP-loaded DPPC liposomes. Blue bars: free AcGFP in solution. The initial quantity of protein equals for each single condition. Notice how black bars (*i.e.*, protein-loaded nanoparticles) maintain the higher levels especially for the later points.

Nanoparticle colocalization with Lysotracker was assessed using confocal microscopy at different time points (namely 3, 12, 24, 48 and 72 hours after

administration). Results showed a pick of colocalization of nanoparticles within lysosomes 24 hours after administration, while at 72 hours no fluorescence was detected from AcGFP. Manders' coefficients quantitatively show that colocalization starts to increase at 12 h, reaches a pick at 24 h and 48 h, and then suddenly decreases and disappears at 72 h (not shown). This dynamic behavior can be considered as the consequence of nanoparticle degradation inside lysosomes, followed by the further digestion of AcGFP protein. In addition, the tested nanosystems did not elicit cytotoxicity in hours (for further details the reader is redirected to ref.[115]).

C.4 Particle stability in acidic conditions

To assess nanoparticle and protein stability in an environment similar to the acidic conditions of lysosomes, I designed an experiment based on monitoring AcGFP fluorescence emission (and, as a consequence, protein stability) in different buffer conditions at 37°C. Nanoparticles were added in two different solutions: citric acid (pH 4.5) and PBS (pH 7). In addition, simple liposomes containing the same amount of protein as the tested nanoparticles and isolated AcGFP were used as controls, thus creating 6 different experimental conditions. Fluorescence intensity from the six different situations were collected for 24 hours at different time points (0, 2, 6 and 24 hours after the beginning of the experiment). The results obtained suggested that silica-based nanoparticles help protecting their payload for the longest time, while protein alone, especially at acidic pH, gets denatured in a short time. The comparison with simple liposomes revealed that silica-based nanoparticles maintained a higher intrinsic fluorescence intensity (thus a higher amount of active protein) for all time points, for both acidic and neutral conditions. I would like to call the reader's attention on how the amount of fluorescence signal from the nanoparticles at the zero-time point is equal for both acidic and neutral

conditions while for liposomes and proteins alone, the acidic conditions show lower signal values compared to the neutral cases. Taken together, these results seem to supports the idea that the silica shell may provide a protective shield against acidic solutions, thus safeguarding the stability and functionality of the protein loaded for longer times with respect to the conditions of the control experiments. This interpretation is further supported by the studies conducted in cells using AcGFP-loaded liposomes alone (for further details please address ref.[115]). In this case, liposomes lasted inside cells only for 6-8 hours and they never reached such a high internalization efficiency (despite a zeta-potential of 2mV) within lysosomes. Worthy of note is that cell cultures were washed only the first time following nanoparticle administration; in fact, cell cultures were washed only at the beginning of the internalization experiments; this is important because allowed us to avoid the removal of particles expelled by the cell, meaning that, if present we could have noticed them: this did not happen, thus further corroborating the idea that nanoparticles (and thus active protein) were degraded inside lysosomes.

C.5 Concluding remarks

The results reported above show how the combination of nanoparticle architecture and synThesis conditions proposed could represent a potential effective platform, not limited to small organic molecules, but open to protein encapsulation and delivery. New perspectives may be envisioned based on these preliminary results. Functionalization with effective targeting molecules is a further step to be addressed, along with the encapsulation of different proteins, tailored to specific biomedical applications. In regard to targeting, it is worth noting that the present nanosystem has already proved its ability to efficiently target the lysosomes with no need for additional modifications. The degradation of the silica shell inside lysosomes (with subsequent release of

intact protein cargoes) may represent an interesting opportunity for the treatment of LSDs: the delivery of active galactoceribrosidase (GALC) enzyme to lysosomes as an Enzyme Replacement Therapy (ERT) represents, for instance, the preferred choice of treatment for the rare Krabbe disease[147]. In general, the architecture and results herein reported represent only the beginning of an itinerary required for their validation as a potent tool for protein delivery and therapeutics. In addition, the further analysis of such a delivery system with the analytical techniques described in this dissertation may contribute to the acquisition of a deeper understanding on the degradation dynamics of this delivery system thus offering the opportunity for its redesign and improvement following a specific function.

Bibliography

1. Schrödinger, E. *What is life? The physical aspect of the living cell and mind*. (Cambridge University Press Cambridge, 1944).
2. Satori, C. P., Henderson, M. M., Krautkramer, E. A., Kostal, V., Distefano, M. M. & Arriaga, E. A. Bioanalysis of Eukaryotic Organelles. (2013).
3. Alberts, B., Bray, D., Hopkin, K., Johnson, A. D., Lewis, J., Raff, M., Roberts, K. & Walter, P. *Essential cell biology*. (Garland Science, 2015).
4. Theillet, F. X. *et al.* Physicochemical properties of cells and their effects on intrinsically disordered proteins (IDPs). *Chemical Reviews* (2014). doi:10.1021/cr400695p
5. Hyman, A. A. & Simons, K. Beyond oil and waterphase transitions in cells. *Science (80-.).* **337,** 1047–1049 (2012).
6. O'Farrell, P. Z., Goodman, H. M. & O'Farrell, P. H. High resolution two-dimensional electrophoresis of basic as well as acidic proteins. *Cell* **12,** 1133–1142 (1977).
7. Pasquali, C., Fialka, I. & Huber, L. A. Subcellular fractionation, electromigration analysis and mapping of organelles. *J. Chromatogr. B Biomed. Sci. Appl.* **722,** 89–102 (1999).
8. Satori, C. P., Kostal, V. & Arriaga, E. A. Review on recent advances in the analysis of isolated organelles. *Anal. Chim. Acta* **753,** 8–18 (2012).
9. Huber, L. A., Pfaller, K. & Vietor, I. Organelle proteomics: Implications for subcellular fractionation in proteomics. *Circ. Res.* **92,** 962–968 (2003).
10. Olson, K. J., Ahmadzadeh, H. & Arriaga, E. A. Within the cell:

Analytical techniques for subcellular analysis. *Anal. Bioanal. Chem.* **382,** 906–917 (2005).

11. Huber, L. A. Is proteomics heading in the wrong direction? *Nat. Rev. Mol. Cell Biol.* **4,** 74–80 (2003).

12. Gross, R. W. High plasmalogen and arachidonic acid content of canine myocardial sarcolemma: a fast atom bombardment mass spectroscopic and gas chromatography-mass spectroscopic characterization. *Biochemistry* **23,** 158–165 (1984).

13. Gross, R. W. Identification of plasmalogen as the major phospholipid constituent of cardiac sarcoplasmic reticulum. *Biochemistry* **24,** 1662–1668 (1985).

14. Koning, R. I., Koster, A. J. & Sharp, T. H. Advances in cryo-electron tomography for biology and medicine. *Ann. Anatomy-Anatomischer Anzeiger* **217,** 82–96 (2018).

15. Callaway, E. Molecular-imaging pioneers scoop Nobel. *Nature* (2017). doi:10.1038/nature.2017.22738

16. Knoll, M. & Ruska, E. Das elektronenmikroskop. *Zeitschrift für Phys.* **78,** 318–339 (1932).

17. Knott, G. & Genoud, C. Is EM dead? *J Cell Sci* **126,** 4545–4552 (2013).

18. Palade, G. E. The fine structure of mitochondria. *Anat. Rec.* **114,** 427–451 (1952).

19. Palade, G. E. & Porter, K. R. Studies on the endoplasmic reticulum: i. its identification in cells in situ. *J. Exp. Med.* **100,** 641–656 (1954).

20. Adrian, M., Dubochet, J., Lepault, J. & McDowall, A. W. Cryo-electron microscopy of viruses. *Nature* **308,** 32 (1984).

21. Weber, M. S., Wojtynek, M. & Medalia, O. Cellular and Structural Studies of Eukaryotic Cells by Cryo-Electron Tomography. *Cells* **8,** 57 (2019).

22. Baker, L. A., Grange, M. & Grünewald, K. Electron cryo-tomography captures macromolecular complexes in native environments. *Current Opinion in Structural Biology* (2017). doi:10.1016/j.sbi.2017.08.005

23. Bäuerlein, F. J. B., Saha, I., Mishra, A., Kalemanov, M., Mart\'\inez-

Sánchez, A., Klein, R., Dudanova, I., Hipp, M. S., Hartl, F. U., Baumeister, W. & others. In situ architecture and cellular interactions of PolyQ inclusions. *Cell* **171,** 179–187 (2017).

24. Wan, W., Kolesnikova, L., Clarke, M., Koehler, A., Noda, T., Becker, S. & Briggs, J. A. G. Structure and assembly of the Ebola virus nucleocapsid. *Nature* **551,** 394 (2017).

25. Braga, P. C., Ricci, D. & others. *Atomic force microscopy in biomedical research: methods and protocols*. (Springer, 2011).

26. Lee, G.-J., Chae, S.-J., Jeong, J. H., Lee, S.-R., Ha, S.-J., Pak, Y. K., Kim, W. & Park, H.-K. Characterization of mitochondria isolated from normal and ischemic hearts in rats utilizing atomic force microscopy. *Micron* **42,** 299–304 (2011).

27. Awizio, A.-K., Onofri, F., Benfenati, F. & Bonaccurso, E. Influence of synapsin I on synaptic vesicles: an analysis by force-volume mode of the atomic force microscope and dynamic light scattering. *Biophys. J.* **93,** 1051–1060 (2007).

28. Guo, S., Hong, L., Akhremitchev, B. B. & Simon, J. D. Surface elastic properties of human retinal pigment epithelium melanosomes. *Photochem. Photobiol.* **84,** 671–678 (2008).

29. Petibois, C. Imaging methods for elemental, chemical, molecular, and morphological analyses of single cells. *Anal. Bioanal. Chem.* **397,** 2051–2065 (2010).

30. Kuimova, M. K., Chan, K. L. A. & Kazarian, S. G. Chemical imaging of live cancer cells in the natural aqueous environment. *Appl. Spectrosc.* **63,** 164–171 (2009).

31. Weiss, P. S. Nobel prizes for super-resolution imaging. (2014).

32. Van Noorden, R. Insider view of cells scoops Nobel. *Nature* **514,** 286 (2014).

33. Huang, B., Bates, M. & Zhuang, X. Super-resolution fluorescence microscopy. *Annu. Rev. Biochem.* **78,** 993–1016 (2009).

34. Rust, M. J., Bates, M. & Zhuang, X. Sub-diffraction-limit imaging by stochastic optical reconstruction microscopy (STORM). *Nat. Methods*

3, 793 (2006).

35. Betzig, E., Patterson, G. H., Sougrat, R., Lindwasser, O. W., Olenych, S., Bonifacino, J. S., Davidson, M. W., Lippincott-Schwartz, J. & Hess, H. F. Imaging intracellular fluorescent proteins at nanometer resolution. *Science (80-.).* **313,** 1642–1645 (2006).

36. Hess, S. T., Girirajan, T. P. K. & Mason, M. D. Ultra-high resolution imaging by fluorescence photoactivation localization microscopy. *Biophys. J.* **91,** 4258–4272 (2006).

37. Cox, S. Super-resolution imaging in live cells. *Dev. Biol.* **401,** 175–181 (2015).

38. Cox, S. & Jones, G. E. Imaging cells at the nanoscale. *Int. J. Biochem. Cell Biol.* **45,** 1669–1678 (2013).

39. Balzarotti, F., Eilers, Y., Gwosch, K. C., Gynnå, A. H., Westphal, V., Stefani, F. D., Elf, J. & Hell, S. W. Nanometer resolution imaging and tracking of fluorescent molecules with minimal photon fluxes. *Science (80-.).* (2017). doi:10.1126/science.aak9913

40. Gustafsson, M. G. L. Surpassing the lateral resolution limit by a factor of two using structured illumination microscopy. *J. Microsc.* **198,** 82–87 (2000).

41. Gustafsson, M. G. L., Shao, L., Carlton, P. M., Wang, C. J. R., Golubovskaya, I. N., Cande, W. Z., Agard, D. A. & Sedat, J. W. Three-dimensional resolution doubling in wide-field fluorescence microscopy by structured illumination. *Biophys. J.* **94,** 4957–4970 (2008).

42. Heintzmann, R. Saturated patterned excitation microscopy with two-dimensional excitation patterns. *Micron* **34,** 283–291 (2003).

43. Kner, P., Chhun, B. B., Griffis, E. R., Winoto, L. & Gustafsson, M. G. L. Super-resolution video microscopy of live cells by structured illumination. *Nat. Methods* **6,** 339 (2009).

44. Hirvonen, L. M., Wicker, K., Mandula, O. & Heintzmann, R. Structured illumination microscopy of a living cell. *Eur. Biophys. J.* **38,** 807–812 (2009).

45. Fiolka, R., Shao, L., Rego, E. H., Davidson, M. W. & Gustafsson, M. G. L. Time-lapse two-color 3D imaging of live cells with doubled

resolution using structured illumination. *Proc. Natl. Acad. Sci.* (2012). doi:10.1073/pnas.1119262109

46. Hell, S. W. & Wichmann, J. Breaking the diffraction resolution limit by stimulated emission: stimulated-emission-depletion fluorescence microscopy. *Opt. Lett.* **19,** 780–782 (1994).

47. Klar, T. A. & Hell, S. W. Subdiffraction resolution in far-field fluorescence microscopy. *Opt. Lett.* **24,** 954–956 (1999).

48. Nagerl, U. V., Willig, K. I., Hein, B., Hell, S. W. & Bonhoeffer, T. Live-cell imaging of dendritic spines by STED microscopy. *Proc. Natl. Acad. Sci.* (2008). doi:10.1073/pnas.0810028105

49. Schneider, J., Zahn, J., Maglione, M., Sigrist, S. J., Marquard, J., Chojnacki, J., Kräusslich, H. G., Sahl, S. J., Engelhardt, J. & Hell, S. W. Ultrafast, temporally stochastic STED nanoscopy of millisecond dynamics. *Nat. Methods* (2015). doi:10.1038/nmeth.3481

50. Lanzanò, L., Scipioni, L., Di Bona, M., Bianchini, P., Bizzarri, R., Cardarelli, F., Diaspro, A. & Vicidomini, G. Measurement of nanoscale three-dimensional diffusion in the interior of living cells by STED-FCS. *Nat. Commun.* **8,** 1–10 (2017).

51. Elson, E. L. Fluorescence correlation spectroscopy: past, present, future. *Biophys. J.* **101,** 2855–2870 (2011).

52. Haustein, E. & Schwille, P. Fluorescence correlation spectroscopy: novel variations of an established technique. *Annu. Rev. Biophys. Biomol. Struct.* **36,** 151–169 (2007).

53. Ries, J. Advanced fluorescence correlation techniques to study membrane dynamics. (2008).

54. Krichevsky, O. & Bonnet, G. Fluorescence correlation spectroscopy: the technique and its applications. *Reports Prog. Phys.* **65,** 251 (2002).

55. Di Rienzo, C., Gratton, E., Beltram, F. & Cardarelli, F. Spatiotemporal Fluctuation Analysis: A Powerful Tool for the Future Nanoscopy of Molecular Processes. *Biophys. J.* **111,** 679–685 (2016).

56. Kim, S. A., Heinze, K. G. & Schwille, P. Fluorescence correlation spectroscopy in living cells. *Nat. Methods* **4,** 963 (2007).

57. Digman, M. A., Brown, C. M., Sengupta, P., Wiseman, P. W., Horwitz, A. R. & Gratton, E. Measuring fast dynamics in solutions and cells with a laser scanning microscope. *Biophys. J.* **89,** 1317–1327 (2005).

58. Digman, M. A. & Gratton, E. Analysis of diffusion and binding in cells using the RICS approach. *Microsc. Res. Tech.* **72,** 323–332 (2009).

59. Digman, M. A., Sengupta, P., Wiseman, P. W., Brown, C. M., Horwitz, A. R. & Gratton, E. Fluctuation correlation spectroscopy with a laser-scanning microscope: Exploiting the hidden time structure. *Biophys. J.* **88,** L33–L36 (2005).

60. Di Rienzo, C., Piazza, V., Gratton, E., Beltram, F. & Cardarelli, F. Probing short-range protein Brownian motion in the cytoplasm of living cells. *Nat. Commun.* **5,** 1–8 (2014).

61. Gröner, N., Capoulade, J., Cremer, C. & Wachsmuth, M. Measuring and imaging diffusion with multiple scan speed image correlation spectroscopy. *Opt. Express* **18,** 21225–21237 (2010).

62. Hebert, B., Costantino, S. & Wiseman, P. W. Spatiotemporal image correlation spectroscopy (STICS) theory, verification, and application to protein velocity mapping in living CHO cells. *Biophys. J.* **88,** 3601–3614 (2005).

63. Hebert, B., Costantino, S. & Wiseman, P. W. Spatiotemporal image correlation spectroscopy (STICS) theory, verification, and application to protein velocity mapping in living CHO cells. *Biophys. J.* (2005). doi:10.1529/biophysj.104.054874

64. Digiacomo, L., D'Autilia, F., Durso, W., Tentori, P. M., Caracciolo, G. & Cardarelli, F. Dynamic fingerprinting of sub-cellular nanostructures by image mean square displacement analysis. *Sci. Rep.* (2017). doi:10.1038/s41598-017-13865-4

65. Wang, L., Xiao, Y., Tian, W. & Deng, L. Activatable rotor for quantifying lysosomal viscosity in living cells. *J. Am. Chem. Soc.* (2013). doi:10.1021/ja311688g

66. Digiacomo, L., D'Autilia, F., Durso, W., Tentori, P. M., Caracciolo, G. & Cardarelli, F. Dynamic fingerprinting of sub-cellular nanostructures by image mean square displacement analysis. *Sci. Rep.* **7,** 1–10 (2017).

67. Lanzano, L., Digman, M. A., Fwu, P., Giral, H., Levi, M. & Gratton, E. Nanometer-scale imaging by the modulation tracking method. *J. Biophotonics* (2011). doi:10.1002/jbio.201100002

68. Cardarelli, F., Lanzano, L. & Gratton, E. Capturing directed molecular motion in the nuclear pore complex of live cells. *Proc. Natl. Acad. Sci.* (2012). doi:10.1073/pnas.1200486109

69. Cardarelli, F., Lanzano, L. & Gratton, E. Fluorescence Correlation Spectroscopy of Intact Nuclear Pore Complexes. *Biophys. J.* (2011). doi:10.1016/j.bpj.2011.04.057

70. Lanzano, L., Lei, T., Okamura, K., Giral, H., Caldas, Y., Masihzadeh, O., Gratton, E., Levi, M. & Blaine, J. Differential modulation of the molecular dynamics of the type IIa and IIc sodium phosphate cotransporters by parathyroid hormone. *Am. J. Physiol. - Cell Physiol.* **301,** 850–861 (2011).

71. Appelqvist, H., Wäster, P., Kågedal, K. & Öllinger, K. The lysosome: From waste bag to potential therapeutic target. *Journal of Molecular Cell Biology* (2013). doi:10.1093/jmcb/mjt022

72. Ballabio, A. The awesome lysosome. *EMBO Mol. Med.* (2016). doi:10.15252/emmm.201505966

73. C., S., A., F., D.L., M. & A., B. Signals from the lysosome: A control centre for cellular clearance and energy metabolism. *Nat. Rev. Mol. Cell Biol.* (2013). doi:10.1038/nrm3565

74. Di Malta, C. *et al.* Transcriptional activation of RagD GTPase controls mTORC1 and promotes cancer growth. *Science (80-.).* (2017). doi:10.1126/science.aag2553

75. Levi, V., Ruan, Q. Q. & Gratton, E. 3-D particle tracking in a two-photon microscope: Application to the study of molecular dynamics in cells. *Biophys. J.* (2005). doi:10.1529/biophysj.104.044230

76. Kis-Petikova, K. & Gratton, E. Distance Measurement by Circular Scanning of the Excitation Beam in the Two-Photon Microscope. *Microsc. Res. Tech.* (2004). doi:10.1002/jemt.10417

77. Weber, G. & Farris, F. J. Synthesis and Spectral Properties of a

Hydrophobic Fluorescent Probe: 6-Propionyl-2-(dimethylamino)naphthalene. *Biochemistry* (1979). doi:10.1021/bi00581a025

78. Thoke, H. S., Thorsteinsson, S., Stock, R. P., Bagatolli, L. A. & Olsen, L. F. The dynamics of intracellular water constrains glycolytic oscillations in Saccharomyces cerevisiae. *Sci. Rep.* (2017). doi:10.1038/s41598-017-16442-x

79. Thoke, H. S., Tobiesen, A., Brewer, J., Hansen, P. L., Stock, R. P., Olsen, L. F. & Bagatolli, L. A. Tight coupling of metabolic oscillations and intracellular water dynamics in Saccharomyces cerevisiae. *PLoS One* (2015). doi:10.1371/journal.pone.0117308

80. Parasassi, T., De Stasio, G., Ravagnan, G., Rusch, R. M. & Gratton, E. Quantitation of lipid phases in phospholipid vesicles by the generalized polarization of Laurdan fluorescence. *Biophys. J.* (1991). doi:10.1016/S0006-3495(91)82041-0

81. Parasassi, T., Krasnowska, E. K., Bagatolli, L. & Gratton, E. Laurdan and Prodan as Polarity-Sensitive Fluorescent Membrane Probes. *J. Fluoresc.* (1998). doi:10.1023/A:1020528716621

82. Liu, T., Liu, X., Spring, D. R., Qian, X., Cui, J. & Xu, Z. Quantitatively mapping cellular viscosity with detailed organelle information via a designed PET fluorescent probe. *Sci. Rep.* (2014). doi:10.1038/srep05418

83. Zeng, J. & Chong, P. L. Effect of ethanol-induced lipid interdigitation on the membrane solubility of Prodan, Acdan, and Laurdan. *Biophys. J.* (1995). doi:10.1016/S0006-3495(95)80218-3

84. Begarani, F., D'Autilia, F., Signore, G., Del Grosso, A., Cecchini, M., Gratton, E., Beltram, F. & Cardarelli, F. Capturing Metabolism-Dependent Solvent Dynamics in the Lumen of a Trafficking Lysosome. *ACS Nano* (2019). doi:10.1021/acsnano.8b07682

85. Dross, N., Spriet, C., Zwerger, M., Müller, G., Waldeck, W. & Langowski, J. Mapping eGFP oligomer mobility in living cell nuclei. *PLoS One* (2009). doi:10.1371/journal.pone.0005041

86. Devany, J., Chakraborty, K. & Krishnan, Y. Subcellular Nanorheology Reveals Lysosomal Viscosity as a Reporter for Lysosomal Storage Diseases. *Nano Lett.* **18,** 1351–1359 (2018).

87. Lübke, T., Lobel, P. & Sleat, D. E. Proteomics of the lysosome. *Biochimica et Biophysica Acta - Molecular Cell Research* (2009). doi:10.1016/j.bbamcr.2008.09.018

88. Xu, H. & Ren, D. Lysosomal Physiology. *Annu. Rev. Physiol.* (2015). doi:10.1146/annurev-physiol-021014-071649

89. Lim, C. Y. & Zoncu, R. The lysosome as a command-and-control center for cellular metabolism. *Journal of Cell Biology* (2016). doi:10.1083/jcb.201607005

90. Klymchenko, A. S. Solvatochromic and Fluorogenic Dyes as Environment-Sensitive Probes: Design and Biological Applications. *Acc. Chem. Res.* (2017). doi:10.1021/acs.accounts.6b00517

91. Parasassi, T. & Gratton, E. Membrane lipid domains and dynamics as detected by Laurdan fluorescence. *J. Fluoresc.* (1995). doi:10.1007/BF00718783

92. Celli, A., Beretta, S. & Gratton, E. Phase fluctuations on the micron-submicron scale in GUVs composed of a binary lipid mixture. *Biophys. J.* (2008). doi:10.1529/biophysj.107.105353

93. Celli, A. & Gratton, E. Dynamics of lipid domain formation: Fluctuation analysis. *Biochimica et Biophysica Acta - Biomembranes* (2010). doi:10.1016/j.bbamem.2009.12.002

94. Sanchez, S. A., Tricerri, M. A. & Gratton, E. Laurdan generalized polarization fluctuations measures membrane packing micro-heterogeneity in vivo. *Proc. Natl. Acad. Sci.* (2012). doi:10.1073/pnas.1118288109

95. Steinman, R. M., Mellman, I. S., Muller, W. A. & Cohn, Z. A. Endocytosis and the recycling of plasma membrane. *Journal of Cell Biology* (1983). doi:10.1083/jcb.96.1.1

96. Voccoli, V., Tonazzini, I., Signore, G., Caleo, M. & Cecchini, M. Role of extracellular calcium and mitochondrial oxygen species in psychosine-induced oligodendrocyte cell death. *Cell Death Dis.* (2014). doi:10.1038/cddis.2014.483

97. Del Grosso, A., Antonini, S., Angella, L., Tonazzini, I., Signore, G. &

Cecchini, M. Lithium improves cell viability in psychosine-treated MO3.13 human oligodendrocyte cell line via autophagy activation. *J. Neurosci. Res.* (2016). doi:10.1002/jnr.23910

98. Duchen, L. W., Eicher, E. M., Jacobs, J. M., Scaravilli, F. & Teixeira, F. Hereditary leucodystrophy in the mouse: The new mutant twitcher. *Brain* (1980). doi:10.1093/brain/103.3.695

99. Cappello, V., Marchetti, L., Parlanti, P., Landi, S., Tonazzini, I., Cecchini, M., Piazza, V. & Gemmi, M. Ultrastructural characterization of the lower motor system in a mouse model of krabbe disease. *Sci. Rep.* (2016). doi:10.1038/s41598-016-0001-8

100. Hawkins-Salsbury, J. A., Parameswar, A. R., Jiang, X., Schlesinger, P. H., Bongarzone, E., Ory, D. S., Demchenko, A. V & Sands, M. S. Psychosine, the cytotoxic sphingolipid that accumulates in globoid cell leukodystrophy, alters membrane architecture. *J. Lipid Res.* **54,** 3303–3311 (2013).

101. Spitzer, J. From Water and Ions to Crowded Biomacromolecules: In Vivo Structuring of a Prokaryotic Cell. *Microbiol. Mol. Biol. Rev.* (2011). doi:10.1128/mmbr.00010-11

102. Parry, B. R., Surovtsev, I. V., Cabeen, M. T., O'Hern, C. S., Dufresne, E. R. & Jacobs-Wagner, C. The bacterial cytoplasm has glass-like properties and is fluidized by metabolic activity. *Cell* (2014). doi:10.1016/j.cell.2013.11.028

103. Munder, M. C. *et al.* A pH-driven transition of the cytoplasm from a fluid- to a solid-like state promotes entry into dormancy. *Elife* (2016). doi:10.7554/eLife.09347

104. Rabouille, C. & Alberti, S. Cell adaptation upon stress: the emerging role of membrane-less compartments. *Current Opinion in Cell Biology* (2017). doi:10.1016/j.ceb.2017.02.006

105. Hyman, A. A. & Simons, K. Beyond oil and water - Phase transitions in cells. *Science* (2012). doi:10.1126/science.1223728

106. Weber, S. C. & Brangwynne, C. P. Getting RNA and protein in phase. *Cell* (2012). doi:10.1016/j.cell.2012.05.022

107. Milovanovic, D., Wu, Y., Bian, X. & De Camilli, P. A liquid phase of synapsin and lipid vesicles. *Science (80-.).* (2018).

doi:10.1126/science.aat5671

108. Su, X., Ditlev, J. A., Hui, E., Xing, W., Banjade, S., Okrut, J., King, D. S., Taunton, J., Rosen, M. K. & Vale, R. D. Phase separation of signaling molecules promotes T cell receptor signal transduction. *Science (80-.).* (2016). doi:10.1126/science.aad9964

109. Ling, G. N. & others. physical theory of the living state. (1962).

110. Bianchini, P., Harke, B., Galiani, S., Vicidomini, G. & Diaspro, A. Single-wavelength two-photon excitation-stimulated emission depletion (SW2PE-STED) superresolution imaging. *Proc. Natl. Acad. Sci. U. S. A.* (2012). doi:10.1073/pnas.1119129109

111. Manders, E. M., Stap, J., Brakenhoff, G. J., van Driel, R. & Aten, J. A. Dynamics of three-dimensional replication patterns during the S-phase, analysed by double labelling of DNA and confocal microscopy. *J. Cell Sci.* (1992).

112. Bangham, A. D., Standish, M. M. & Weissmann, G. The action of steroids and streptolysin S on the permeability of phospholipid structures to cations. *J. Mol. Biol.* (1965). doi:10.1016/S0022-2836(65)80094-8

113. Mayer, L. D., Hope, M. J., Cullis, P. R. & Janoff, A. S. Solute distributions and trapping efficiencies observed in freeze-thawed multilamellar vesicles. *BBA - Biomembr.* (1985). doi:10.1016/0005-2736(85)90084-7

114. Lira, R. B., Steinkühler, J., Knorr, R. L., Dimova, R. & Riske, K. A. Posing for a picture: Vesicle immobilization in agarose gel. *Sci. Rep.* (2016). doi:10.1038/srep25254

115. Cardarelli, F., Margheritis, E., Marotta, R., Cassano, D., Begarani, F. & Voliani, V. Silica-Based Nanoparticles for Protein Encapsulation and Delivery. *Nanomaterials* (2018). doi:10.3390/nano8110886

116. Kinch, M. S. An overview of FDA-approved biologics medicines. *Drug Discov. Today* **20,** 393–398 (2015).

117. Carter, P. J. Introduction to current and future protein therapeutics: A protein engineering perspective. *Exp. Cell Res.* **317,** 1261–1269

(2011).

118. Leader, B., Baca, Q. J. & Golan, D. E. Protein therapeutics: A summary and pharmacological classification. *Nat. Rev. Drug Discov.* **7,** 21–39 (2008).

119. Yu, M., Gu, Z., Ottewell, T. & Yu, C. Silica-based nanoparticles for therapeutic protein delivery. *Journal of Materials Chemistry B* (2017). doi:10.1039/c7tb00244k

120. Yu, M., Wu, J., Shi, J. & Farokhzad, O. C. Nanotechnology for protein delivery: Overview and perspectives. *J. Control. Release* (2016). doi:10.1016/j.jconrel.2015.10.012

121. Blanco, E., Shen, H. & Ferrari, M. Principles of nanoparticle design for overcoming biological barriers to drug delivery. *Nat. Biotechnol.* **33,** 941–951 (2015).

122. Frokjaer, S. & Otzen, D. E. Protein drug stability: A formulation challenge. *Nat. Rev. Drug Discov.* **4,** 298–306 (2005).

123. Pisal, D. S., Kosloski, M. P. & Balu-Iyer, S. V. Delivery of therapeutic proteins. *Journal of Pharmaceutical Sciences* (2010). doi:10.1002/jps.22054

124. Levin, D., Golding, B., Strome, S. E. & Sauna, Z. E. Fc fusion as a platform technology: Potential for modulating immunogenicity. *Trends Biotechnol.* **33,** 27–34 (2015).

125. Yu, M. & Zheng, J. Clearance Pathways and Tumor Targeting of Imaging Nanoparticles. *ACS Nano* **9,** 6655–6674 (2015).

126. Parodi, A. *et al.* Synthetic nanoparticles functionalized with biomimetic leukocyte membranes possess cell-like functions. *Nat. Nanotechnol.* **8,** 61–68 (2013).

127. Wang, C., Sun, X., Cheng, L., Yin, S., Yang, G., Li, Y. & Liu, Z. Multifunctional theranostic red blood cells for magnetic-field-enhanced in vivo combination therapy of cancer. *Adv. Mater.* **26,** 4794–4802 (2014).

128. Yan, M. *et al.* A novel intracellular protein delivery platform based on single-protein nanocapsules. *Nat. Nanotechnol.* **5,** 48–53 (2010).

129. Li, S. & Huang, L. reviews Pharmacokinetics and Biodistribution of

Nanoparticles. *Mol. Pharm.* (2008). doi:10.1021/mp800049w

130. Cassano, D., David, J., Luin, S. & Voliani, V. Passion fruit-like nano-architectures: a general synthesis route. *Sci. Rep.* **7,** 43795 (2017).

131. Wu, J. *et al.* Development of multinuclear polymeric nanoparticles as robust protein nanocarriers. *Angew. Chemie - Int. Ed.* (2014). doi:10.1002/anie.201404766

132. Galliani, M., Santi, M., Del Grosso, A., Cecchettini, A., Santorelli, F. M., Hofmann, S. L., Lu, J. Y., Angella, L., Cecchini, M. & Signore, G. Cross-Linked Enzyme Aggregates as Versatile Tool for Enzyme Delivery: Application to Polymeric Nanoparticles. *Bioconjug. Chem.* **29,** 2225–2231 (2018).

133. Estey, T., Kang, J., Schwendeman, S. P. & Carpenter, J. F. BSA degradation under acidic conditions: A model for protein instability during release from PLGA delivery systems. *J. Pharm. Sci.* (2006). doi:10.1002/jps.20625

134. Guerrero-Martínez, A., Pérez-Juste, J. & Liz-Marzán, L. M. Recent progress on silica coating of nanoparticles and related nanomaterials. *Adv. Mater.* **22,** 1182–1195 (2010).

135. Cassano, D., Pocoví-Martínez, S. & Voliani, V. Ultrasmall-in-Nano Approach: Enabling the Translation of Metal Nanomaterials to Clinics. *Bioconjug. Chem.* **29,** 4–16 (2018).

136. Zhang, Y., Hsu, B. Y. W., Ren, C., Li, X. & Wang, J. Silica-based nanocapsules: Synthesis, structure control and biomedical applications. *Chem. Soc. Rev.* **44,** 315–335 (2015).

137. Ferrari, M. Cancer nanotechnology: Opportunities and challenges. *Nat. Rev. Cancer* **5,** 161–171 (2005).

138. Xu, R. *et al.* An injectable nanoparticle generator enhances delivery of cancer therapeutics. *Nat. Biotechnol.* **34,** 414–418 (2016).

139. Cassano, D., Santi, M., Cappello, V., Luin, S., Signore, G. & Voliani, V. Biodegradable Passion Fruit-Like Nano-Architectures as Carriers for Cisplatin Prodrug. *Part. Part. Syst. Charact.* **33,** 818–824 (2016).

140. Armanetti, P., Pocoví-Martínez, S., Flori, A., Avigo, C., Cassano, D.,

Menichetti, L. & Voliani, V. Dual photoacoustic/ultrasound multi-parametric imaging from passion fruit-like nano-architectures. *Nanomedicine Nanotechnology, Biol. Med.* **14,** 1787–1795 (2018).

141. Croissant, J. G., Fatieiev, Y. & Khashab, N. M. Degradability and Clearance of Silicon, Organosilica, Silsesquioxane, Silica Mixed Oxide, and Mesoporous Silica Nanoparticles. *Adv. Mater.* **29,** (2017).

142. Mapanao, A.-K., Santi, M., Faraci, P., Cappello, V., Cassano, D. & Voliani, V. Endogenously-Triggerable Ultrasmall-in-Nano Architectures: Targeting Assessment on 3D Pancreatic Carcinoma Spheroids. *ACS Omega* (2018).

143. d'Amora, M., Cassano, D., Pocoví-Martínez, S., Giordani, S. & Voliani, V. Biodistribution and biocompatibility of passion fruit-like nano-architectures in zebrafish. *Nanotoxicology* 1–9 (2018). doi:10.1080/17435390.2018.1498551

144. Bégu, S., Pouëssel, A. A., Lerner, D. A., Tourné-Péteilh, C. & Devoisselle, J. M. Liposil, a promising composite material for drug storage and release. *J. Control. Release* **118,** 1–6 (2007).

145. Gokhale, P. C., Radhakrishnan, B., Husain, S. R., Abernethy, D. R., Sacher, R., Dritschilo, A. & Rahman, A. An improved method of encapsulation of doxorubicin in liposomes: Pharmacological, toxicological and therapeutic evaluation. *Br. J. Cancer* **74,** 43–48 (1996).

146. Masalov, V. M., Sukhinina, N. S., Kudrenko, E. A. & Emelchenko, G. A. Mechanism of formation and nanostructure of Stöber silica particles. *Nanotechnology* (2011). doi:10.1088/0957-4484/22/27/275718

147. Lee, W. C., Kang, D., Causevic, E., Herdt, A. R., Eckman, E. A. & Eckman, C. B. Molecular Characterization of Mutations That Cause Globoid Cell Leukodystrophy and Pharmacological Rescue Using Small Molecule Chemical Chaperones. *J. Neurosci.* **30,** 5489–5497 (2010).

148. Manzo, C. & Garcia-Parajo, M. F. A review of progress in single particle tracking: from methods to biophysical insights. *Reports Prog. Phys.* **78,** 124601 (2015).

149. Göttfert, F., Wurm, C. A., Mueller, V., Berning, S., Cordes, V. C.,

Honigmann, A. & Hell, S. W. Coaligned dual-channel STED nanoscopy and molecular diffusion analysis at 20 nm resolution. *Biophys. J.* **105,** L01--L03 (2013).

150. Majer, G. & Melchior, J. P. Characterization of the fluorescence correlation spectroscopy (FCS) standard Rhodamine 6G and calibration of its diffusion coefficient in aqueous solutions. *J. Chem. Phys.* **140,** (2014).

List of Figures

List of Tables

Acknowledgements

I would like to express my gratitude to many people for their support and assistance during my PhD experience.

First of all, I would like to thank Prof. Francesco Cardarelli for closely helping me in organizing my entire PhD project. The countless fruitful discussions we had, still represent the very turning point of my professional life. I would also like to acknowledge Prof. Fabio Beltram, for giving me the opportunity to work at NEST research center, Prof. Stefano Luin, Dr. Giovanni Signore and Dr. Francesca D'Autilia for their precious contribution to my project.

A special "Thanks" goes to all the people I had the pleasure to meet at NEST laboratory and at Scuola Normale Superiore, and who helped me in many ways: among these, Domenica Convertino, Domenico Cassano, Ambra Del Grosso, Tommaso Cavallucci, Paolo Tentori, Luca Bellucci, Piero Mazzarisi, Cecilia Masciullo, Antonio Rossi, Eleonora Margheritis, Federica Bianco, Melissa Santi, Gina Greco, Francesco Colangelo, Rosy Amodeo, Marianna Galliani, Paola Parlanti, Gianmarco Ferri and Carmine di Rienzo.

Dutiful thanks are addressed to all my friends who represented an unmatchable source of distraction and relax.

However, the highest acknowledgment must go to my family who supported me in every moment of my life and gave me the chance to study and do research!

Last but not least a huge thanks to Alissa Mazzei for her priceless support!!